Pulsed Laser Deposition of Heteroepitaxial Ferroelectric Thin Film Capacitor

Yip Ping Wah

M.Phil.

The Hong Kong Polytechnic University

2001

Pulsed Laser Deposition of Heteroepitaxial Ferroelectric Thin Film Capacitor

Submitted by

Yip Ping Wah

For The Degree of

Master of Philosophy in Applied Physics

at

The Hong Kong Polytechnic University

in August 2000

TABLE OF CONTENTS

Acknowledgements

I would like to acknowledge my supervisor, Dr. K. H. Wong for his valuable advice and fruitful discussions throughout these two years. Special thanks should be given to Dr. W. B. Wu and Dr. K. W. Kwok for their enlightening suggestions and assistance in this project.

I would also like to thank all my research companions especially Mr. K. S. So for lending help in some technical problems.

This work was supported by a Research Grant of The Hong Kong Polytechnic University under the Code No.G-V724. I am grateful for the award of a research studentship by The Hong Kong Polytechnic University.

Abstract

In the present studies, high quality conducting $SrVO_3$ (SVO) and $YBa_2Cu_3O_{7-x}$ (YBCO) oxide thin films were grown by Pulsed Laser Deposition (PLD) method. It has been demonstrated that SVO films can be epitaxially grown on Si at a processing temperature as low as 550°C and heteroepitaxial relationship of $(100)_{SVO}||(100)_{TiN}||(100)_{Si}$ has been obtained. Our SVO films are of good metallic properties and a very low resistivity of 3 $\mu\Omega$-cm at 78 K has been recorded. The high temperature superconducting YBCO films integrating on Si through the STO/TiN buffer layers also show good metallic property and have good electrical conduction of 95 $\mu\Omega$-cm at room temperature. Its transition temperature (T_c) is about 88 K. However, from the scanning electron microscopic studies of the YBCO/STO/TiN/Si heterostructure, microcracks were observed. The microcracks may arise from the large difference in thermal expansion mismatch between YBCO and STO and the oxidation of TiN layer. In view of this, magnesium oxide (MgO), a buffer material with better thermal matching with YBCO and a good oxygen diffusion barrier for protecting TiN from oxidation during the growth of YBCO was used. From the scanning electron microscopic studies of the YBCO/MgO/TiN/Si heterostructure, a crack-free and a much better surface morphologies has been observed. In addition, it did allow a better crystal growth of PZT films on YBCO bottom electrode, i.e. PZT/YBCO/MgO/TiN/Si. Both the structure and electrical properties of the Au/PZT/YBCO/MgO/TiN/Si integrated ferroelectric capacitors are comparable to those grown on single crystal $LaAlO_3$ (LAO) substrates. The Au/PZT/YBCO/MgO/TiN/Si integrated ferroelectric capacitor shows good

ferroelectric properties such as high remnant polarization, low coercive field and high dielectric constant with low dielectric loss values. No polarization fatigue was observed at bi-polar switching up to 10^7 cycles. The leakage current of such capacitor is in the order of 10^{-7} A/cm^2.

In short, SVO films of good crystal quality has been fabricated on Si substrates through TiN buffered layer and the processing temperature can be as low as 550°C. Besides, a very low resistivity of SVO films has been obtained. In addition, the merits of using MgO/TiN buffer layers over that of STO/TiN has been demonstrated. Up till now, there are many choices of buffer layers for growing perovskites films. It is our believe that the discovery of the advantage of using MgO/TiN buffer layers will have a great influence on people's decision when they choose the materials for buffer layers. Finally, as an example, excellent quality of the heteroepitaxial Au/PZT/YBCO/MgO/TiN/Si integrated ferroelectric capacitors for potential non-volatile memory devices were fabricated.

Chapter 1

Introduction

1.1 Introduction

Nonvolatile, fast switching and radiation hardness are some of the attributes of ferroelectric memory devices that make them more desirable than their semiconductor counterparts. Ferroelectric thin film capacitors thus offer a colossal potential for future applications in microelectronic industry. Yet, issues pertaining to integration and long term properties, such as polarization switching fatigue in some ferroelectrics like $Pb(Zr_{0.52}Ti_{0.48})O_3$ (PZT), have to be addressed and overcome.

In the past few years, conductive oxides have been used as electrodes for all ferroelectric thin film capacitors [Wu et al., 2000]. Superior and near fatigue free operations have been demonstrated. For example, oxide electrodes, RuO_2 [Vijay et al., 1993], IrO_2 [Vijay et al., 1993], $La_{0.5}Sr_{0.5}CoO_3$(LSCO) [Ramesh et al., 1993] and $YBa_2Cu_3O_7$(YBCO) [Kurogi et al., 1998] which have good electrical conductivity have been shown to improve the fatigue performance of PZT thin films significantly. With conducting oxide electrodes, it is thought that the trapped oxygen vacancies could be compensated by the oxygen from within the electrodes. Eventually, it can then alleviate the internal field and thus prevent fatigue. However, the choice of appropriate oxide electrodes that have sufficiently low resistivity and lattice-match with the ferroelectric is wide open and is at present under intense investigation. An

all epitaxially growth trilayered capacitor structures with sharp and clean interface will undoubtedly have superior electrical characteristics. Very low leakage current and long term switching stability are expected.

For miniaturized device application, successful integration of the ferroelectric thin films into IC is essential. This implies that the perovskite oxides need to be epitaxially grown on Si. For this reason a buffer layer of compatible structural, electrical as well as thermal properties are required. TiN has been known to grow epitaxially on Si [Narayan et al., 1992]. More recently, STO/TiN heteroepitaxially grown on Si has been demonstrated [Lee et al., 1997]. Thus the STO/TiN/Si will form an excellent platform for epitaxial growth of ferroelectric capacitor [Wu et al., 2000].

Pulsed laser deposition (PLD) has proved to be a very successful technique for fabrication of high quality thin perovskite oxide films. In addition, the PLD is exceedingly favorable in preparing heteroepitaxial multilayers by simply ablating different targets in alternate fashion. We used PLD method to fabricate our proposed heterostructures as well as other related films.

Although there are many reports on fabrication of ferroelectric thin film capacitor, there are, up-to-date, very few reports on preparation and characterization of all epitaxially grown integrated ferroelectric capacitor with conductive oxide electrodes. And only few of them have reported successful epitaxial growth of these structures on Si [Wu et al., 2000]. Our proposed new heteroepitaxial structures are

expected to show better performance for application in nonvolatile FERAMs in microelectronics. Apart from their possible applications, these material systems have good potential to yield vital information and better understanding of the materials science and physics involved.

1.2 Nonvolatile Ferroelectric Random Access Memory (NVFERAM)

Nonvolatile memory is an essential requirement for all computer systems. It is especially important for systems where vital information has to be stored and retained - memory that does not forget when the power is lost. Fig.1.1 shows the schematic diagram of two kinds of NVFERAM architectures which are examples of one transistor and one capacitor (1T-1C) design. This configuration helps to prevent crosstalk between adjacent cells. The high-density architecture (Fig.1.1a) is designed for use as computer memory while the low density architecture (Fig.1.1b) is for smart cards and other applications of embedded memories, say, microprocessor controllers [Auciello et al., 1998].

The selection requirements for a nonvolatile memory include fast read/write, radiation hardness, cost effectiveness via compatibility with currently used integrated circuit (IC) processing technology, high endurance and retention, and nondestructive readout (NDRO) capability [Sinharoy et al., 1992]. In all these respects, ferroelectric memory stands out as the suitable choice.

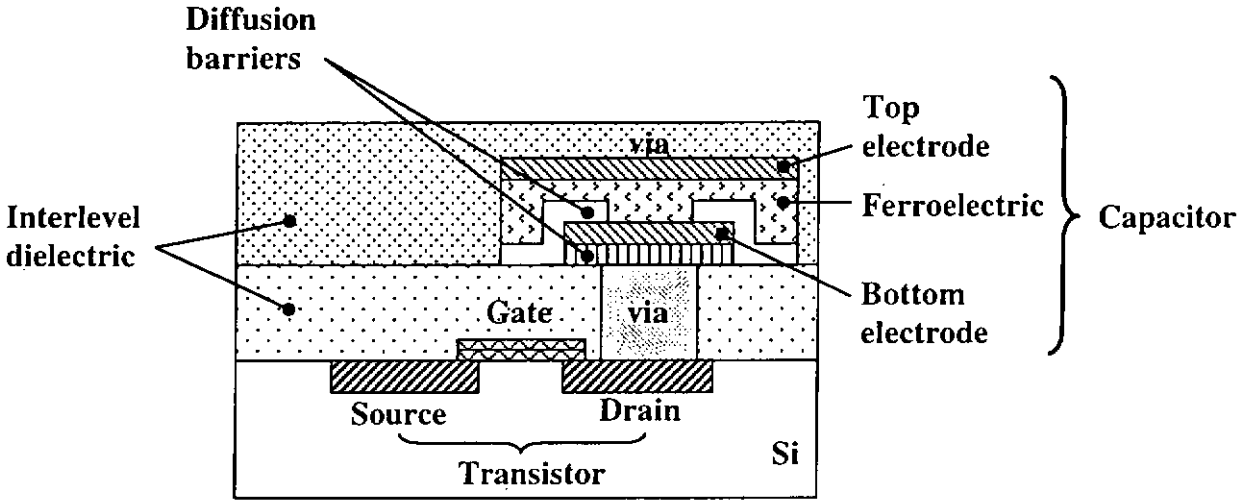

(a)

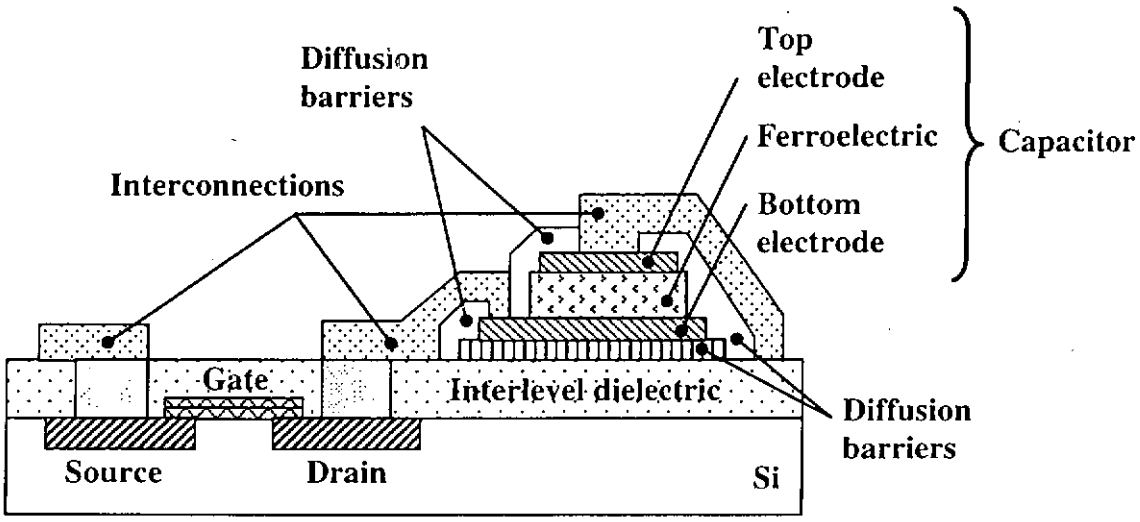

(b)

Fig. 1.1 Schematic diagrams of two kinds of NVFERAM architectures with (a) vertical High-density NVFERAM Architecture (b) lateral Low-density NVFERAM Architecture [Auciello et al., 1998].

Fig.1.2a shows the schematic diagram of the perovskite $A^{2+}B^{4+}O_3^{2-}$ crystal structure with A occupying at the corners, B occupying the centres of each unit cell and O^{2-} ions are centered on each face of the lattice. Above curie temperature, the perovskite crystal structure is cubic lattice whereas below curie temperature, the perovskite crystal structure is tetragonal lattice. Ferroelectric crystals are characterized by having polarization vectors that can be oriented in two diametrically opposite directions (denoted by convention as 1 (Fig.1.2b) and 0 (Fig.1.2c) by applying an external electric field. The 1 and 0 polarization states in a ferroelectric crystal are due to displacements of positive metallic and negative oxygen ions in opposite directions which result in the polarization that characterizes ferroelectric materials. Indeed, the reason why ferroelectric material can be used as nonvolatile memory is because ferroelectric material retains two stable remnant polarization ($\pm$Pr) values at zero field as shown in Fig.1.3. And the polarization reversal from up (1) to down (0) or vice versa as a function of applied voltage can allow the control and sensing of the state of the polarization. If we apply a large electric field to a distorted ferroelectric phase, all the domains can be lined up in the same direction. On the other hand, when we apply a reversed field to the specimen, the polarization of it can be switched from up (1) to down (0). For a large single crystal this change of polarization would require voltages of several kilovolts which is actually impractical for commercial devices [Scott et al., 1989]. Nonetheless, for a thin film of order 100nm thick, this can be achieved only by a few volts. The major concern in the use of ferroelectric in thin film memories is the fatigue problem which is the loss of switchable polarization with electric field cycling.

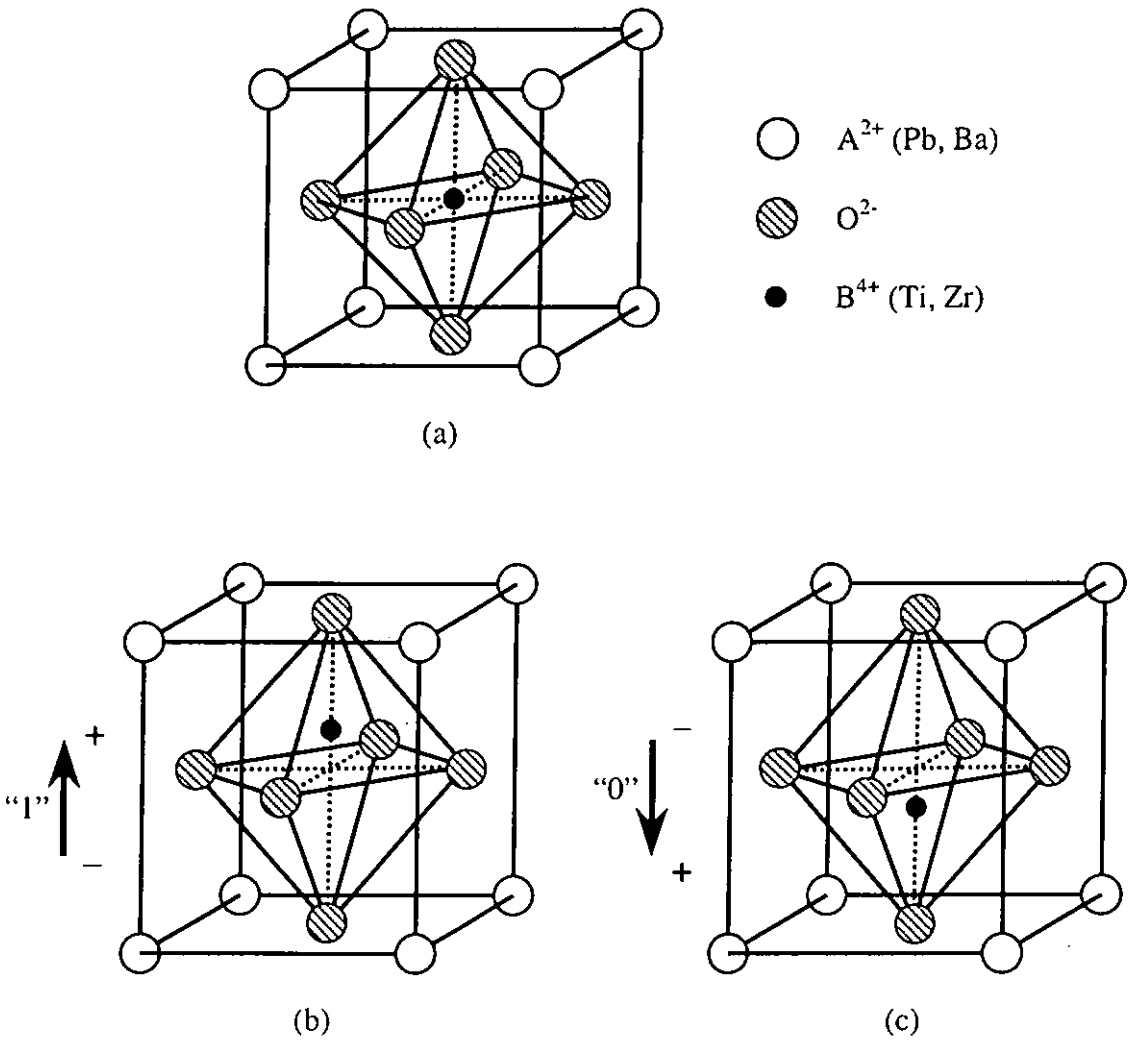

Fig.1.2 Schematic diagrams of the (a) $A^{2+}B^{4+}O_3^{2-}$ perovskite crystal structure: cubic lattice (above Curie temperature); (b) tetragonal lattice (below Curie temperature) with spontaneous polarization pointing upwards; (c) tetragonal lattice (below Curie temperature) with spontaneous polarization pointing downwards.

In fact, the fatigue mechanism has not been well explained yet. In accordance with what other authors have been suggested, the fatigue mechanism may be due to the trapping of oxygen vacancies at the electrode/ferroelectric interface which would then cause an internal field to build up. Consequently, this prevents further domain switching. It is generally believed that the oxygen vacancies in PZT thin film are due to the lead losses during the crystallization of the films [Du et al., 1998].

In Chapter 2, a brief history and the principle of PLD are presented. Besides, the advantages as well as disadvantages of using PLD for film preparation are discussed.

In Chapter 3, the experiments and set-up are presented. Working principles for the four-circle mode X-ray diffraction, four-point probe technique, P-E loop measurement and fatigue test are described.

In Chapter 4, the results of SVO films grown on (100)LAO and (100)Si substrates are reported. The processing parameters as well as the structural and electrical properties of SVO films are discussed. Besides, its scanning electron micrographs of the cross-section and surface morphologies of the SVO films are also shown.

In Chapter 5, the work on fabrication of integrated epitaxial YBCO thin films on Si by PLD method using STO and TiN as buffer layers are presented.

Heteroepitaxial structures of TiN/Si, STO/TiN/Si and YBCO/STO/TiN/Si are prepared and their structural and electrical properties are discussed.

In Chapter 6, the structural and electrical properties of the YBCO/MgO/TiN/Si heterostructure are presented. Its merit over the YBCO/STO/TiN/Si heterostructure is also discussed.

In Chapter 7, the structural characterization and ferroelectric properties of the epitaxial ferroelectric thin-film capacitors based on the Au/$Pb(Zr_{0.52}Ti_{0.48})O_3$/$YBa_2Cu_3O_{7-x}$/MgO/TiN/Si heterostructure are presented. Besides, the superior surface morphologies of PZT thin films when grown on YBCO/MgO/TiN/Si heterostructure instead of YBCO/STO/TiN/Si heterostructure are also discussed.

Finally, a conclusion, in which the results and emphasis of the original achievements of the present work as well as the suggestions for future studies are included, is given in Chapter 8.

Chapter 2

Pulsed Laser Deposition (PLD)

2.1 History of Pulsed Laser Deposition

The first experiment using pulsed laser deposition could be traced back as far as 1965. However, further investigations were sporadic and slow-paced during the next two decades. Nonetheless, the successful growth of high T_c superconducting films in 1987 has allowed the rapid development of PLD [Singh et al., 1998; Douglas et al., 1994].

The present name, pulsed laser deposition (PLD), was named by official voting from the participants of the first Material Research Society Symposium on Pulsed Laser Ablation held in San Francisco in April 1989. Actually, before using the present name, several other names were used such as laser sputtering, laser-assisted deposition and annealing (LADA) pulsed laser evaporation (PLE) laser molecular beam epitaxy (LMBE) laser-induced flash evaporation (LIFE).

2.2 Advantages of Pulsed Laser Deposition

There are various methods which can produce thin films such as co-evaporation [Ishiwara et al., 1991], electron-beam evaporation method [Moon et al., 1994], r.f. sputtering [Lee et al., 1999], chemical vapor deposition (CVD) [Funakubo et al., 1998], molecular beam epitaxy (MBE) [Nagata et al., 1992]. However, PLD offers a number of advantages over the others. The foremost advantage is that it allows

"congruent" evaporation. That means the stoichiometry of multicomponent materials can be preserved in the deposited films and actually it is a great advantage for the deposition of multicomponent ceramics where conventional thermal evaporation or sputtering can lead to non-stoichiometry films. Since the focused laser beam has a very high energy density, it can then ablate all the constituent components of the target simultaneously irrespective of their difference in melting point. Besides, the ablated species are highly energetic. Their kinetic and excitation energies may help them to migrate to their favorable site after deposition. This implies that crystalline films can be grown at a relatively lower substrate temperature. In addition, PLD is probably the simplest among all thin film growth techniques. It can be used to grow thin films of any kind of materials. It also allows the in-situ growth of multilayers of different materials. Actually, it is most suitable for rapid exploration of new materials-integration strategies to develop heterostructures such as all-perovskite capacitor for NVFERAMs. A multiple targets system can be loaded inside the deposition chamber on a rotating holder which can be used to sequentially expose different targets to the laser beam, thereby enabling the in situ growth of heterostructures. Furthermore, film growth can be carried out in a reactive environment containing any kind of gas with or without plasma excitation. For growing oxide films, ambient oxygen, say, can be provided at the time of ablating.

In fact, there are disadvantages in using PLD method to deposit thin films. One of the disadvantages of PLD is its difficulty in coating thick film. Besides, the narrow forward angular distribution that makes large-area smooth film growth a

very difficult task. The film thickness is highest at the center of the plasma plume normal to the target surface and decreases rapidly with the distance away from this point [Venkatesan, 1988]. There are however, some methods to improve the thin films' uniformity. For example, by tilting and rotating the target result in a much larger scanning area of the plasma plume to the substrates and hence can much improve the uniformity of the thin films to form larger area size samples [Greer, 1989; Buhay et al.,1992]. The other intrinsic disadvantage of the PLD method is the formation of micron-sized particulates. This problem is more severe in the multi-layer systems because the particulates on the surface of the films will greatly affect the growth of the subsequent layers and the interface quality. Nonetheless, various approaches such as "crossed fluxes" techniques, and "eclipse" method, were adopted to either reduce or to eliminate those particulates. The insertion of an opaque mask between the target and the substrate forming a shadow mask to block the large particulates emitted from the target in the forward direction has been suggested by Iwabuchi et al. [1994]. Particulate free thin films with very smooth surface have been obtained.

2.3 Principle of Pulsed Laser Deposition

2.3.1 Three Stages for the PLD Process

1) Laser radiation interaction with the target and production of a highly forward directed plume which consists of a mixture of energetic species including atoms, molecules, electrons, ions, clusters, micron-sized solid particulates, and molten globules.

2) The interaction of the plume with a background ambient gas which depends on the type of thin films to be deposited. Oxygen gas is usually added for the oxides films.

3) Condensation, nucleation and growth of a thin film on the substrate surface.

2.3.2 Three Common Modes of Film Growth in the Initial Stages

According to Lewis and Anderson, there are three common modes of film growth in the initial stages. They are Frank-Van Der Merwe, Volmer-Weber and Stranski-Krastanov. The Frank-Van Der Merwe is the growth of one monolayer at a time. Consequently, it has a very smooth epitaxial film. It occurs when the cohesive energy between the film and substrate atoms is greater than the cohesive energy of the film. However, the smoothness of the film monotonically decreases as each new film layer is added. Volmer-Weber is the island growth mode provided that the cohesive energy of the film atoms is greater than the cohesive binding between the film and the substrate atoms. This results in an epitaxial film that has a rough surface, or a polycrystalline film containing voids. Stranski-Krastanov mode which will occur when the monotonic decrease in binding energy with each successive layer is energetically overridden by some factor such as strain energy due to lattice mismatch and island formation becomes more favorable, consists of island growth after the first monolayer has formed successfully.

Among the three modes of growth, Frank-Van Der Merwe is more desirable for thin film growth as it gives a high quality films and epitaxial single crystal films.

However, the three modes of film growth are only important for ultra-thin films and are not a matter of concern for films of thickness $\geq$ 100nm. In the present study, the thickness of the different multilayers fabricated is greater than this value, so, the type of modes of film growth is not the subject of our investigation.

Chapter 3

Experiments and Set-up

3.1 Introduction

All the epitaxially grown films in the present studies were prepared by the PLD technique. The PLD system as shown schematically in Fig.3.1 consisted of a KrF excimer laser, a high vacuum chamber and a rotating multi-target holder. The targets were fabricated by the standard solid state reaction of mixtures of different oxides. The PLD process was carried out under ambient oxygen and at elevated substrate temperatures. The as-prepared films were structurally characterized by X-ray diffractometer. Surface morphology of the films was examined by the scanning electron microscopy (SEM) and the atomic force microscopy (AFM). The correlation between the structural properties and the deposition conditions was studied. The electrical properties of the SVO and YBCO films were measured by the standard four-point-probe technique. Measurement of ferroelectric properties of the capacitors such as P-E loops, switching fatigue, dielectric constant and current-voltage characteristics were carried out.

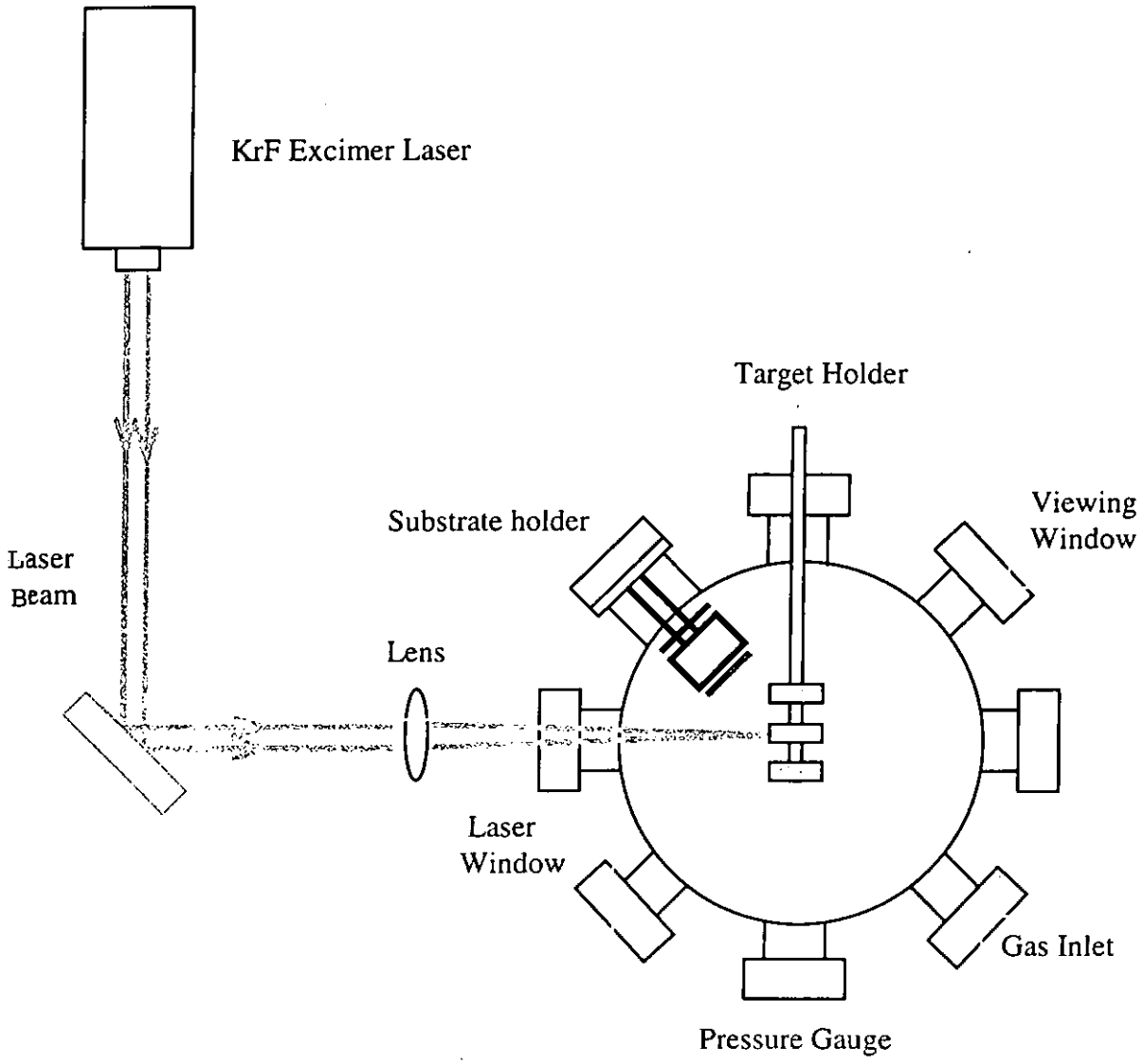

Fig.3.1 The schematic diagram of the pulsed laser deposition system.

3.2 Instruments

3.2.1 Excimer Laser

An excimer laser is a type of gas discharge pulsed laser which can emit high flux of UV photons. In the deposition of our films, a KrF excimer laser was used. The KrF laser involves gases of F_2, Kr and Ne in partial pressure of 4 mbar, 130 mbar and 3210 mbar, respectively. The ionic and electronically excited species are created by the avalanche electric discharge excitation (about 40 kV). At the same time, laser transition takes place during the dissociation of the excimer molecules as the ground state is repulsive and they rapidly dissociate. The resulting radiation wavelength is 248 nm. Our KrF excimer laser is a Lamda Physik COMPex 200. The maximum laser energy is about 500 mJ per pulse and the repetition rate can go up to 20 Hz. The output laser has a near "top-hat" spatial profile with a cross-section measuring 1x3 cm^2 at the exit window. Shot-to-shot laser energy fluctuation is less than 5%. In general, there is no noticeable energy drop over 15-30 minutes duration, which is the typical time span for film deposition.

3.2.2 Optical Elements

The optical elements in the PLD system include lens, mirror and laser window. They are used to couple the energy from the laser to the target and are placed between the output port of the laser and the laser port of the deposition chamber. As dirt tends to attenuate and scatter the light beam, it causes optical damage to the optical components easily, so, all the optical elements used in our PLD experiments have always been kept clean and dust-free.

3.2.2.1 Lens

The lens is used to collect radiation from the laser and to focus it on the target to achieve the required energy density for ablation. Lenses made of various materials such as magnesium fluoride, sapphire, calcium fluoride, UV-grade fused silica, borosilicate crown glass, zinc sulphide and zinc selenide provide different transmittances at different wavelengths. As a KrF excimer laser with wavelength of 248 nm was used in our PLD system, UV-grade fused-silica lens with 99 % transmittance at 248 nm (excluding norminal reflection at the interface) was used. The focal length of the lens was 50 cm.

3.2.2.2 Mirror

The mirrors used in our PLD system are 5 cm diameter and dielectric multilayer coated mirrors which are designed for 45° incidence. The manufacturer quoted reflectivity for the laser beam incident on the coating side is higher than 95%.

3.2.2.3 Laser Window

The function of the laser window is to allow laser to enter the deposition chamber while keeping the chamber at high vacuum. It is a circular flat made of UV-grade fused silica with 5 mm thick and 500 mm diameter. During the PLD process, the window's surface is very often contaminated or coated with the laser ablated materials. For this reason, the window needs to be routinely cleaned and re-polished.

3.2.3 Vacuum Chamber

After the laser beam passed through the optics, it enters the vacuum chamber through the fused silica window. The vacuum chamber had several ports and they are used for heater, pressure gauge, gas inlet, target holder, laser window and viewing window. The heater is made of stainless steel and it is heat-shielded by a few thin plates of stainless steel wrapped around the side of the heater. Kanthal wire (25% chromium, 5% aluminum, 3% cobalt and 67% iron) is used as the filament inside the heater for heating purpose. The diameter of the Kanthal wire is 0.559 mm and the resistance per unit length is 5.1 Ωm^{-1}. A total resistance of the Kanthal wire

used was 15 Ω. A K-type (Nickel-Chromium, Nickel-Aluminum) thermocouple is inserted into the heating block for the measurement of the substrate temperature. The temperature is controlled by a temperature controller (PAC25-0321) capable of operating a temperature range room temperature to 750°C. The substrates are pasted onto the top of the heating-block with silver paint (G3691 Agar Scientific Ltd.) as it has good heat conduction and can provide good adhesion between the heating block and the substrates.

The base pressure of the vacuum chamber is monitored by an ionization gauge (Type WI-T). The ambient gas pressure during deposition and post-annealing is measured by a Baratron pressure gauge (MKS Baratron Type 122A) which is mounted on one of the chamber port. A digital meter (MKS Type PDR-D-1 Power Supply Digital Readout) is connected to the pressure gauge to display the value. The range of the measurable pressure is 1 mTorr to 12 Torr with the accuracy of ±0.01% of full scale.

3.2.4 X-ray Diffractometer (XRD)

The crystal structures of the thin films are characterized by an X-ray diffractometer (Philip X'pert system) in four-circle mode. The Cu K_α radiation (λ=1.54Å) is used and the K_β line is filtered by a Ni filter. Fig.3.2 shows a schematic digram of the X-ray diffraction of a crystal. When X-ray falls on atoms in a crystal, each atom scatters a small fraction of the incident beam. The reflected beams from all atoms in the crystal planes involved may interfere and the resultant

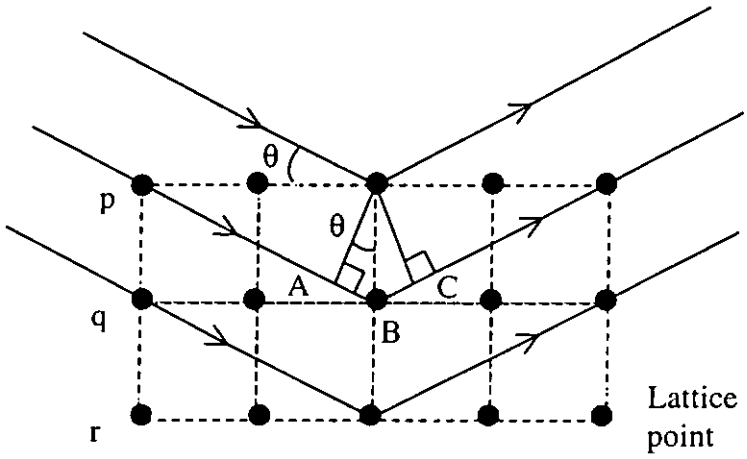

Fig.3.2 The schematic diagram of X-ray diffraction of a crystal

reflected beam is strong only when the path difference between the successive planes is an integral number of the wavelength of the incident X-ray. That means reinforcement only occurs for planes p and q when AB + BC = $n\lambda$, where n is an integer and λ is the wavelength of the X-ray. If d is the distance between planes of atoms and θ is the angle between the X-ray beam and the crystal plane, then AB + BC = $2d \sin\theta$, and the reflected beam has maximum intensity when

$$2d \sin\theta = n\lambda \qquad \text{(Bragg's Law)} \qquad (3.1)$$

and the d value is calculated as

$$d = a/(h^2+k^2+l^2)^{1/2} \qquad (3.2)$$

where a is the lattice constant of the crystal structure and h, k and l are the reciprocal lattice indices for a-axis, b-axis and c-axis respectively.

For example, to calculate the 2θ angle for (400)Si:

As a = 5.43Å for (100) Si, λ = 1.54Å for K_α radiation of Cu in X-ray

Then $d = 5.43/ (4^2+0+0)^{1/2}$Å = 1.3575 Å

From Equation (3.1),

$2\theta = 69.11°$.

3.3 Experimental Procedures

3.3.1 Substrate Preparation

The (100)Si wafer and (100)LAO were used as substrates. For convenient analysis and measurement, they were cut into small pieces with dimension of 0.5x1

cm^2. Since contamination on the substrates will interfere with the registration of the atoms of the deposited layer, a basic requirement for epitaxy is an atomically clean surface prior to deposition. Hence, the (100)Si substrates were cleaned prior to insertion in the vacuum chamber by ultrasonically degreasing in acetone for 6 - 10 minutes and by immersing in 10 % HF solution for 10 minutes to remove the surface oxide layers. The substrates were then cleaned with deionized water and acetone. For the (100)LAO substrates, similar cleaning procedure, but without HF etching was performed.

3.3.2 Deposition Process

All the thin films, including TiN, $SrVO_3$ (SVO), $SrTiO_3$ (STO), MgO, $YBa_2Cu_3O_{7-x}$ (YBCO) and $Pb(Zr_{0.52}Ti_{0.48})O_3$ (PZT) were deposited by the PLD method. For the in-situ deposition of multilayer thin films, all the targets (TiN, SVO, STO, MgO, YBCO and PZT) were mounted on the same rotating target holder (Fig.3.3). By adjusting the vertical position of the rod, the laser beam was focused onto the round surfaces of different targets for ablation. To avoid digging a hole on the target, the target was rotated during ablation.

The substrate was pasted to the heater by silver paint which acted as a heat conducting medium. The temperature of the substrate heater was set in the range of 450°C - 750°C and was controlled by a temperature controller. The distance between the target and the substrate was 4 cm. When high-vacuum deposition was required, the chamber was evacuated by a rotary pump first until the pressure was

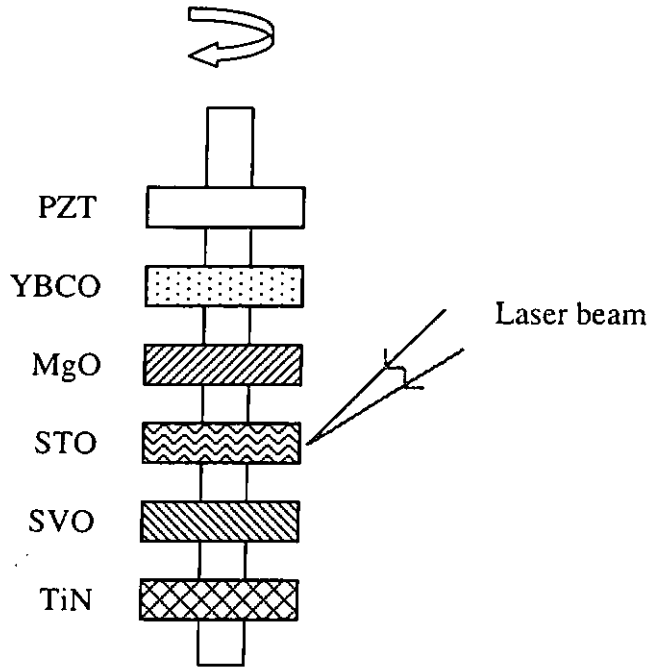

Fig.3.3 The schematic diagram of the multi-target holder for in-situ deposition of multilayer thin films

approximately 10 mTorr. Then a cryo-pump was used to obtain a base pressure of $\leq 10^{-6}$ Torr. Indeed, the type of pump used and the vacuum required depended on the kinds of films to be deposited. For TiN, SVO, STO and MgO films, all of them needed to be prepared at high vacuum. After the cryo-pump had evacuated for a certain amount of time, e.g. 10 minutes, the substrate was heated to the desired temperature. After the substrate was stablized at the desired temperature, the laser was switched on and pulsed at a repetition rate of 10 Hz for a certain amount of time. The thickness of the thin film was controlled by the deposition time.

In order to obtain high crystallinity and to reduce oxygen deficiency, the films were post annealed at elevated temperature for about 10 – 30 minutes under high vacuum or in an ambient gas pressure.

3.3.3 Structural Analysis of Thin Films

The structure of the thin films was characterized by X-ray diffractometer (XRD). In order to determine the epitaxial quality of the deposited thin films, θ-2θ scan, ω-scan (rocking curve) and 360° ϕ-scan were carried out. Fig.3.4 shows the three axes rotation of the sample, i.e. θ axis, φ axis and ϕ axis.

For the θ-2θ scan, it allows us to observe the lattice planes of the thin films grown with the direction parallel to the normal direction of the substrate surface. If epitaxial thin films are grown, only one set of planes of a family (e.g. (h00)) should be observed and it needs to be the same as the substrate (i.e. (h00)). Otherwise, the

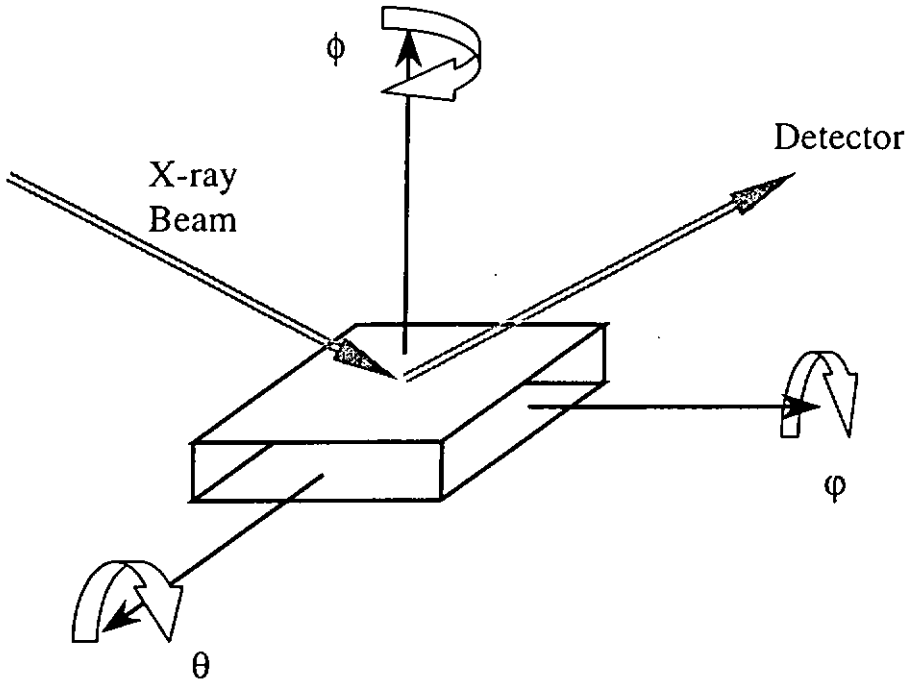

Fig.3.4 The rotation axes of the sample relative to the X-ray emitter and detector.

thin films grown are not epitaxial and are randomly oriented polycrystalline. Nonetheless, even if one set of planes from a single family of peaks in the θ-2θ scan is observed, we cannot guarantee that the films are epitaxially grown on the substrates. Since there is the possibility for poor plane-to-plane alignment such as twisting between planes, we can only say that the films are highly oriented in this direction.

The rocking curve, which is carried out by fixing the 2θ value of the selected peak and the angle θ is scanned for a few degrees, allows us to know the degree of orientation of the thin films fabricated. In other words, it can let us know how good the films are crystallized. The value of the Full Width at Half Maximum (FWHM) reflects the degree of the orientation of the thin films. A small value of the FWHM implies a high degree of orientation. Generally, a FWHM of ~1° is considered to be good oriented, and if it is ≤ 1°, the films can be said as highly oriented.

As mentioned before, if reflection peaks from a single family of planes in the θ-2θ scan are observed, it is not sufficient to say that the thin films are epitaxially grown. Therefore, 360° ϕ-scan is performed to ensure definitively that the films are epitaxially grown on the substrates. It is also used to determine whether the deposited films are lattice matched and "cube-on-cube" growth on the substrates.

For simple cubic structure, in carrying out the 360° ϕ-scan, the angle φ is tilted to 45°, fixing the 2θ and θ angles corresponding to the (220) planes of substrates or

films. Usually, higher order plane diffractions are used for good lattice matched substrate in order to obtain resolved peaks from the film and the substrate. From the 360° ϕ-scan profile, four diffraction peaks are observed and each of them is separated to 90°. They correspond to the (220), $(2\bar{2}0)$, (202) and $(20\bar{2})$ reflections. If the four peaks of the film have the same ϕ angles as those of the substrate, we can then say that the film has been cube-on-cube epitaxially grown on the substrate.

3.3.4 Electrical Properties of the Thin Films

3.3.4.1 Resistivity Against Temperature Measurements

The electrical properties of the deposited SVO and YBCO thin films were measured by the standard four-point-probe technique. After the thin films were deposited on the substrate, four gold top electrodes with equal spacing were sputtered on the film surface. Conducting wires were attached on the top electrodes using silver paint for connection to external measuring circuit. A constant current I was allowed to flow through the two outer electrodes. The voltage difference V between the two inner electrodes was measured. As a constant current was supplied to the film, the resistivity ρ of the thin film was calculated by:

$$\rho = \frac{V \times t \times C.F.}{I} \tag{3.3}$$

where t is the thickness of the film and C.F. is the correction factor. The correction factor for a circular sample (with a diameter d) and a rectangular sample (with the side parallel to the probe line as a and that perpendicular to the probe line as d) are given in Table 3.1 where s is the probe spacing [Tsai, 1988].

Table 3.1 Correction factor (C.F.) for the measurement of sheet resistances with the four-point-probe.

		Square	Rectangle		
d/s	Circle	*A/d* = 1	*a/d* = 2	*a/d* = 3	*a/d* ≥ 4
1.0				0.9988	0.9994
1.25				1.2467	1.2248
1.5			1.4788	1.4893	1.4893
1.75			1.7196	1.7238	1.7238
2			1.9475	1.9475	1.9475
2.5			**2.3532**	2.3541	2.3541
3.0	2.2662	2.4575	2.7000	2.7005	2.7005
4.0	2.9289	3.1127	3.2246	3.2248	3.2248
5.0	3.3625	3.5098	3.5749	3.5750	3.5750
7.5	3.9273	4.0095	4.0361	4.0362	4.0362
10.0	4.1716	4.2209	4.2357	4.2357	4.2357
15.0	4.3646	4.3882	4.3947	4.3947	4.3947
20.0	4.4364	4.4516	4.4553	4.4553	4.4553
40.0	4.5076	4.5120	4.5129	4.5129	4.5129
∞	4.5324	4.5324	4.5325	4.5325	4.5324

Note: The one high-lighted is the C.F. we used for our samples.

$$(\frac{a}{d} = \frac{1}{0.5} = 2\,;\ \frac{d}{s} = \frac{0.5}{0.2} = 2.5)$$

Fig.3.5 shows the constant current source circuit for the sample. A standard 747 operational amplifier configured in a negative feedback inverting amplifier mode was used to maintain a constant current flowing through the feedback loop even if the resistance of the sample changed widely. By adjusting the supply voltage or the values of the resistors, a constant current was obtained. In the present study, the constant current was kept at 1 mA. Fig.3.6 shows the constant current source circuit for the Pt thermometer which was used to monitor the sample temperature down to liquid nitrogen temperature of 77 K. Similarly, a constant current of 1 mA was maintained in this circuit. Therefore, the variation of the sample resistivity with temperature was measured by using these two constant current circuits.

3.3.4.2 Hysteresis (P-E) Loop Measurement

Owing to the noncentrosymmetric crystal-lattice structure (i.e. the center of all the positive charges does not coincide with that of the negative charges), electric dipole is formed in each crystal of the ferroelectric polycrystalline materials, such as PZT. For an as-prepared ferroelectric material, the electric dipoles orient randomly such that the resulting polarization of the material is almost zero. When a sufficiently high electric field is applied to a ferroelectric sample, the electric dipoles align along the electric field leading to a net polarization (P) and then polarization charges on the sample surface. When the electric field is removed, only a small number of the dipoles will switch back leaving a net permanent polarization (called remnant polarization P_r) in the sample. In order to reverse the resulting remnant polarization, an electric field higher than the coercive field E_c in opposite direction

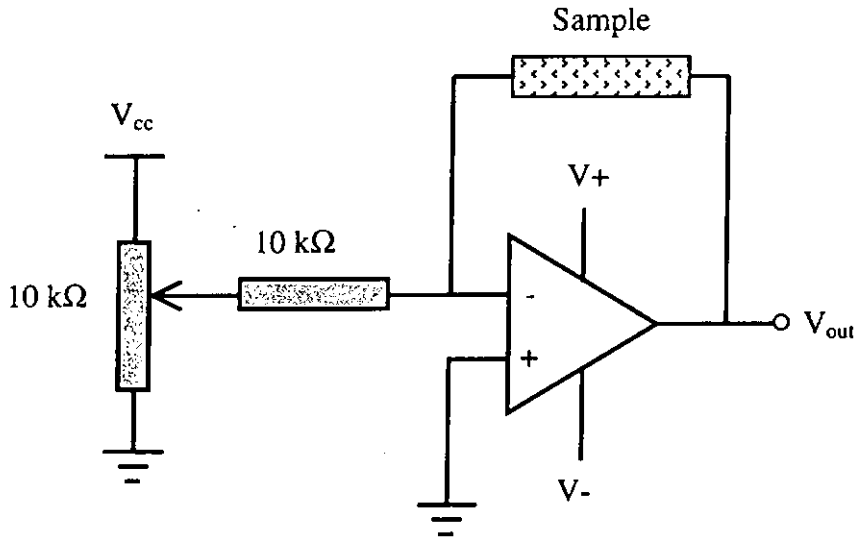

Fig.3.5 The constant current circuit for the sample.

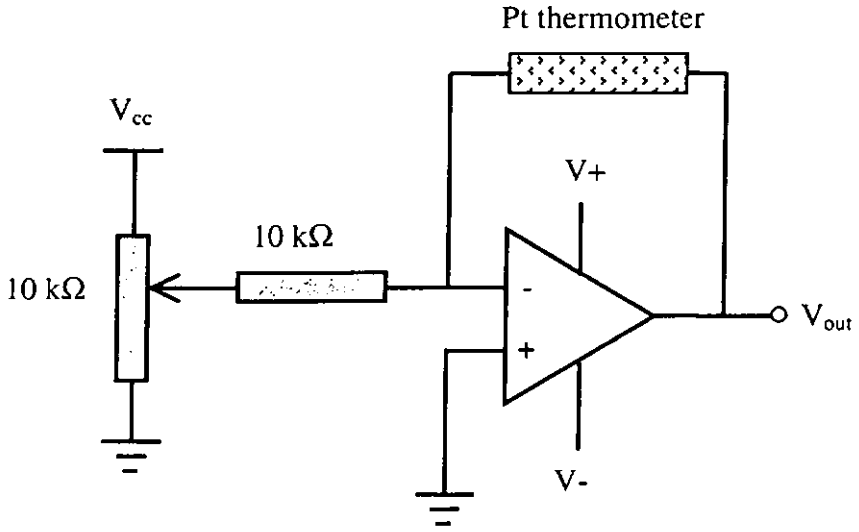

Fig.3.6 The constant current circuit for the thermometer.

has to be applied. By measuring the polarization charges generated on the sample surface upon the application of an electric field, a hysteresis loop of polarization (= surface density of polarization charges) versus applied field is observed. A typical polarization hysteresis loop is shown in Fig.3.7.

In the present study, a standardized ferroelectric test system (RT-66A, Radiant Technology), operating in the virtual ground mode was used to measure the hysteresis loop measurement (Fig.3.8). A one-cycle triangle-wave form of magnitude V and 9Hz (Fig.3.9) was applied to the sample of which the other surface was maintained at zero volts. The generated polarization charge (Q) was collected by an integrator. The electric field across the sample (E) and the induced polarization (P) were calculated as:

$$E = \frac{V}{d} \tag{3.4}$$

$$P = \frac{Q}{A} \tag{3.5}$$

where A and d are the surface area and thickness, respectively, of the sample.

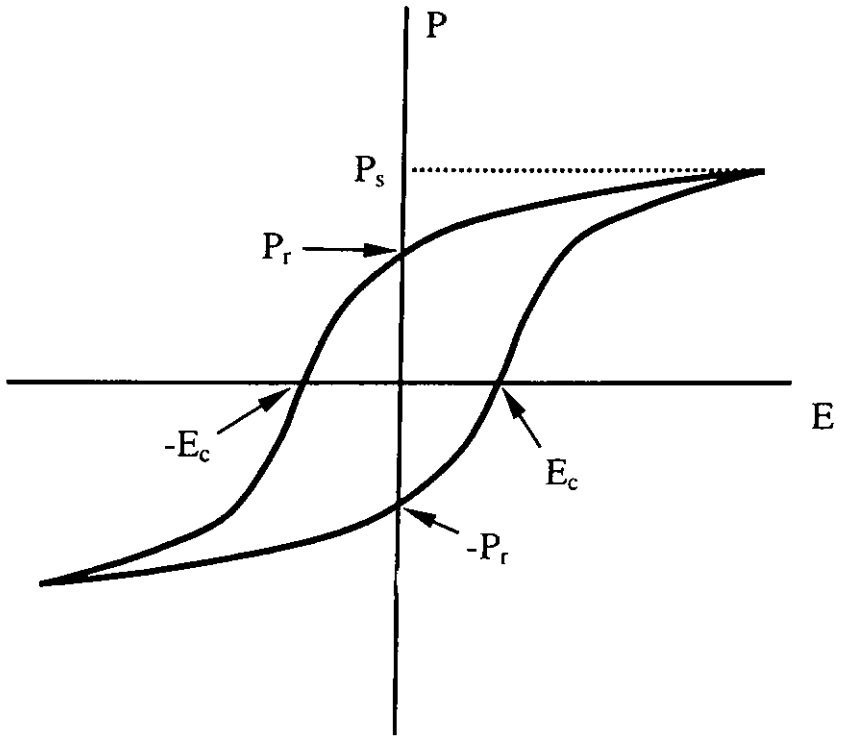

Fig.3.7 A typical hysteresis loop of polarization versus applied field. P_s is the saturation polarization, P_r is the remnant polarization, and E_c is the coercive field.

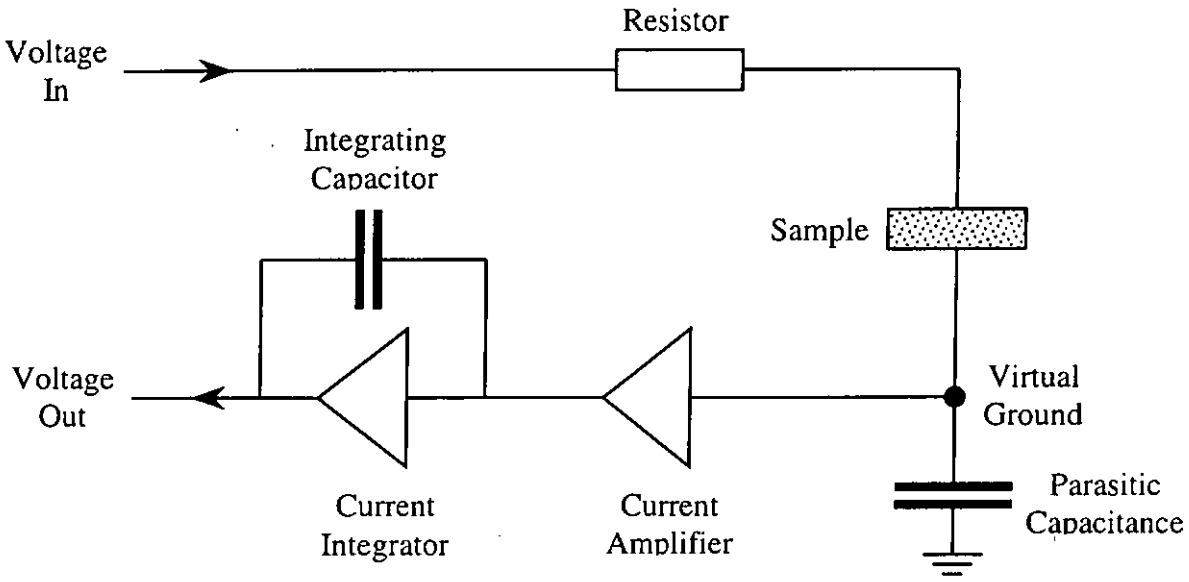

Fig.3.8 Schematic setup for measuring the hysteresis loop using a RT66A tester, operating in the virtual ground mode.

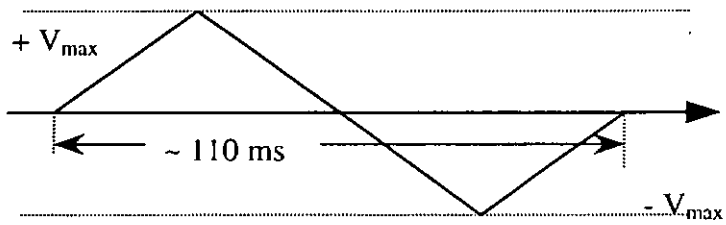

Fig.3.9 Schematic diagrams of the signals used in the hysteresis polarization

3.3.4.3 Fatigue Test

Fatigue is defined as the loss of the switchable polarization with continuous switching of a ferroelectric material. In the present study, the fatigue tests were carried out using a RT66A ferroelectric tester. A bipolar square wave of 9 V and frequency 25 kHz (Fig.3.10a) was applied to the sample. The cycling was periodically interrupted and a pulse polarization measurement was made. In the pulse polarization test, five triangular pulses (Fig.3.10b) were applied to the sample and the switched polarization $\pm P^*$ and nonswitched polarization $\pm P^\wedge$ (Fig.3.10c) were determined. P^* was determined after subjecting the capacitor to two triangular pulses of opposite polarities whereas $P^\wedge$ was determined after subjecting the capacitor to two triangular pulses of the same polarity. The difference between P^* and $P^\wedge$ denoted the switchable polarization.

3.3.4.4 Current-voltage Characteristics and Dielectric Constant

The dielectric constant of the PZT capacitors was measured using an impedance analyzer (HP 4194A), while the current–voltage characteristic was measured using an electrometer (TR8652). Patterned top electrodes produced by shadow mask method were used to facilitate these measurements.

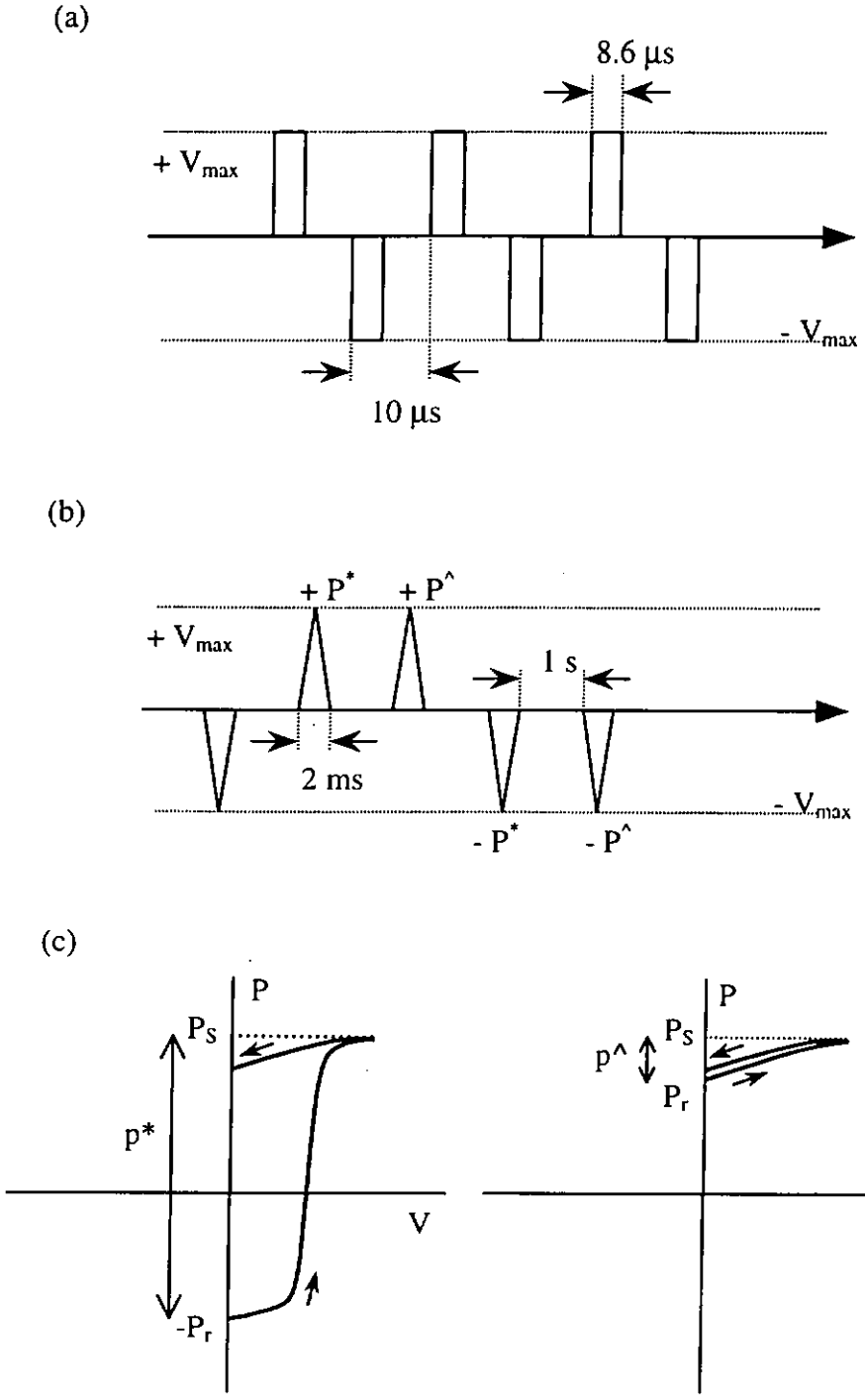

Fig.3.10 Schematic diagrams of the (a) signal used in fatigue test; (b) pulse train used to measure the pulse polarization of the capacitors; (c) switched polarization (+P*) and non-switched polarization (+P^).

Chapter 4

Fabrication and Characterization of $SrVO_3/LaALO_3$ and $SrVO_3/TiN/Si$

4.1 Introduction

Currently, there is great interest in fabricating highly conducting oxide films for use as electrodes in applications such as ferroelectric capacitor and solid-oxide fuel cell. Commonly used conducting oxides include $YBa_2Cu_3O_{7-x}$, $La_{1-x}Sr_xCoO_3$, and doped lanthanum manganates. $SrVO_3$ (SVO) has a perovskite cubic structure with a lattice constant of 3.84 Å. It is known to have very low electrical resistivity and is therefore a suitable material for conducting oxide electrodes. Indeed it has been reported that the high quality SVO films can be fabricated on oxide single crystal substrates and resistivities of the order of μΩ-cm have been achieved [Ritums et al., 1998]. SVO films directly grown on Si substrates have also been attempted. Only poor crystalline structure and high resistivity films, however, have been obtained [Ritums et al., 1998; Nagata et al., 1992]. SVO films grown on Si through thin buffer layers of Sr [Moon et al., 1996] and yttria-stabilized zirconia (YSZ) [Ritums et al., 1998] have been reported. High quality epitaxial films have been demonstrated at substrate temperature of 650°C. This relatively high deposition temperature, however, is incompatible with the processing temperature of about 500°C commonly used in Si fabrication technology.

In this chapter, we present the results of fabricating SVO thin films on $LaALO_3$

(LAO) and TiN buffered Si by pulsed laser deposition (PLD) method. Very high quality epitaxial SVO films grown on LAO substrates have been obtained and resistivities of 3 μΩ-cm and 19 μΩ-cm were recorded at 77 K and 300 K respectively. High quality heteroepitaxial SVO/TiN/Si structures have also been fabricated and a low processing temperature of 550°C has been demonstrated.

4.2 Structural Analysis of $SrVO_3$ Films

4.2.1 $SrVO_3$ (SVO) Target Fabrication

SVO target was fabricated by using the standard solid state reaction method. Chemicals of vanadium oxide (V_2O_5) and strontium carbonate ($SrCO_3$) were used. Since the ratio of strontium (Sr) to vanadium (V) is 1 for the SVO target, the required masses for V_2O_5 and $SrCO_3$ can be calculated as follows:

Molar mass of

V_2O_5 : 181.88

$SrCO_3$: 147.63

For V_2O_5, the required mass is calculated as follows:

181.88 / (2 * 99%) = 91.8568

91.8568 / 10 = 9.18586

9.18586 / 2.5 = 3.67g

Similarly, the required mass of $SrCO_3$ is calculated as follows:

147.63 / 99% = 149.1212

149.1212 / 10 = 14.91212

14.91212 / 2.5 = 5.96g

After the desired proportion of oxides was weighed, they were well mixed by a mortar and a pestle for about 1 hour. The powders were then put into an alumina crucible and covered with a lid. The whole assembly was heated to 850°C at a rate of 3°C/min in a high temperature furnace for calcination. After heated at 850°C for 5 hours, the sample was cooled down to room temperature slowly. The resulting SVO compound (in the form of a block) was then crushed and ground by a mortar and a pestle for about 1 hour. In order to ensure the homogenity and complete calcination of the compound, it was re-calcinated at 850°C in the furnace for 5 hours. The resulting compound was then re-ground into fine powder. Afterwards the powder was pressed into circular pellets of diameter 22 mm and thickness 5 mm, using a pressure of about 1000 kg/cm^2. The pellets were sintered at 950°C in the furnace for 5 hours. The structure of the resulting SVO target was characterized by an X-ray diffractometer.

4.2.2 Substrate Temperature Dependence

4.2.2.1 $SrVO_3$/LAO

SVO films were grown on LAO substrate at deposition temperatures ranging from 450°C to 750°C. The ambient oxygen pressure was kept between 10^{-6} and 10^{-2} Torr. Except for those deposited at high vacuum of 10^{-6} Torr, all SVO films showed poor crystallinity and high resistivity. So, in all subsequent studies, SVO films were grown at 10^{-6} Torr ambient pressure. Fig.4.1 shows the θ-2θ scans of the films deposited at 750°C, 650°C, 550°C and 450°C. Apart from the film grown at 450°C (Fig. 4.1(iv)), all the as-deposited films are well crystallized. This is evident from

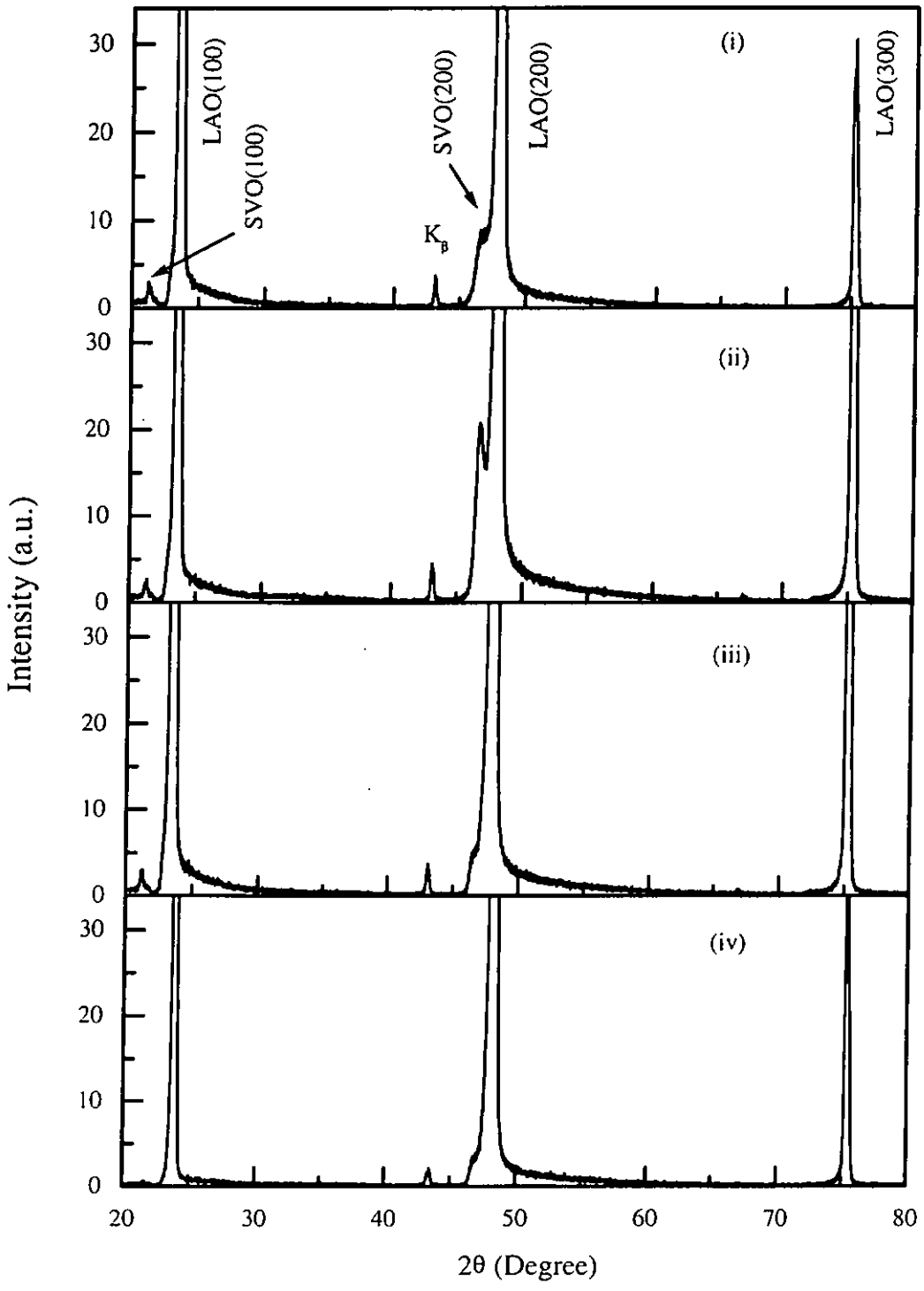

Fig. 4.1 X-ray θ-2θ diffraction patterns for the SVO/LAO structure with the SVO layer grown under high vacuum and deposition temperature as follows: (i) 750°C, (ii) 650°C, (iii) 550°C, and (iv) 450°C.

the presence of the sharp and well-defined diffraction peaks. As shown in Fig.4.1, only strong (h00) reflection peaks are observed, no trace of other SVO reflections is observed. This suggests that highly oriented SVO films can be obtained at temperature of 550°C or above. Actually, the crystallinity obtained for the SVO films is very good as indicated by the narrow X-ray ω-scan rocking curves of the (200)SVO reflection. For example, for the SVO film deposited at 650°C, the full width at half maximum (FWHM) is about 0.7°. The small K_β peaks observed for all the films are due to the diffraction of the K_β line of the X-ray by the LAO substrate (Fig.4.1).

In fact, a film can be grown on a substrate in an excellent orientation to the normal of the surface, but poor in the in-plane orientation as twisting between planes can occur. Therefore, in order to determine whether the SVO films were epitaxially grown on the substrate, 360° ϕ-scans for the (220)SVO and (220)LAO were also carried out. It was used to confirm the in plane alignment of the films to the substrates.

Fig.4.2 shows the X-ray 360° ϕ-scans on (220)SVO and (220)LAO planes with which the film was deposited at 650°C. It is seen that four sharp peaks separated at 90° interval appear indicating the four-fold symmetry of a typical cubic structure. The two sets of the reflections occur at the same diffraction angle suggesting a cube-on-cube expitaxial growth of SVO films on LAO substrate. For films deposited at higher temperatures, similar results are observed.

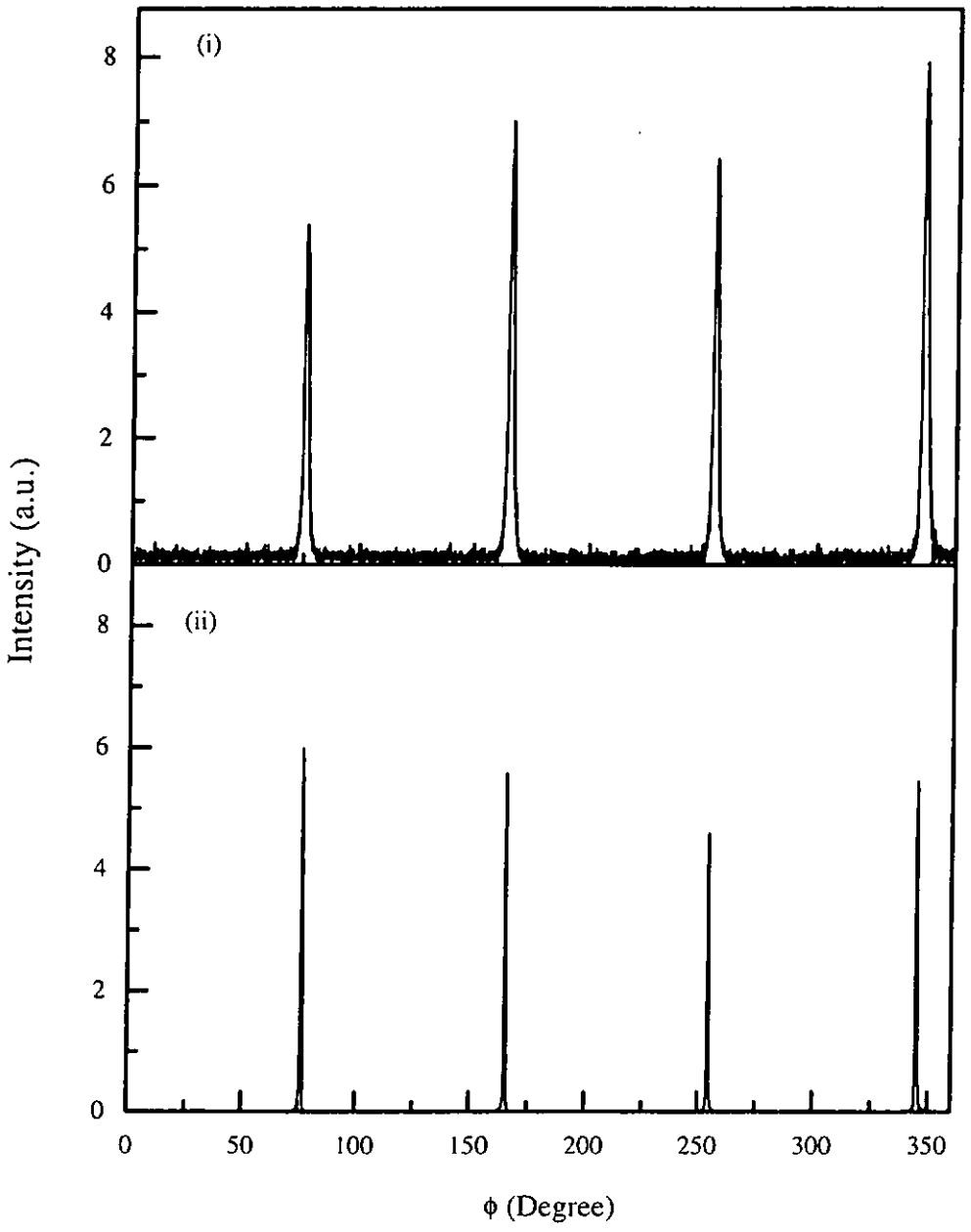

Fig.4.2 360° ϕ-scans diffraction patterns of (i) (220)SVO, and (ii) (220)LAO.

4.2.2.2 $SrVO_3$/TiN/Si

In view of the fact that SVO films have such good crystal quality, it will be very interesting and useful if SVO can be grown on Si substrate for integrated device applications. However, it was observed that if SVO was directly grown on Si substrate, the film had poor crystallinity and high resistivity due to lattice-mismatched and chemical diffusion. Moon et al. [1996] has shown that the VO_2 was reduced by silicon to metallic vanadium when SVO was directly grown on Si substrate. Therefore, TiN was used as the buffer layer in the present work. It provides not only a lattice-matched site for subsequent SVO film growth, but also a good chemical diffusion barrier. Fig.4.3 shows the X-ray photoelectron core level spectrum of V 2p and O 1s of the as-grown film deposited at 550°C under high vacuum. In a perovskite SVO structure, the vanadium should be tetravalent. The binding energy of V^{4+} and V^{5+} are 516.3 eV and 517.6 eV, respectively. Our XPS results suggest that our SVO films composed of both V^{4+} and V^{5+}. The measured ratio of the V/Sr by XPS is 1.30/1.48, which is close to the nominal composition of 1/1.

Fig.4.4 shows the X-ray θ-2θ diffraction patterns for the SVO/TiN/Si heterostructure deposited at substrate temperatures of 750°C, 700°C, 650°C, 600°C and 550°C. It is seen that highly oriented SVO films with strong (h00) reflections are prepared. The crystallinity of the film improves as the substrate temperature increases. Fig.4.5 and Fig.4.6 show the X-ray ω-scan rocking curves on the (200) reflection of the SVO and TiN films deposited at 550°C, respectively. Their FWHM

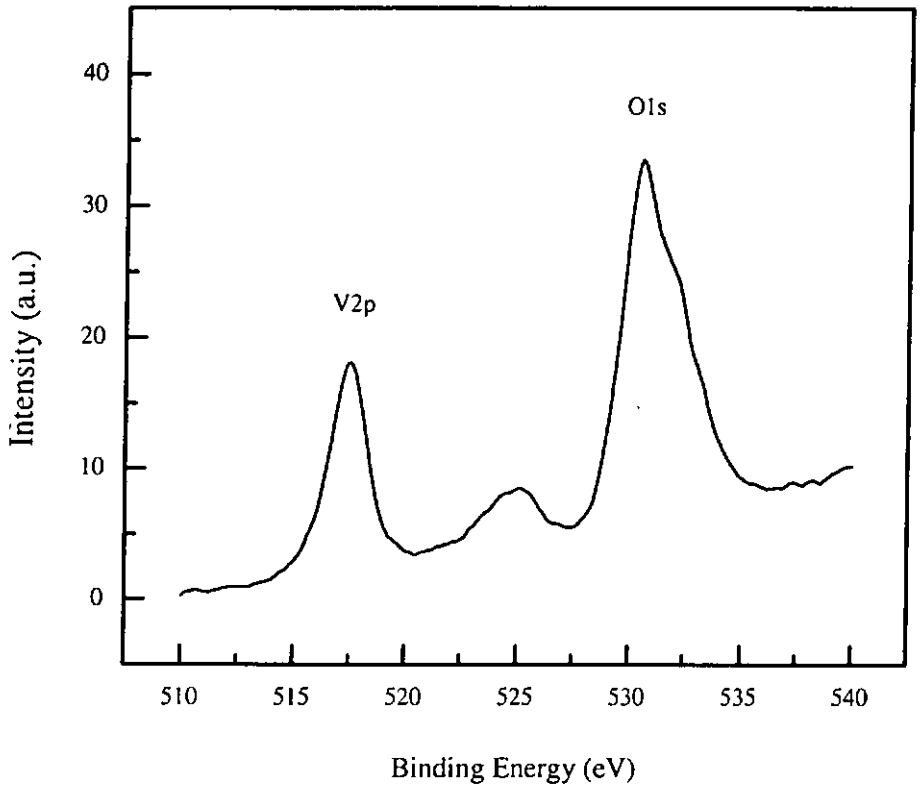

Fig.4.3 X-ray photoelectron core level spectrum of V 2p and O 1s of the as-grown film deposited at 550°C under high vacuum.

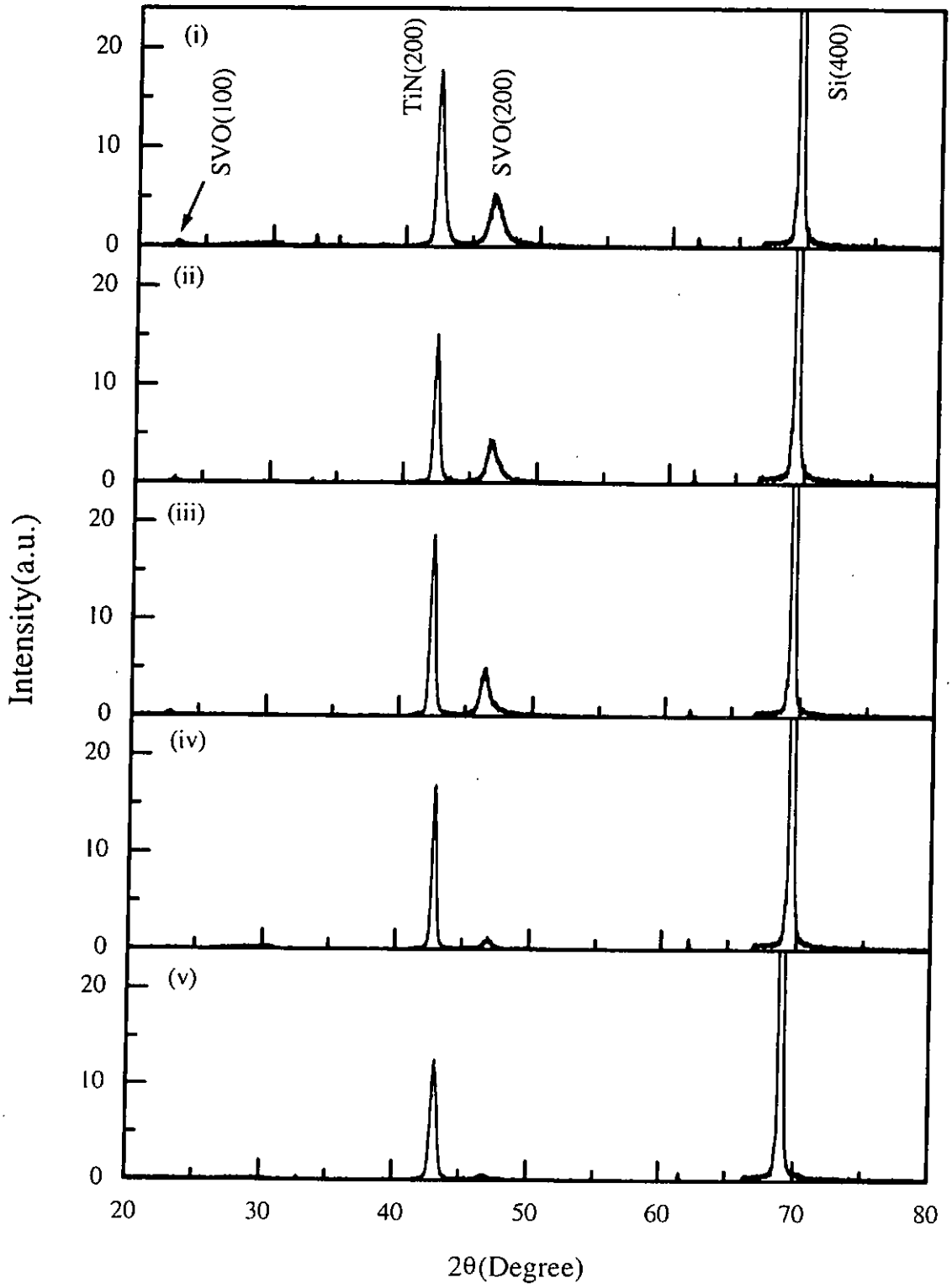

Fig.4.4 X-ray θ-2θ diffraction patterns for the SVO/TiN/Si structure with the TiN layer deposited at 550°C under high vacuum. The SVO layer was deposited at (i) 750°C, (ii) 700°C, (iii) 650°C, (iv) 600°C, and (v) 550°C.

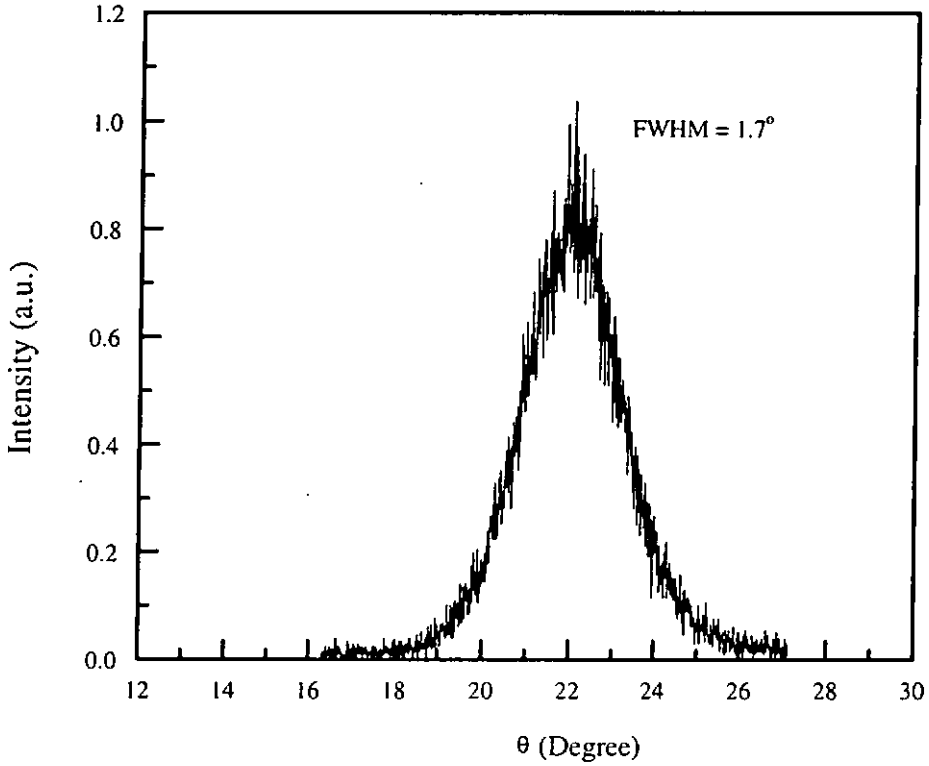

Fig.4.5 Rocking curve of (200)SVO reflection of the as-deposited SVO film grown on TiN buffered Si substrate. The deposition conditions for both of the SVO and TiN layers were under high vacuum and with deposition temperature of 550°C.

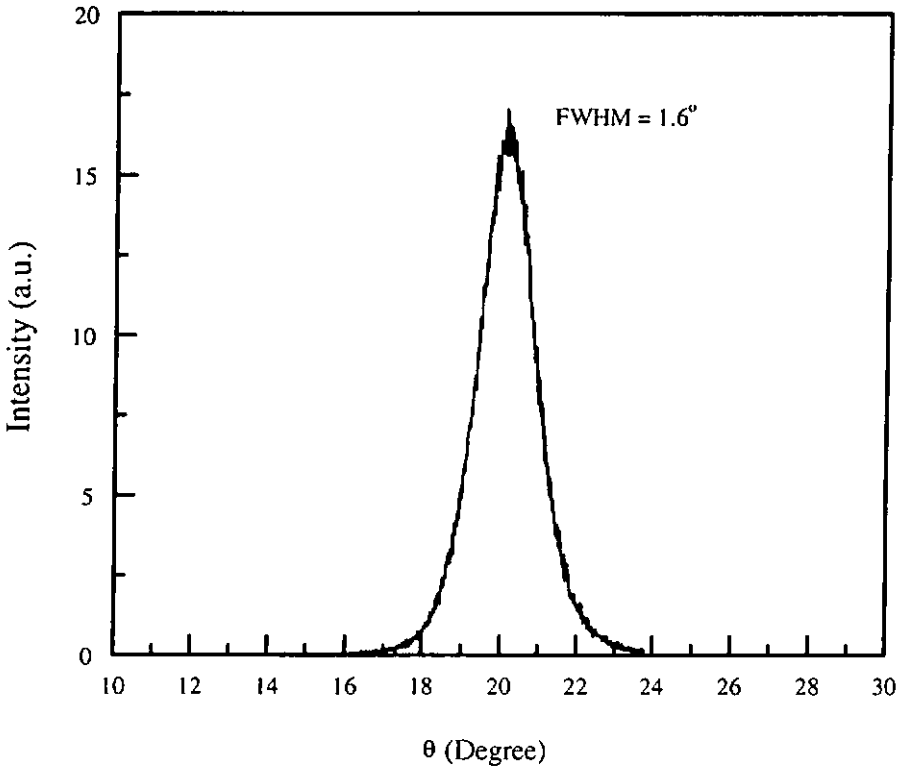

Fig.4.6 Rocking curve of (200)TiN reflection of the buffered TiN film of the SVO/TiN/Si heterostructure. The deposition conditions for both of the SVO and TiN layers were under high vacuum and with deposition temperature of 550°C.

are about 1.7° and 1.6°, respectively, indicating that they are well oriented. Fig.4.7 shows the X-ray 360° ϕ-scans on the (220)SVO, (220)TiN and (220)Si diffraction. Both the TiN and SVO films were deposited at 550°C. The characteristic four-fold symmetry is observed and cube-on-cube epitaxial growth is suggested. The low temperature processing of the SVO/TiN/Si heterostructure is important for developing integrated devices on Si.

4.2.2.3 Cross-section and Surface Morphology of the $SrVO_3$/LAO and $SrVO_3$/TiN/Si

In order to investigate the thickness and smoothness of the films, scanning electron microscopy (SEM) measurements were carried out. Fig.4.8a and Fig.4.8b show the SEM micrographs of the cross-section of the SVO/LAO and SVO/TiN/Si structures, respectively. The thickness of the SVO film deposited on LAO substrate is about 375 nm and those of the SVO film and TiN buffer layer deposited on Si substrate are about 250 nm and 200 nm, respectively. It is also seen that sharp interfaces between the SVO, TiN, and Si layers are observed (Fig.4.8b).

Fig.4.9a and Fig.4.9b show the surface morphology of the SVO films deposited on LAO substrate and TiN buffered Si substrate, respectively. It is seen that the surfaces are quite smooth. As shown in the atomic force microscope (AFM) topographic image (Fig.4.10), the surface roughness of the corresponding SVO/TiN/Si film (Fig. 4.9b) is about ±4 Å.

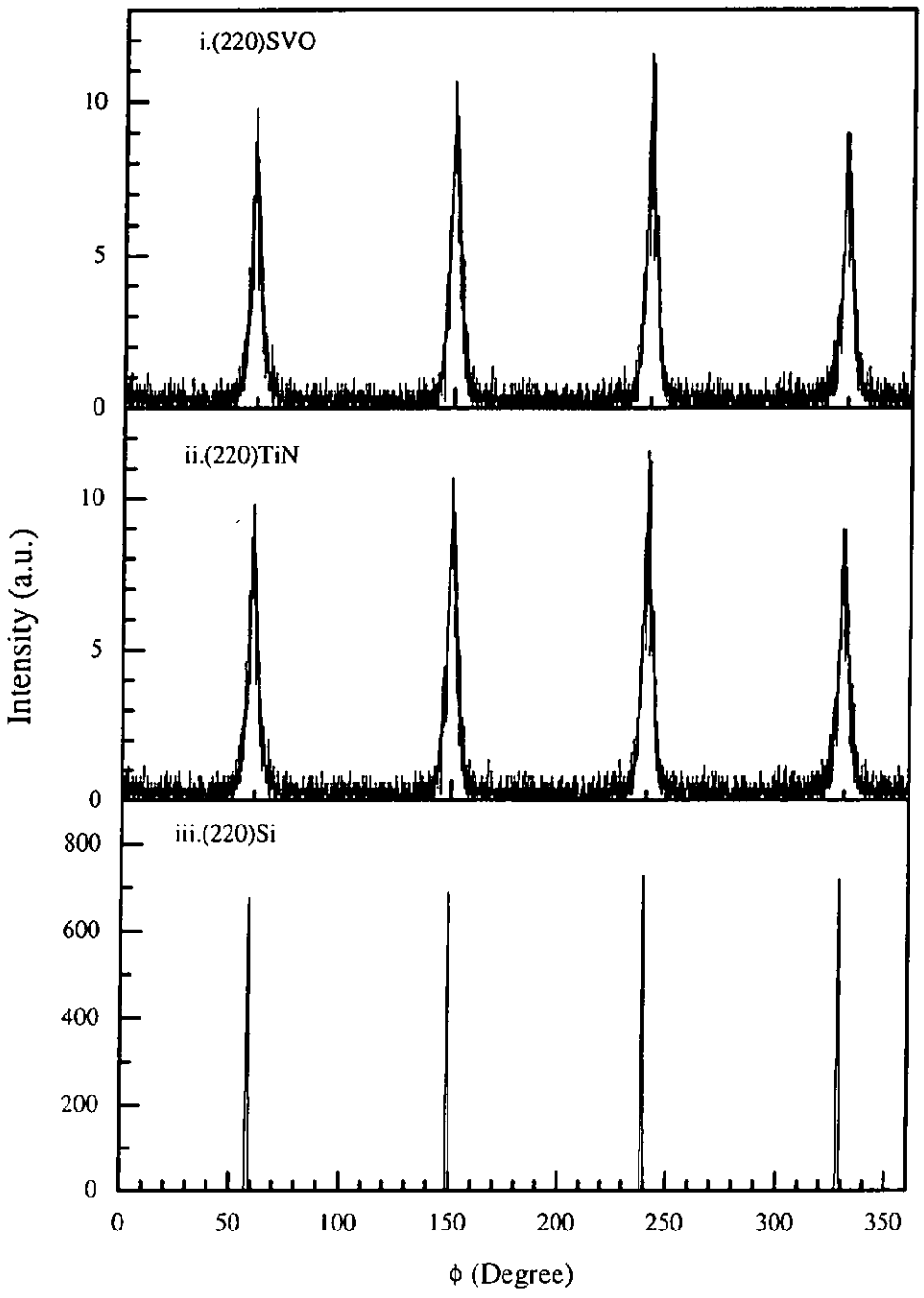

Fig.4.7 360° ϕ-scans diffraction patterns of (i) (220)SVO, (ii) (220)TiN, and (iii) (220)Si.

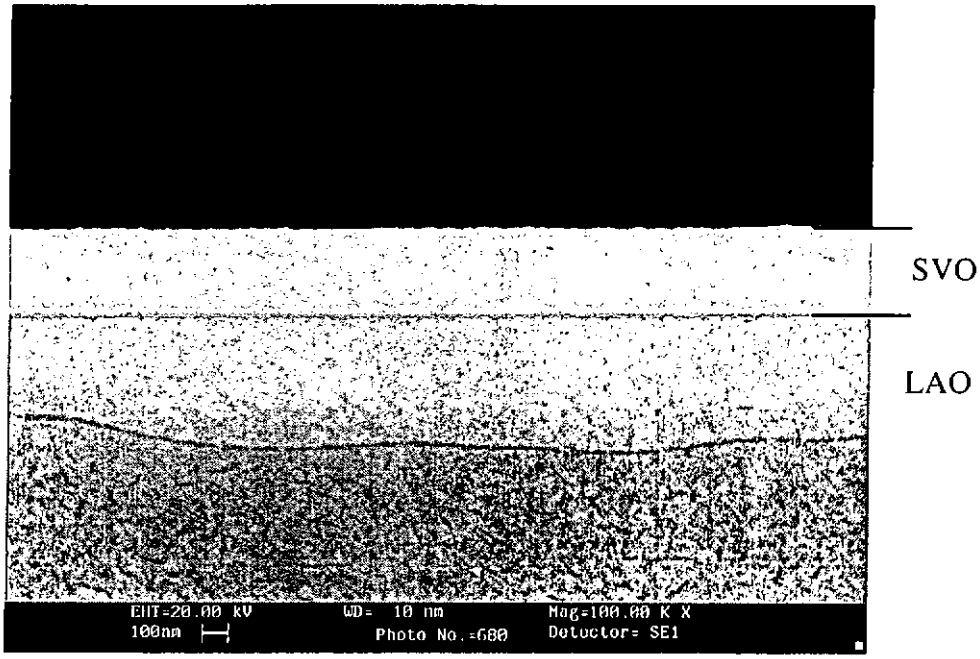

(a)

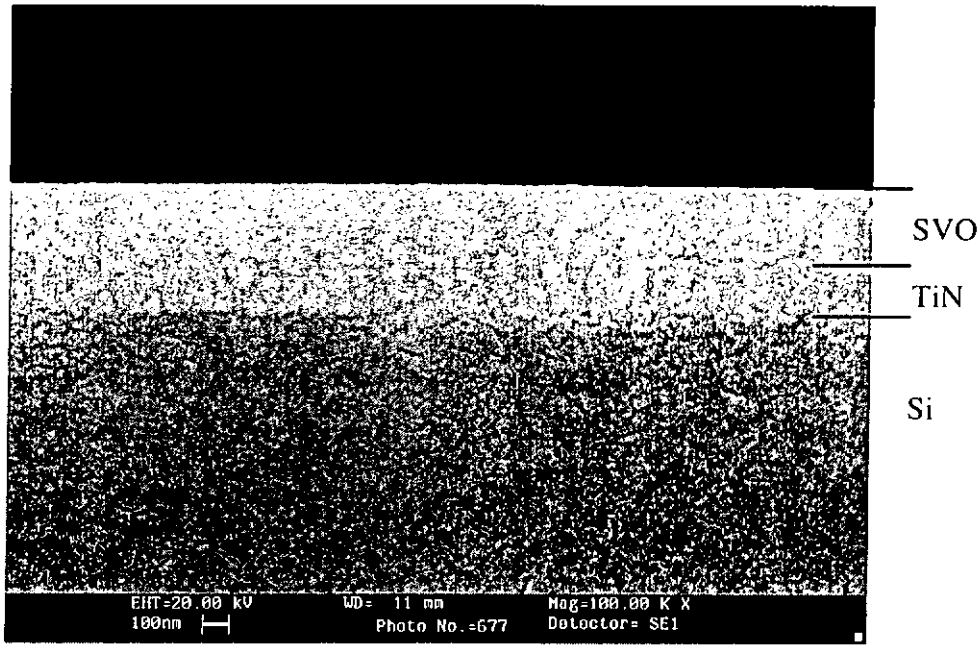

(b)

Fig.4.8 Scanning electron micrographs of the cross-section of the (a) SVO/LAO and (b)SVO/TiN/Si. Both SVO and TiN layers were deposited under a pressure of 4 x 10^{-6} Torr. The deposition temperatures of them are 600°C and 550°C respectively.

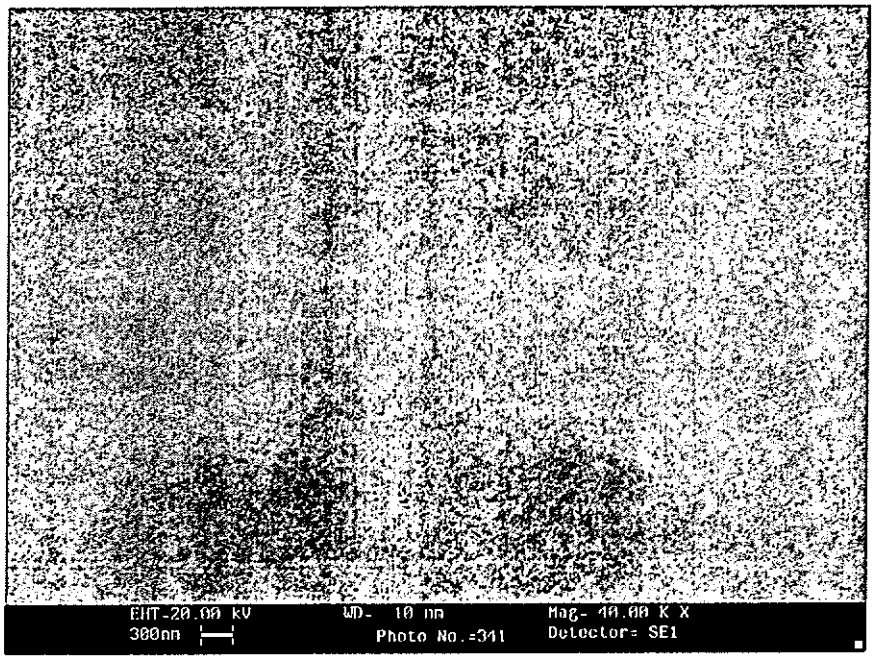

(a)

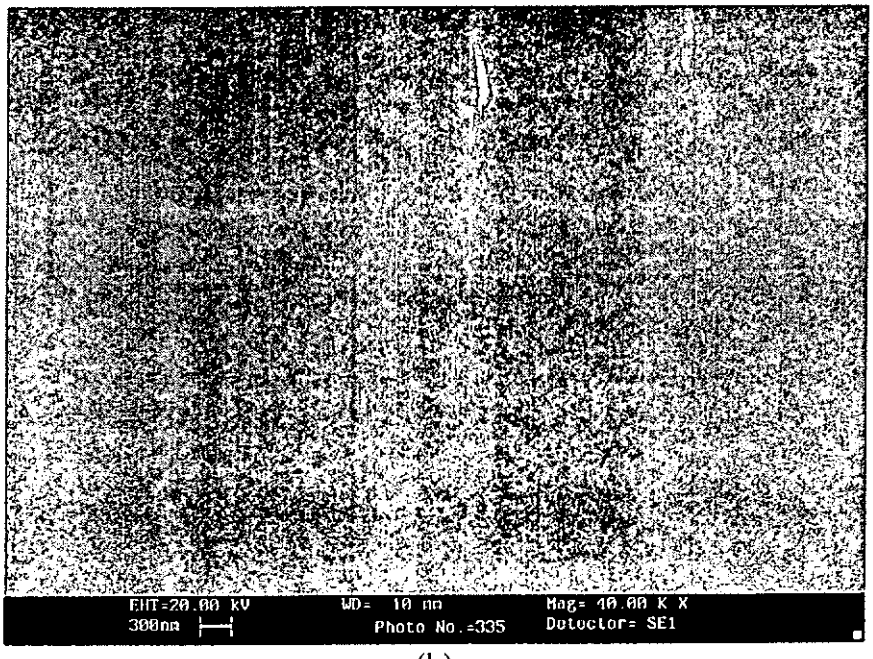

(b)

Fig.4.9 Surface morphology of the SVO films deposited on (a) LAO and (b) TiN/Si. Both SVO and TiN layers were deposited under a pressure of 4 x 10^{-6} Torr. The deposition temperatures of them are 600°C and 550°C respectively.

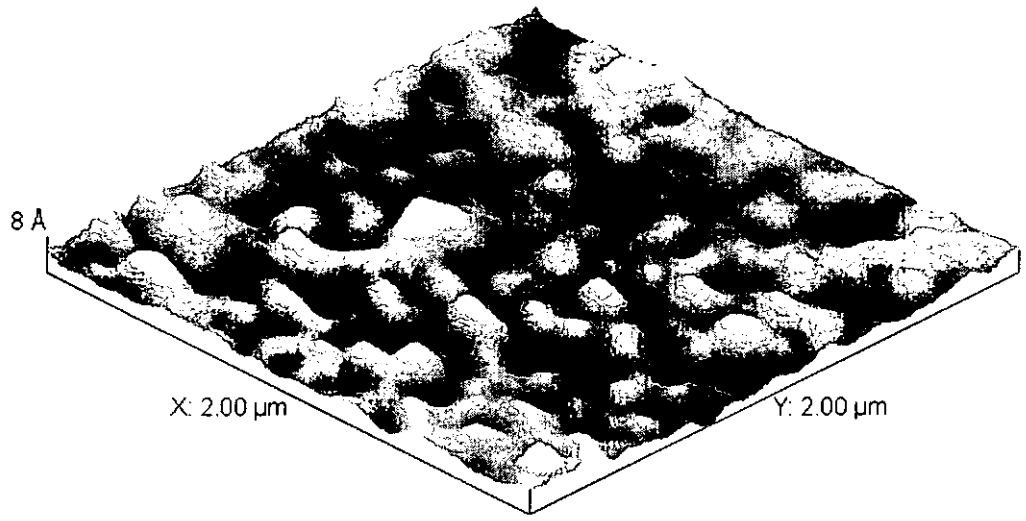

Fig.4.10 AFM topographic image of the $SrVO_3$ film deposited at a substrate temperature of 600°C.

4.3 Post Deposition Annealing Effects under Different Ambient Oxygen

In order to evaluate the effects of ambient oxygen pressure on the structure and properties of SVO films, as-deposited films grown under high vacuum and at deposition temperature of 750°C were in-situ annealed under different ambient oxygen pressures for 20 minutes. Fig. 4.11 shows the X-ray θ-2θ diffraction patterns for the SVO/LAO film annealed under different ambient oxygen pressures. It is clearly seen that the process of post deposition annealing has significant effects on the crystallinity of the SVO thin films. It is seen that as the annealing oxygen pressure increases, the (100)SVO and (200)SVO reflection peaks become smaller, suggesting a poor crystallinity. The peaks almost disappear when the annealing oxygen pressure is '66 mTorr and have the sharpest reflection at a certain low annealing ambient oxygen pressure, i.e. 10 mTorr. This phenomenon may be explained by the heat convection. Under higher annealing ambient oxygen pressure, the temperature of substrate becomes lower than the temperature of the heater due to heat convection. Therefore, the crystallinity of the SVO films becomes poor as a result of a lower annealing temperature. On the other hand, we can see from Fig.4.11 that the crystallinity of the film starts to deteriorate as the annealing pressure is reduced to 10^{-6} Torr. This may be explained by the fact that at such low pressure, the oxygen stoichiometry of the SVO films becomes so poor that it affects the crystallinity.

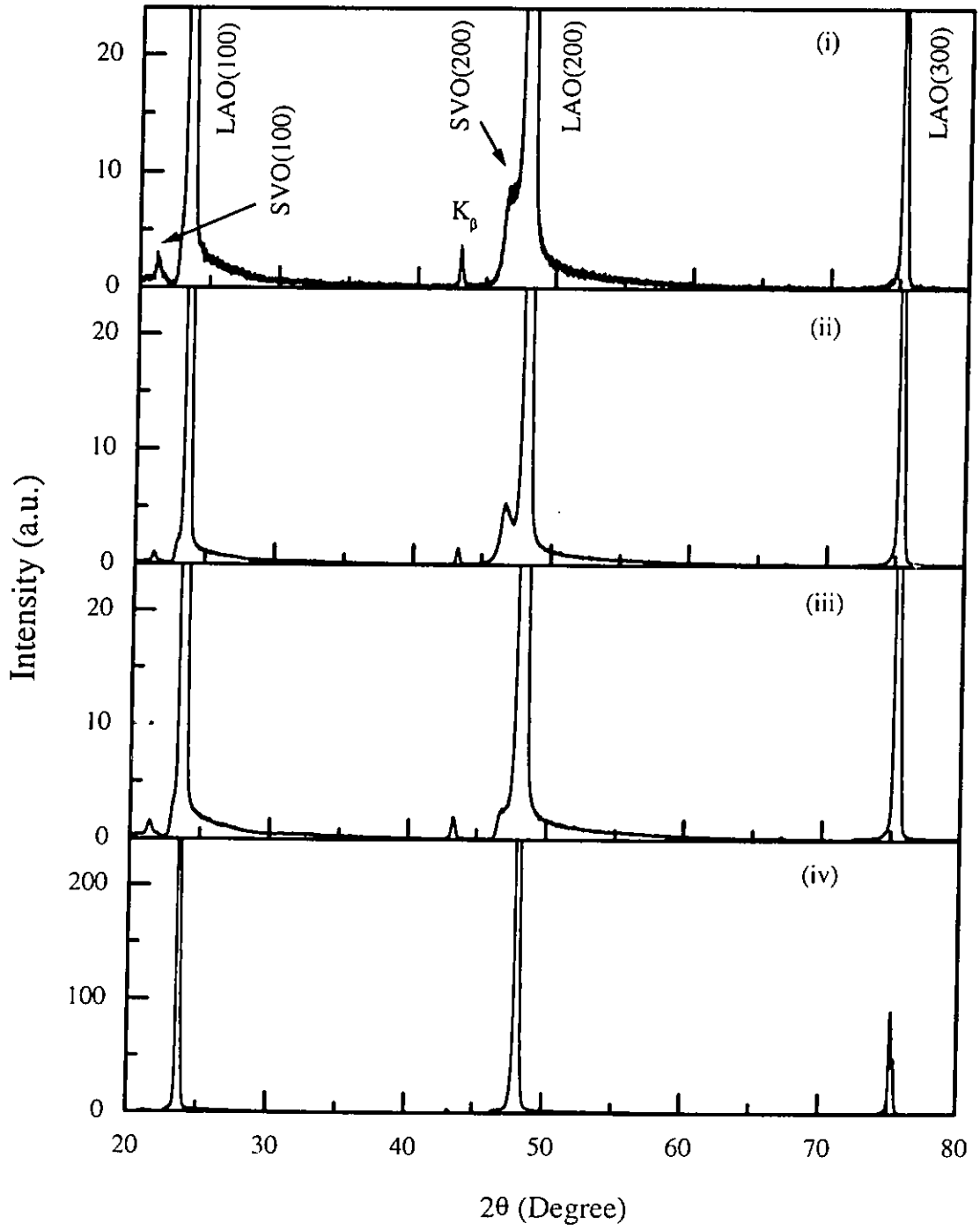

Fig.4.11 X-ray θ-2θ diffraction patterns for the SVO/LAO structure with the SVO layer grown under high vacuum and deposition temperature of 750°C. After the film deposition, it was annealed at 750°C under different ambient oxygen pressure for 20 minutes: (i) 10^{-6} Torr, (ii) 10 mTorr, (iii) 35 mTorr, and (iv) 166 mTorr.

4.4 Electrical Property of $SrVO_3$ Thin Films

The deposition temperature has a distinct effect on the electrical property of the SVO films. Fig. 4.12 shows the temperature dependence of resistivity of the SVO films deposited on LAO substrate at different deposition temperatures: 550°C, 600°C, 650°C and 700°C. Apparently, the SVO films are of good metallic properties. It is also seen that the resistivity of the SVO film decreases as the substrate temperature increases. This trend is probably due to the improved crystallinity of the SVO thin films at higher deposition temperature.

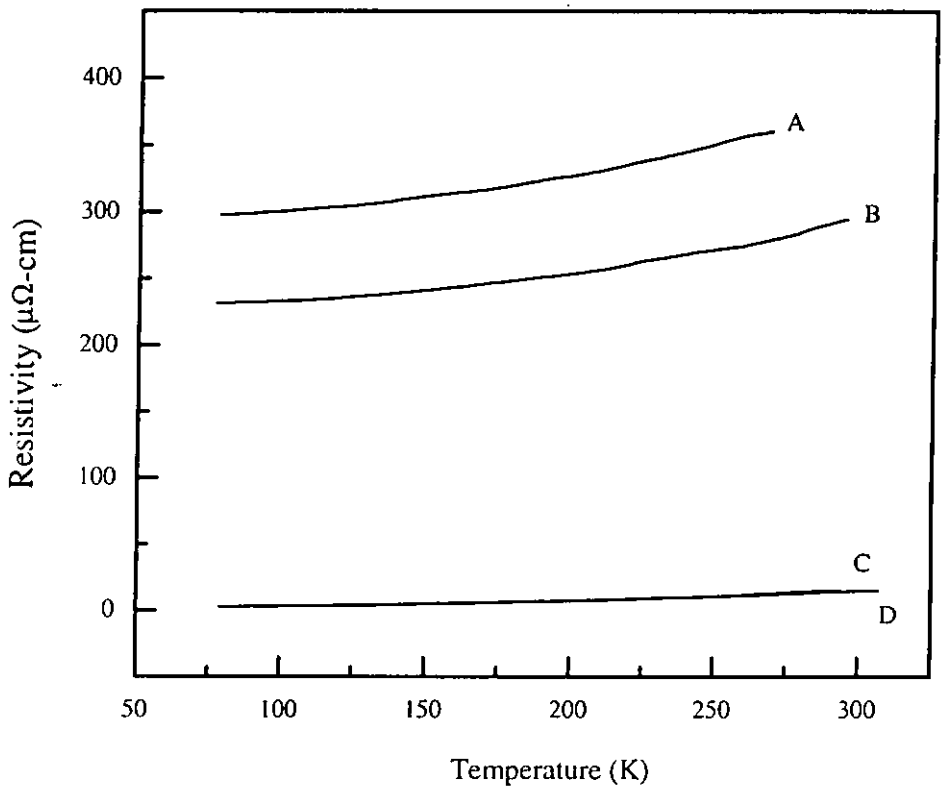

Fig.4.12 Resistivity against temperature of SVO films deposited on LAO substrate at 550°C (Curve A), 600°C (Curve B), 650°C (Curve C), and 700°C (Curve D).

Chapter 5

Fabrication and Characterization of $YBa_2Cu_3O_{7-x}$ (YBCO) Films on Si Substrates Using STO/TiN Buffer Layers

5.1 Introduction

YBCO, one of the most widely studied high temperature superconducting materials, belongs to Type II class of superconductors which are characterized by their ability to retain their superconducting properties in very high magnetic fields.

Numerous attempts have been made to incorporate YBCO into the existing silicon integration technology [Hao et al., 1994] for superconducting and other microelectronic applications. Nonetheless, the deposition of YBCO directly on silicon will damage the electrical properties of the silicon surface and the superconductivity of YBCO due to the out-diffusion of elements in YBCO and the large lattice mismatch (Si, a = 5.43 Å; YBCO, a = 3.82 Å, b = 3.89 Å, c = 11.68 Å.) Therefore, a buffer layer inserted in between the Si and YBCO is necessary to prevent the barium and copper in the stoichiometric YBCO compound from diffusing into the silicon substrate. Actually, the use of these buffer layers between YBCO and Si not only serves to stabilize the YBCO/Si structure, but also provides either an electrical insulation or a conduction channel in this mutilayer system. Different oxide and conducting buffers such as yttria-stabilized zirconia (YSZ) [Liu

et al., 1999; Hwang et al., 1995; Jeong et al., 1998; Juang et al., 1994], MgO [Fork et al., 1991], $SrTiO_3$ [Cheung et al., 1992], CeO_2 [Luo et al., 1991], and SiO_2 [Gupta et al., 1988] have been used. In fact, the stability of this layered structure is determined to a large extent by the properties of the buffer layer and its interfaces with YBCO and Si.

In this chapter, we present the work on fabrication of integrated epitaxial YBCO thin films on Si by the PLD method using STO and TiN as buffer layers. Heteroepitaxial structures of TiN/Si, STO/TiN/Si and YBCO/STO/TiN/Si have been prepared and their structural and electrical properties are discussed.

5.2 Characterization of TiN/Si and STO/TiN/Si

5.2.1 TiN/Si

TiN has a cubic NaCl-type structure with a lattice constant of 4.24 Å for stoichiometric material. It has many unique properties such as high electrical conductivity, high chemical stability, hardness and abrasion resistance. Therefore, it has found wide applications in wear- and abrasion-resistant coating, atomic diffusion barrier and contact formation in advanced LSI technologies. Narayan et al. [1992] showed that the resistivity of an epitaxial TiN layer formed on Si as measured by a four-point-probe technique was very low (15-17 μΩcm) at room temperature and showed a metallic behavior. Therefore, it can also be used to form ohmic contacts in the source and the drain regions of a metal-oxide semiconductor (CMOS) device.

In view of the fact that TiN has such excellent diffusion barrier properties and can be epitaxially grown on Si, it is of interest to use it as a buffer layer for integrating YBCO on Si, which has a lattice constant of 5.43 Å. Although there is a large difference in lattice constant between TiN and Si, TiN has been shown to grow epitaxially on Si via domain matching epitaxy [Tsvetanka Zheleva et al., 1994] in which four lattice constants of TiN match with three of Si. Actually, for domain matching epitaxy, the lattice misfit is about 4.0%. Besides, epitaxial growth of TiN films on Si were obtained in a wide range of substrate temperatures from 500°C to 750°C [Leung, 1998]. Post-deposition annealing of TiN films was not necessary.

In the present work, the TiN buffer layers were fabricated by ablating a TiN target bought from Electronic Space Products International (ESPI) company (grade 2N5). All of the TiN films were prepared at 600°C and 720°C under a pressure of $4x10^{-6}$ Torr. The laser fluence, repetition rate and deposition time used are 3 J/cm^2 10 Hz and 20 minutes respectively. The thickness of the TiN films, as measured by the profiler and cross-section SEM imaging was about 200 nm.

Fig.5.1 shows the X-ray θ–2θ diffraction pattern of the TiN film deposited at 600°C under a pressure of $4x10^{-6}$ Torr on (100)Si substrate. A single sharp peak of (200)TiN is observed indicating a single phase of the TiN film. The FWHM of the (200)TiN reflection is about 1.71° (Fig.5.2) suggesting that the crystal of the film is highly oriented. In order to determine whether the TiN film was epitaxially grown on the Si substrate, 360° ϕ-scans of the (220)TiN and (220)Si reflection peaks were carried out. Fig.5.3 shows their corresponding 360° ϕ-scans profiles. Four sharp

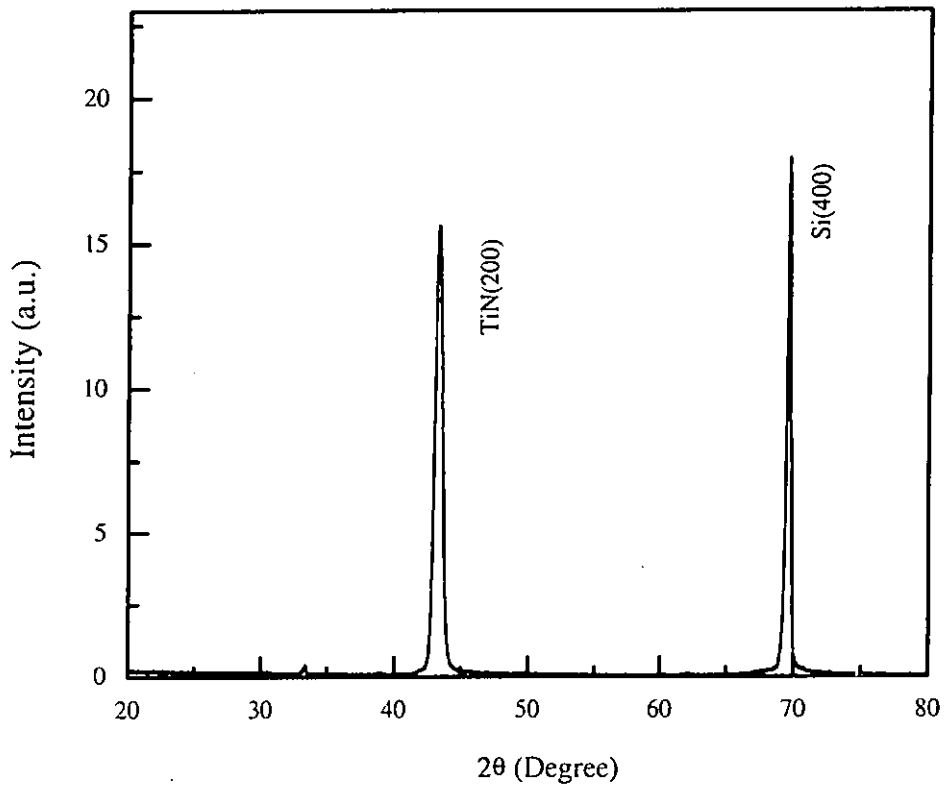

Fig.5.1 X-ray θ-2θ diffraction pattern for the TiN/Si structure. The TiN layer was deposited at 600°C under a pressure of $4x10^{-6}$ Torr.

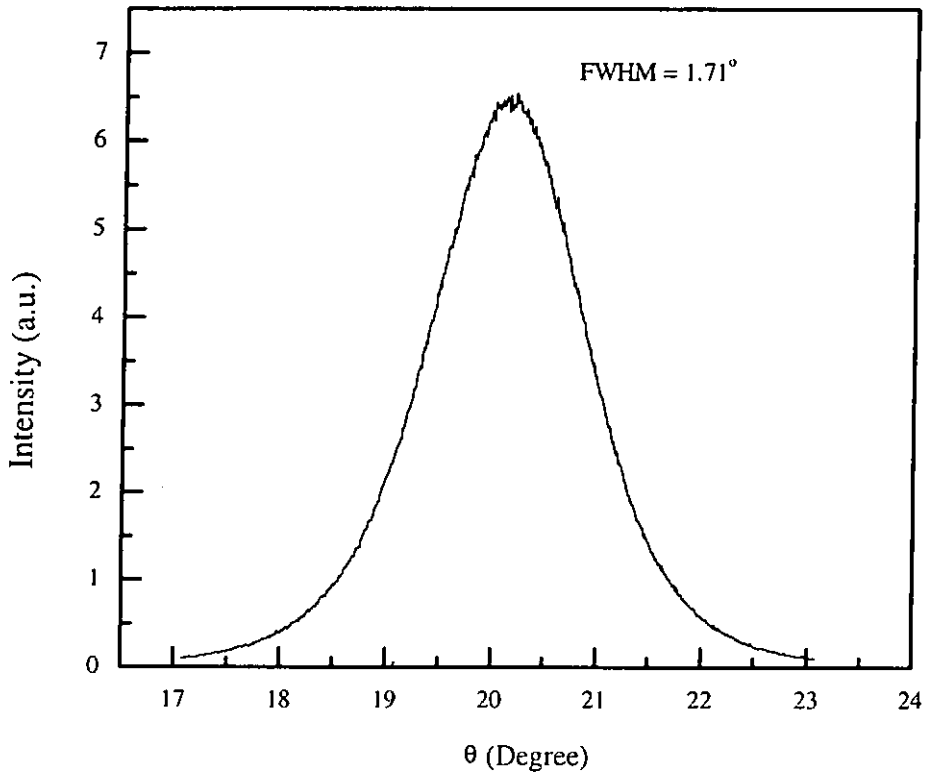

Fig.5.2 Rocking curve of (200)TiN reflection. The TiN layer was deposited at 600°C under a pressure of 4×10^{-6} Torr.

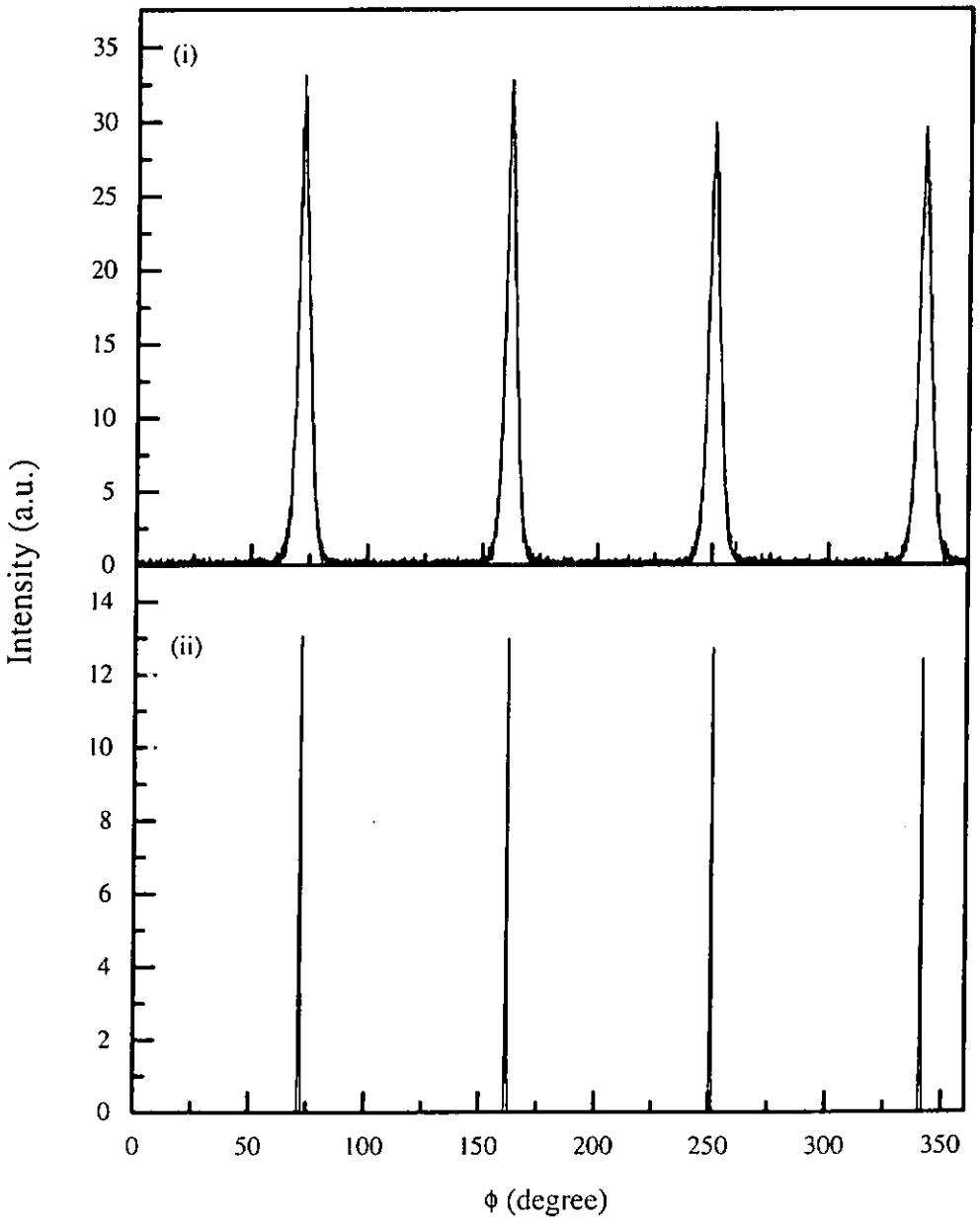

Fig.5.3 360° ϕ-scans diffraction patterns of (i) (220)TiN, and (ii) (220)Si.

peaks for each of the 360° ϕ-scans are observed, indicating the four-fold symmetry of a typical cubic structure. The two sets of reflection peaks occur at the same diffraction angle suggesting a cube-on-cube expitaxial growth of TiN films on Si, i.e. $<100>_{TiN}\|<100>_{Si}$. For the TiN films deposited at a higher temperature, 720°C, similar results are obtained.

5.2.2 Characterization of STO/TiN/Si

5.2.2.1 $SrTiO_3$ (STO) Target Fabrication

The fabrication process of the $SrTiO_3$ (STO) target is very similar to that of SVO target as mentioned in Section 4.2.1. For the ratio between strontium and titanate to be 1, the required mass for $SrCO_3$ and TiO_2 are calculated as follows:

Molar mass of

$SrCO_3$: 147.63

TiO_2 : 79.90

For $SrCO_3$, the required mass is calculated as follows:

147.63 / 99% = 149.121

149.121 / 18 = 8.2845g

Similarly, the required mass of TiO_2 is calculated as follows:

79.90 / 99.99% = 79.908

79.908 / 18 = 4.439g

In the present work, high purity AR grade of titanium dioxide (TiO_2) (grade: 4N) and strontium carbonates ($SrCO_3$) (grade: 2N) were used to fabricate the STO target. After the desired proportion of oxides was weighed, they were well mixed by a

mortar and a pestle for about 1 hour. The powders were then put into an alumina crucible and covered with a lid. The whole assembly was heated to 1000°C at a rate of 10°C/min in a high temperature furnace for calcination. After heated at 1000°C for 10 hours, the sample was cooled down to room temperature slowly. The resulting STO compound (in the form of a block) was then crushed and ground by a mortar and a pestle for about 1 hour. In order to ensure the homogenity and complete calcination of the compound, it was re-calcinated at 1000°C in the furnace for 10 hours. The resulting compound was then re-ground into fine powder. Afterwards the powder was pressed into circular pellets of diameter 22 mm and thickness 5 mm, using a pressure of about 1000 kg/cm^2. The pellets were sintered at 1300°C in the furnace for 10 hours. The structure of the resulting STO target was characterized by an X-ray diffractometer.

Fig.5.4 shows the X-ray θ–2θ diffraction pattern of the STO perovskite oxide target. Sharp and strong reflection peaks are observed. They were identified and were labeled in the figure for reference. Thus the XRD profile suggests that the STO target is well crystallized and is fit for PLD for preparing STO thin films.

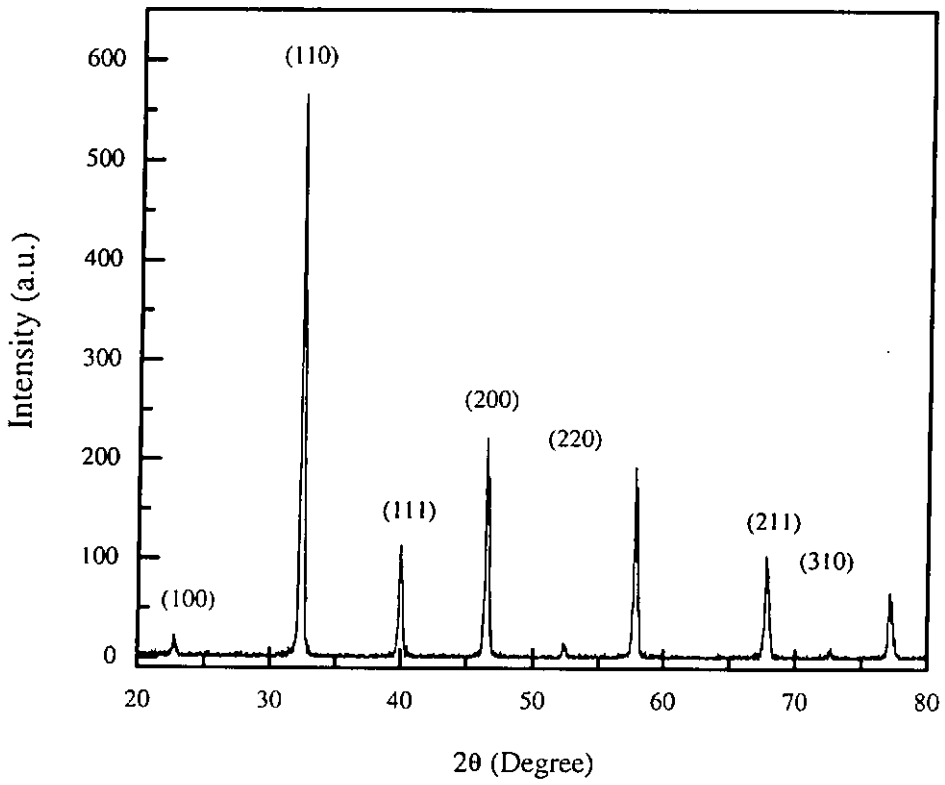

Fig.5.4 XRD pattern of the STO perovskite oxide target.

5.2.2.2 Structural Analysis of STO Thin Films

As discussed in Section 5.1, in order to overcome the problems of lattice mismatch and chemical reaction between YBCO and the Si substrate, different buffer layers have been used. In the present work, STO/TiN buffer layers are used. The reason for introducing the STO buffer layer as well as the TiN buffer layer is because high processing temperature (750°C) and ambient oxygen (300 mTorr) are required during deposition and post-annealing of YBCO films and the TiN buffer layer will probably be oxidized under such circumstances. For this reason, one more buffering layer, STO is introduced before depositing the YBCO films.

STO has a cubic perovskite structure. It has a high dielectric constant ($\varepsilon_r = 300$ at room temperature) which makes it a useful material for DRAMs in semiconductor devices. Its lattice constant of 3.906 Å is lattice match with both of TiN (4.24 Å) and YBCO (a = 3.82 Å, b = 3.89 Å, c = 11.68 Å).

During depositing the STO films, the deposition temperature used was kept at 650°C and a high vacuum condition was needed to avoid undesirable oxidation of the TiN buffer layer. Besides, they were prepared under laser fluence of 3 J/cm^2 with a repetition rate of 10 Hz for 6 minutes. The thickness of the STO films, as measured by the profiler and cross-section SEM imaging was about 150 nm.

Fig.5.5 shows the X-ray θ-2θ diffraction pattern for the STO/TiN/Si heterostructure. The STO and TiN films were deposited at 650°C and 720°C,

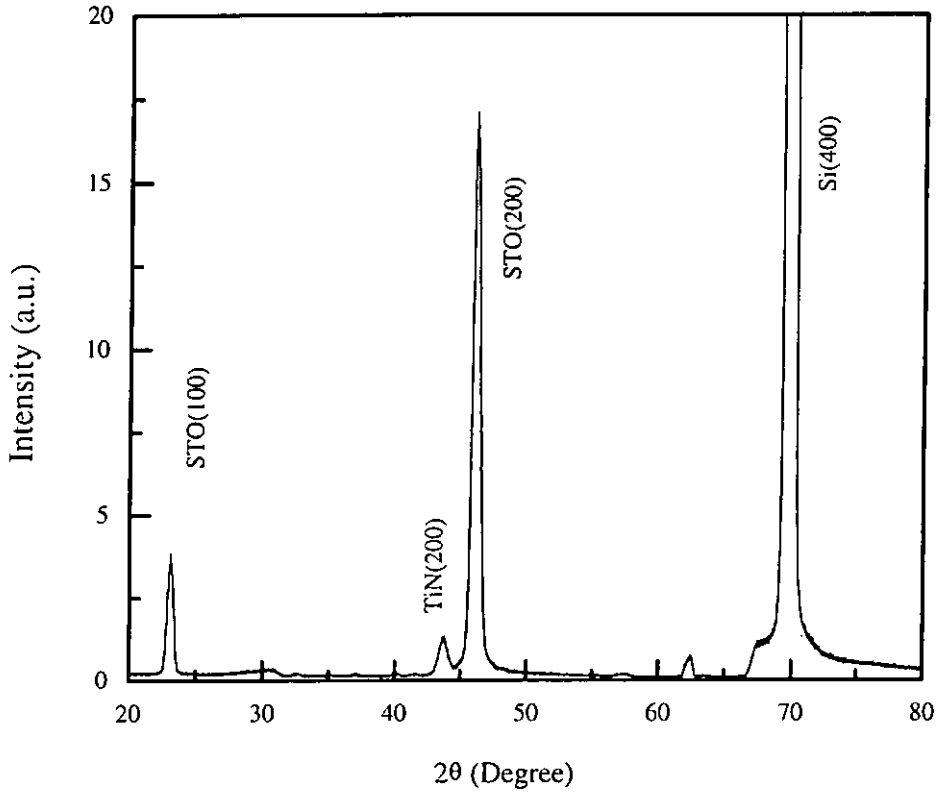

Fig.5.5 X-ray θ-2θ diffraction pattern for the STO/TiN/Si structure. The STO and TiN layers were deposited at 650°C and 720°C, respectively, under a pressure of $4x10^{-6}$ Torr.

respectively, under a pressure of $4x10^{-6}$ Torr. Single phase of TiN and STO films were observed. Fig.5.6 shows the rocking curves of (200)STO and (200)TiN reflections. Their FWHM are 1.52° and 1.67° respectively. Fig.5.7 shows the 360° ϕ-scans of (220)STO, (220)TiN and (220)Si reflection peaks. Again, four sharp peaks for each of the ϕ-scans are observed indicating the four-fold symmetry of a typical cubic structure. The three sets of reflections occur at the same diffraction angle suggesting a cube-on-cube expitaxial growth of STO films on TiN buffered Si substrate. For the STO/TiN/Si heterostructure, lower deposition temperature (600°C) for TiN film was also tried and it showed similar results as that of higher deposition temperature. From these results, we can conclude that high quality of STO films is obtainable on the TiN buffered Si substrate. Consequently, YBCO is possible to be deposited on top of STO/TiN/Si to form YBCO/STO/TiN/Si heteroepitaxial structures.

5.3 Characterization of YBCO/STO/TiN/Si

There are several parameters that influence the quality of YBCO films such as the nature and orientation of the substrate. Besides, the temperature and pressure used during film growth may also play a very important role in obtaining good quality of YBCO films. In this section, the quality of the deposited YBCO thin films as influenced by the temperature and pressure are discussed.

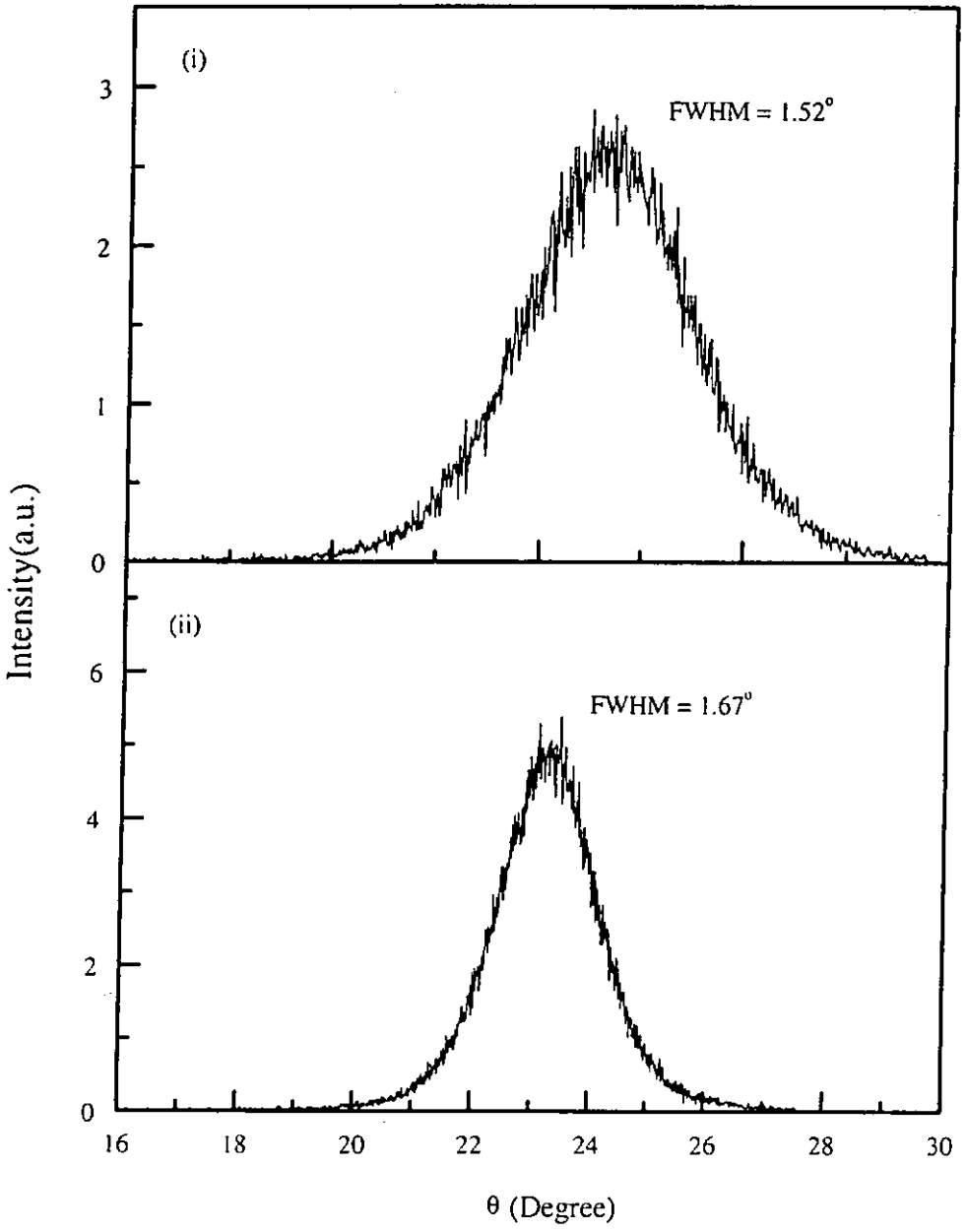

Fig.5.6 Rocking curves of (i) (200)STO and (ii) (200)TiN reflections. The MgO and TiN layers were deposited at 650°C and 720°C, respectively, under a pressure of $4x10^{-6}$ Torr.

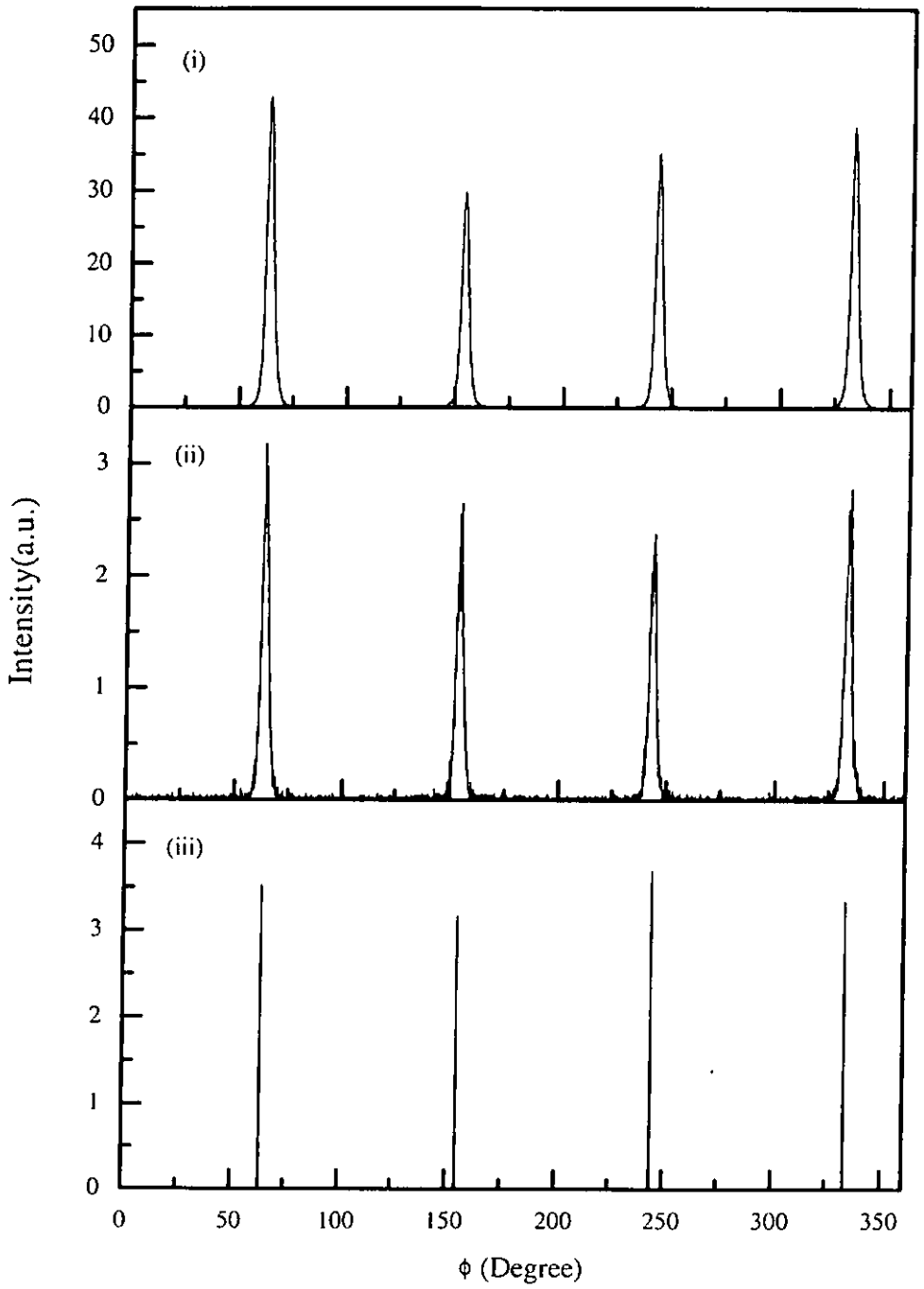

Fig.5.7 360° ϕ-scans diffraction patterns of (i) (220)STO, (ii) (220)TiN, and (iii) (220)Si.

5.3.1 Substrate Temperature Dependence

YBCO films were deposited on the STO/TiN/Si heterostructure under different deposition temperatures ranging from 650°C – 750°C with the ambient oxygen pressure kept at 300 mTorr. The STO/TiN buffer layers, however, were deposited at 650°C under high vacuum. Fig.5.8 shows the X-ray θ-2θ diffraction patterns for the YBCO films deposited on the STO/TiN/Si heterostructure with different substrate temperatures of 650°C, 700°C and 750°C. It is seen that highly oriented YBCO films with strong (00ℓ) reflections are prepared. Besides, the (200)TiN reflections were also recorded when YBCO films were deposited at deposition temperatures of 650°C and 700°C. And their corresponding FWHM of the (200)TiN reflections are 1.91° and 2.31°. It is clearly that when the YBCO is deposited at a higher deposition temperature, the crystallinity of YBCO films gets better. It is reflected from the decreasing value of the FWHM of the YBCO reflection peaks. For example, the FWHM of the (005)YBCO reflections are 1.90°, 1.83° and 1.58° for deposition temperature of 650, 700 and 750°C respectively. In contrast, the FWHM of (200)TiN reflection peaks gets wider and even disappears as the growth temperature of YBCO increases. This phenomenon may attribute to the fact that under elevated temperature with high ambient oxygen pressure, the oxygen may diffuse through the STO capping layer. As a result, TiN is oxidized and the crystallinity of TiN is destroyed. The oxidation of TiN may cause damaging structural defects and can have detrimental effect on the YBCO films and the overall heterostructures. Discussion on these and the remedial solution will be discussed in later chapters.

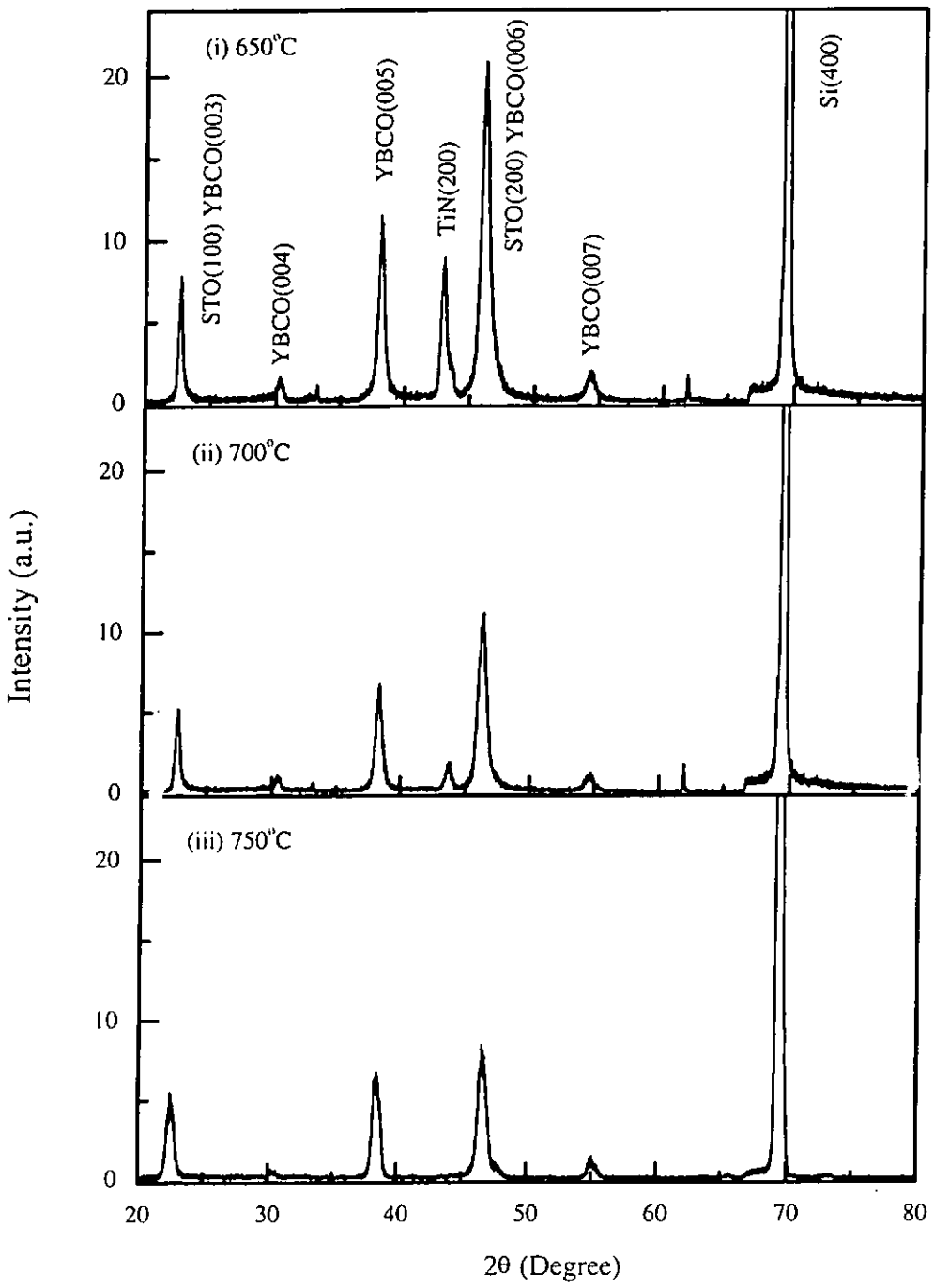

Fig.5.8 X-ray θ-2θ diffraction patterns for YBCO films deposited on the STO/TiN/Si heterostructure. The YBCO layer was deposited under an ambient oxygen pressure of 300 mTorr at different deposition temperatures of (i) 650°C, (ii) 700°C, and (iii) 750°C. Both of the TiN and STO layers were deposited under high vacuum ($4x10^{-6}$ Torr) with deposition temperature of 650°C.

5.3.2 Ambient Oxygen Dependence

In view of the fact that the TiN buffer layer was oxidized when deposited YBCO film at high deposition temperature with high ambient oxygen, so, YBCO film deposited at a lower deposition temperature with high vacuum was tried to grow on the TiN/Si structure first. Then YBCO film deposited at high deposition temperature with high ambient oxygen was carried out. Here, YBCO itself acted as the buffer layer. Fig. 5.9 shows the X-ray θ-2θ diffraction pattern for the YBCO/YBCO/TiN/Si heterostructure. The top-YBCO layer was grown at 750°C under an ambient oxygen pressure of 300 mTorr. The YBCO-buffered and TiN-buffered layers were grown at 650°C and 600°C, respectively, under a pressure of $4x10^{-6}$ Torr. It is clear that only weak signal of (00ℓ)YBCO reflections are obtained. It may be due to the oxygen deficiency of the YBCO films.

Fig.5.10, on the other hand, shows the X-ray θ-2θ diffraction pattern for the YBCO/STO/TiN/Si heterostructure. The deposition conditions for the corresponding layers were kept the same. Clearly, sharp reflection peaks of (00ℓ)YBCO are obtained. And the X-ray ω-scan rocking curves on the (005) reflection of the YBCO shows that the FWHM is 1.7° indicating that the film is of good (00ℓ) orientation. Fig.5.11 shows the X-ray 360° φ-scans on the (220)YBCO, (220)STO and (220)Si diffraction. Apart from the four YBCO peaks, other set of four peaks is observed. They are also separated by 90° but shifted by 45° relative to the YBCO peaks. Judging from their sharpness, they are most likely Si reflection. Their identities, however, have not been determined.

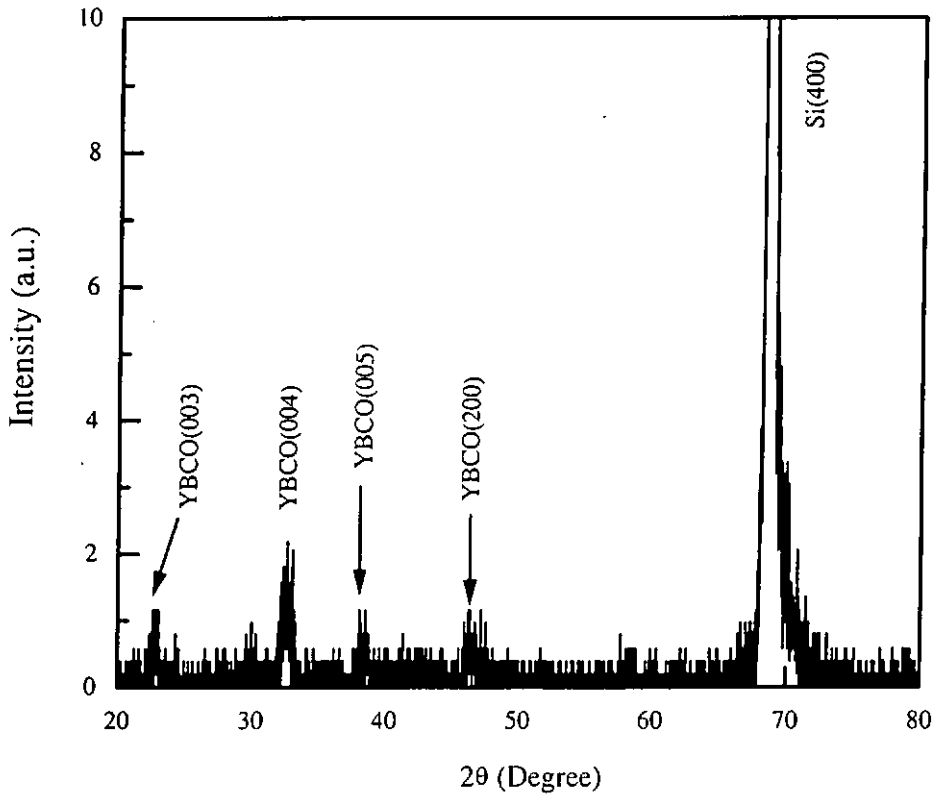

Fig.5.9 X-ray θ-2θ diffraction pattern for the YBCO/YBCO/TiN/Si heterostructure, with the top YBCO layer grown at 750°C under an ambient oxygen pressure of 300 mTorr. The buffered YBCO and TiN layers were grown at 650°C and 600°C, respectively, under high vacuum. After the deposition, the films were annealed for 30 minutes at 500°C under 1 atm oxygen pressure.

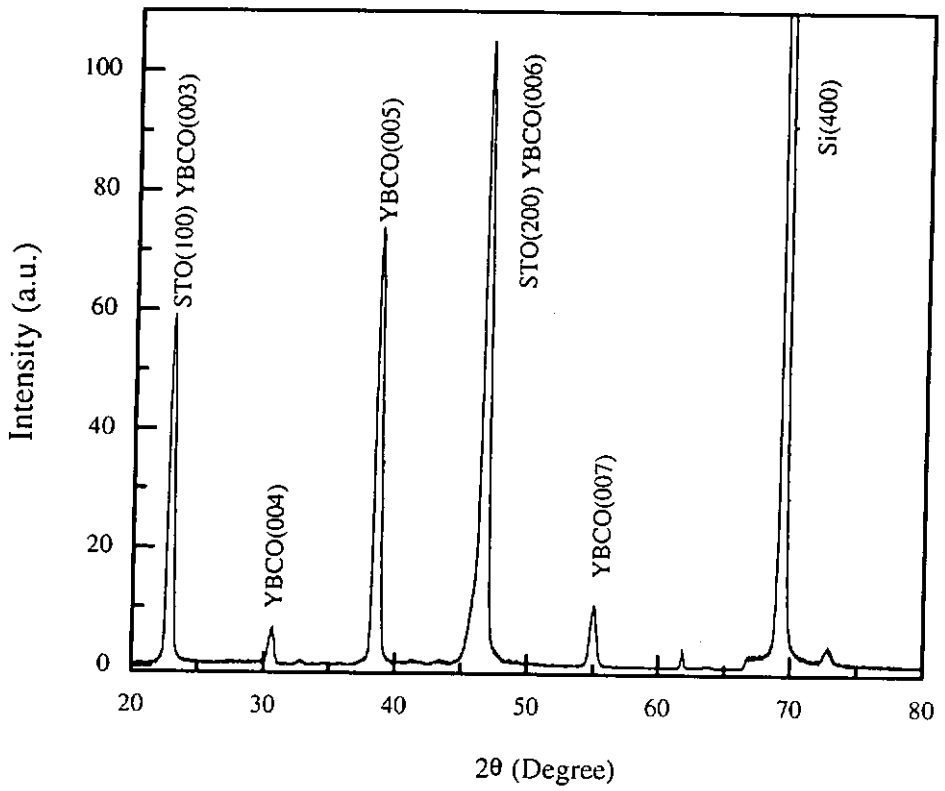

Fig.5.10 X-ray θ-2θ diffraction pattern for the YBCO/STO/TiN/Si heterostructure with the YBCO layer grown at 750°C under 300 mTorr ambient oxygen pressure and both of the STO and TiN layers were under high vacuum with deposition temperature of 650°C and 600°C, respectively.

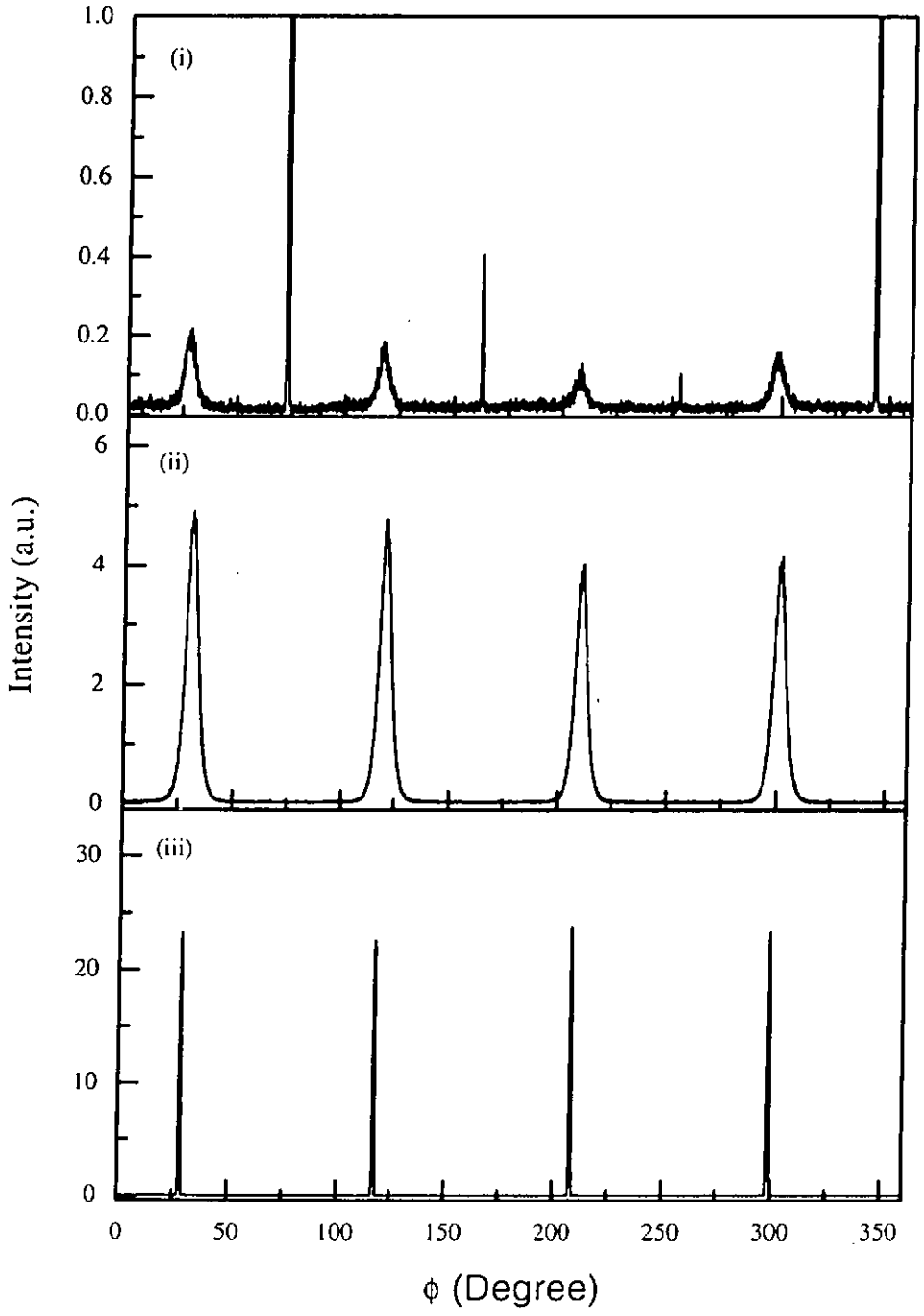

Fig.5.11 X-ray 360° ϕ-scans on the (i) (220)YBCO, (ii) (220)STO and (iii) (220)Si diffraction.

5.3.3 Electrical Property of the YBCO Thin Films

Fig.5.12a and Fig.5.12b show the resistivity against temperature of the YBCO films deposited on the STO/TiN/Si heterostructure. The YBCO layer was grown at 750°C under ambient oxygen pressure of (a) 400 mTorr and (b) 300 mTorr. The STO and TiN buffer layers were deposited at 650°C and 600°C, respectively, under a pressure of $4x10^{-6}$ Torr. The as-grown films were then post-annealed at 500°C in oxygen atmosphere for 30 minutes. From the resistivity against temperature profiles, it is seen that the films show metallic behavior and have a zero resistivity temperature of 88 K. It is comparable with the results obtained by other research group of which the T_c obtained for the YBCO films with YSZ buffer layers on Si is 87 K [Hwang et al., 1995].

Fig.5.13 shows the resistivity against temperature of the YBCO film deposited directly on the $LaAlO_3$ (LAO) single crystal substrate. The YBCO film shows metallic behavior and has a zero resistivity temperature of 90 K. Obviously, we can see that the T_c obtained for the YBCO/STO/TiN/Si heterostructure is quite comparable to the one directly grown on LAO substrate. Yet, the T_c can still be better. In Section 5.3.5, the surface morphology of the YBCO/STO/TiN/Si heterostructure is shown. Microcracks are seen running along the film surface. These cracks may actually severely degrade the electrical qualities of the superconductor film.

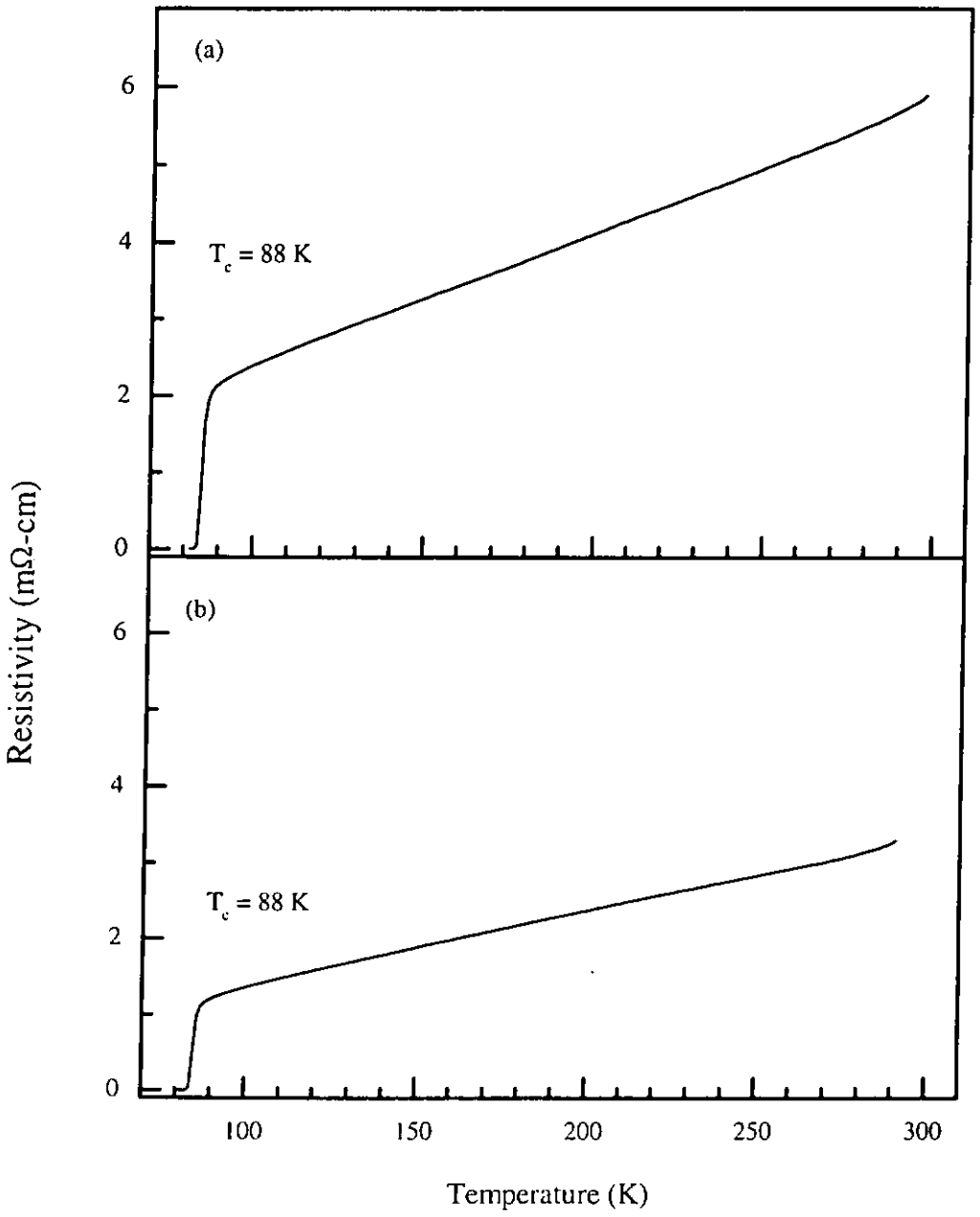

Fig.5.12 Resistivity against temperature of YBCO films deposited on the STO/TiN/Si heterostructure, with the YBCO layer grown at 750°C under an ambient oxygen pressure of (a) 400 mTorr, and (b) 300 mTorr. The TiN and STO films were deposited at 650°C and 600°C, respectively, under high vacuum.

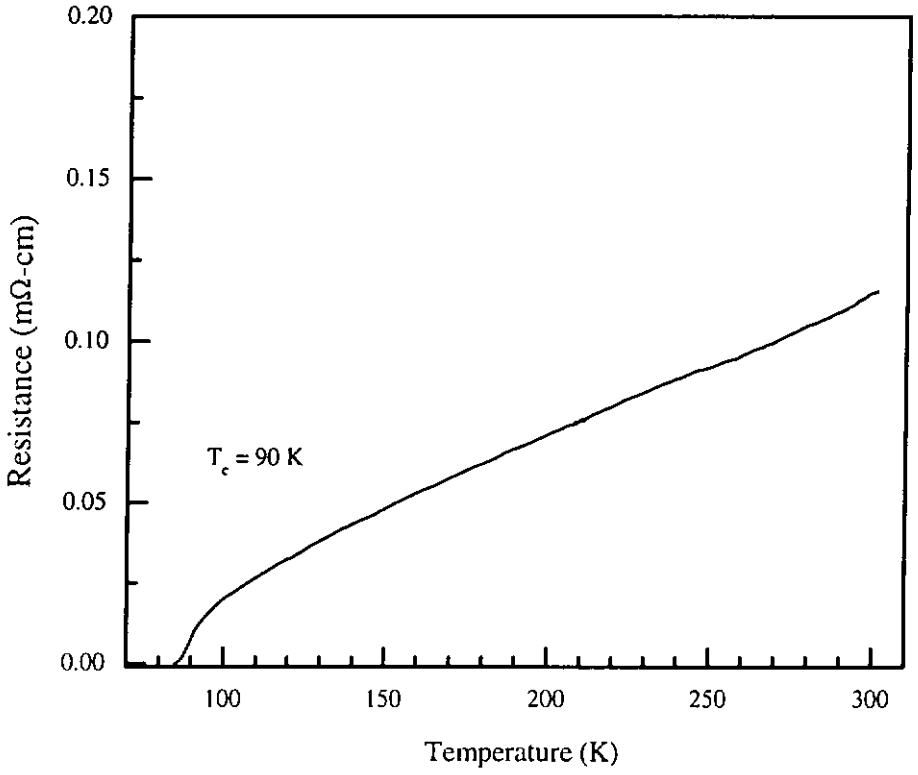

Fig.5.13 Resistivity against temperature of YBCO film deposited on LAO(100) with the YBCO layer grown at 750°C under an ambient oxygen pressure of 400 mTorr and post-annealed at 500°C under 1 atm pressure for 30 minutes.

5.3.4 Cross-section of the YBCO Thin Films

Fig.5.14a and Fig.5.14b show the scanning electron micrographs of the cross-section of the YBCO/STO/TiN/Si heterostructure. In Fig.5.14a, the YBCO layer was grown at 750°C under 300 mTorr whereas both of the STO and TiN layers were grown at 650°C and 720°C, respectively, under a pressure of $4x10^{-6}$ Torr. Actually, the deposition conditions for the YBCO/STO/TiN/Si heterostrcuture in Fig.5.14b was the same as that in Fig.5.14a except that the deposition temperature for the TiN film was at 600°C. From these two different figures, we can see that there are three different layers. The thickness for the corresponding layers in both cases was about the same and was about 550 nm, 150 nm and 200 nm for the YBCO, STO and TiN layers respectively. Besides, we can see the film has several types of defects: grain boundaries, thermally induced cracks and irregular shaped outgrowths. Some grains appear to grow from the interface, a feature similar to the reported case in which the YSZ buffer layer is being used [Hwang et al., 1995]. Hwang et al suggests that the grains outgrow from the interface between YSZ and YBCO. As the film thickens, the grain develops into a cone shape. From the electron probe microanalysis (EPMA) study, they find that the outgrowths have the same composition as the background film. Besides, they are believed to be the same 123 phase as the rest of the film. They nucleate and grow from the YSZ surface with a relatively larger growing rate than the background film like the a-axis growth. Applying the same conception, the outgrowth for the YBCO/STO/TiN/Si heterostructure may come from the interface between STO and YBCO. Similarly, the grain develops into a cone shape.

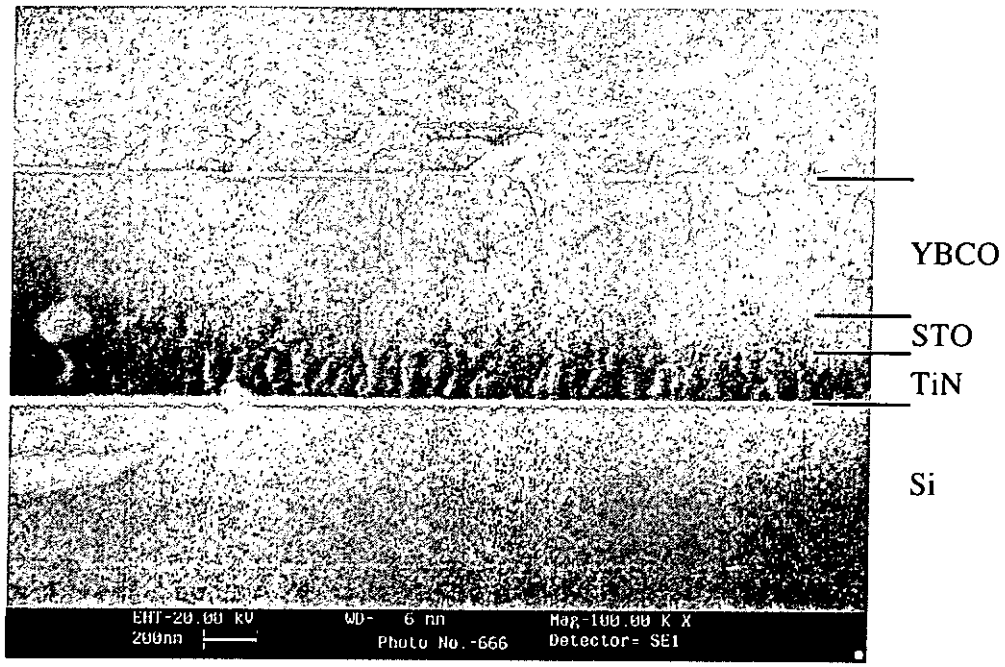

(a)

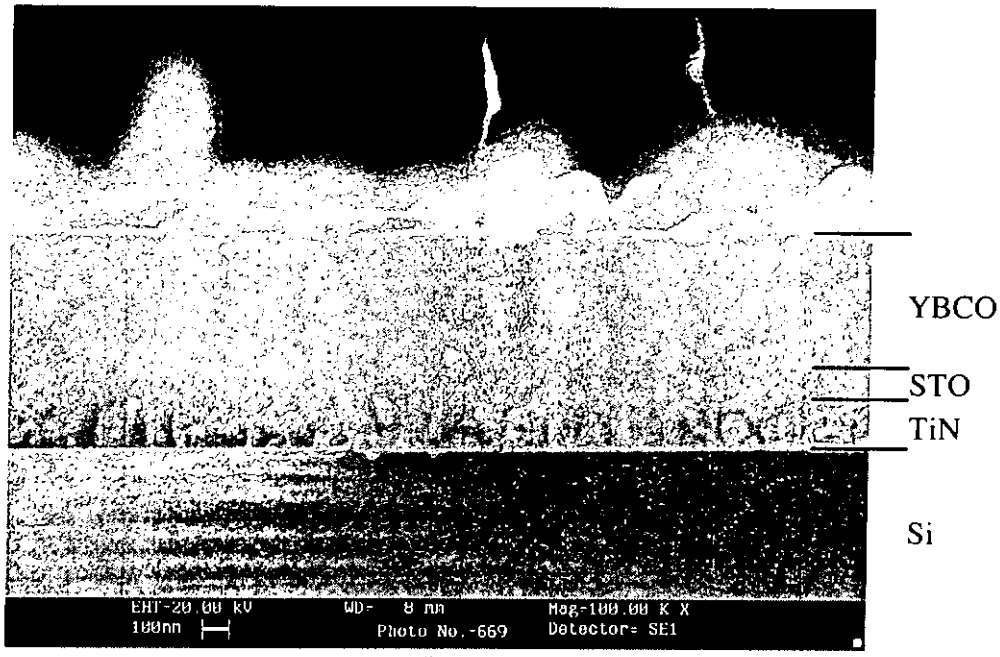

(b)

Fig.5.14 The cross-section of the YBCO/STO/TiN/Si heterostructure, with the TiN layer deposited at (a) 720°C and (b) 600°C, under high vacuum. The YBCO layer was deposited at 750°C under an ambient oxygen pressure of 300 mTorr whereas the STO layer was deposited at 650°C under high vacuum.

5.3.5 Surface Morphology of YBCO Thin Films

5.3.5.1 Substrate Temperature Effect

Fig.5.15, Fig.5.16, and Fig.5.17 show the surface morphologies of YBCO films deposited on the STO/TiN/Si heterostructure. The YBCO layer was deposited at different substrate temperatures of Fig.5.15 (650°C), Fig.5.16 (700°C) and Fig.5.17 (750°C) under an ambient oxygen pressure of 300 mTorr. In Fig.5.15 and Fig.5.16, both of the STO and TiN buffer layers were deposited at 650°C with a pressure of 4 x 10^{-6} Torr. There is big difference in the orientation of the YBCO films. Chan et al. [1989] pointed out that for their YBCO films, the a, b-oriented grains appeared as cross bars and the c-oriented grains appeared as disks. In accordance with what he defined, the orientation of the YBCO grains in Fig.5.15 should be a-c mixed with the YBCO parallel to [100] directions of STO whereas that in Fig.5.16 should be c-oriented.

In Fig.5.17, the deposition conditions for both of the STO and TiN buffer layers were also grown with a base pressure of ~10^{-6} Torr. But the deposition temperatures for them are at 650°C and 720°C respectively. From the surface morphology of the YBCO film shown, we can see that the film is c-oriented. When compare this one with the one shown in Fig.5.16, we can see that the grains in Fig.5.17 are more disks like, it actually implies that the film is much more c-oriented than that in Fig.5.16. In fact, it is consistent with what other has reported that higher deposition temperature favors c-oriented [Lee et al., 1991].

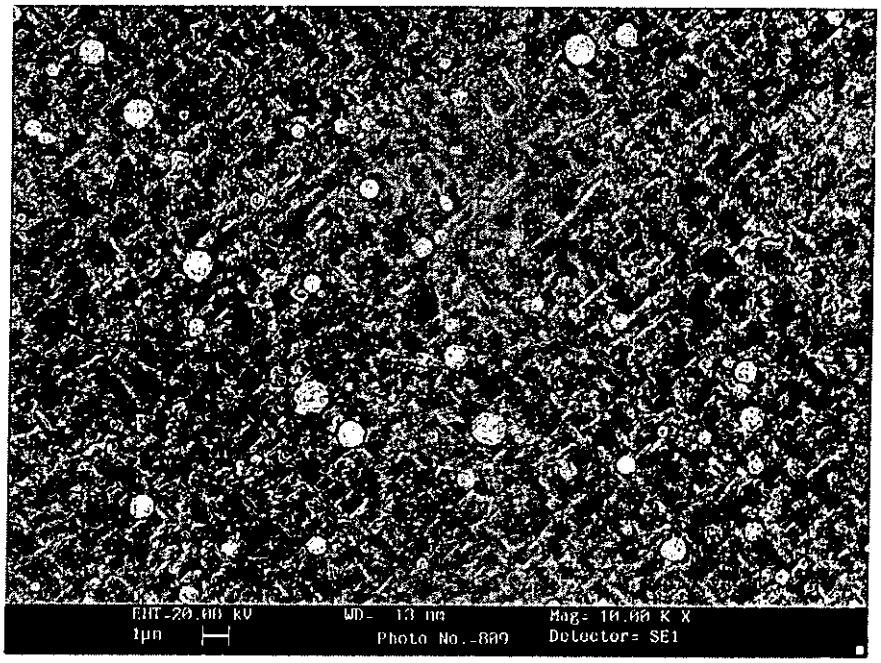

(i)

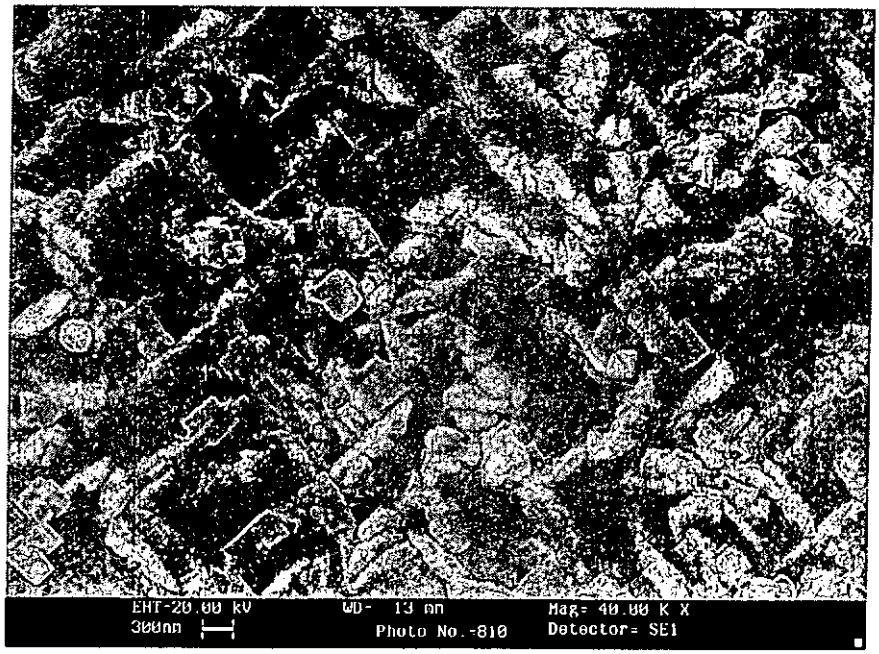

(ii)

Fig.5.15 Surface morphology of the YBCO film deposited on the STO/TiN/Si heterostructure: (i) magnification = 1×10^4, (ii) magnification = 4×10^4. The YBCO layer was deposited at 650°C under an ambient oxygen pressure of 300 mTorr, whereas the STO and TiN buffer layers were deposited at 650°C under a pressure of 10^{-6} Torr.

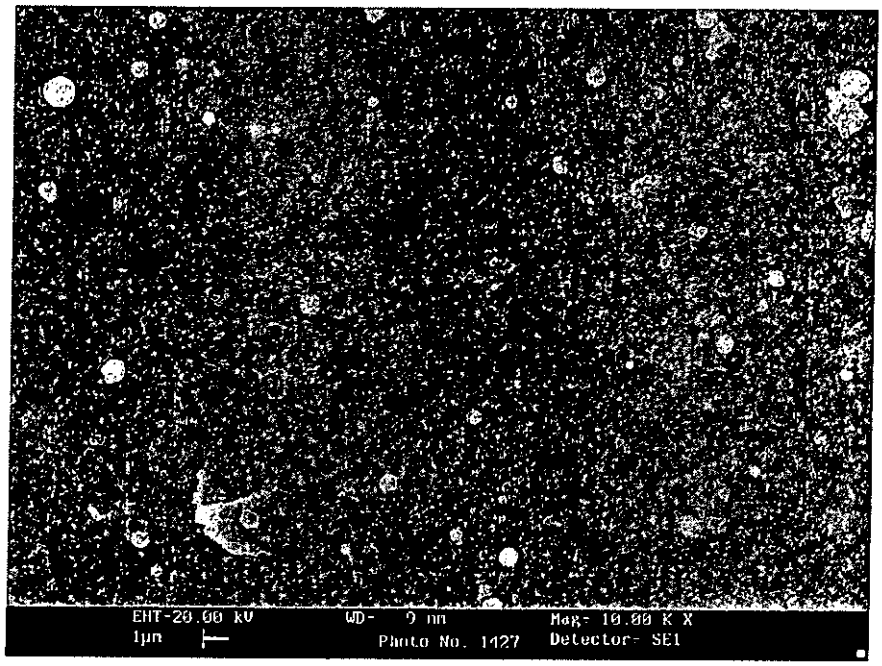

(i)

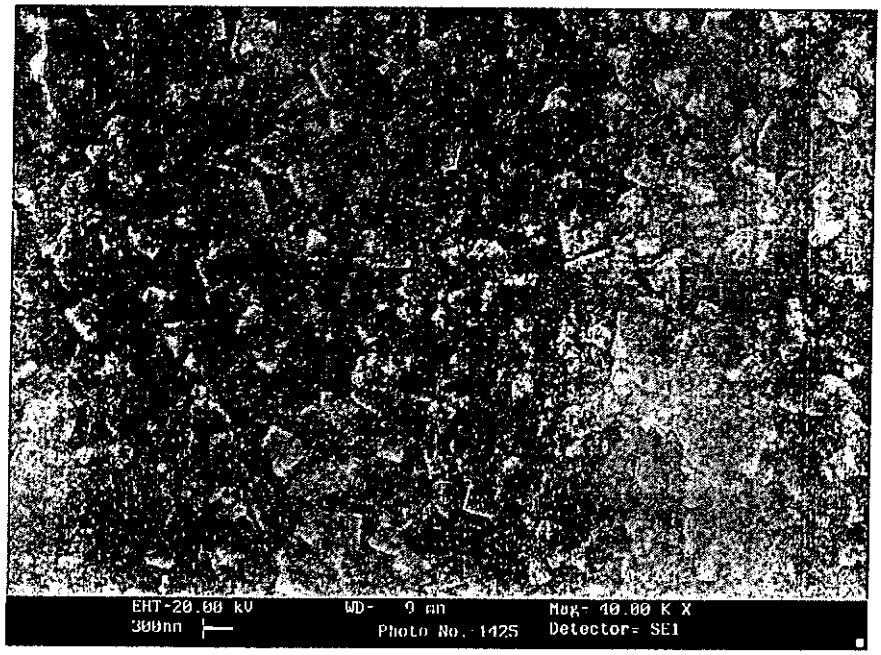

(ii)

Fig.5.16 Surface morphology of the YBCO film deposited on the STO/TiN/Si heterostructure: (i) magnification = 1×10^4, (ii) magnification = 4×10^4. The YBCO layer was deposited at 700°C under an ambient oxygen pressure of 300 mTorr, whereas the STO and TiN buffer layers were deposited at 650°C under a pressure of 10^{-6} Torr.

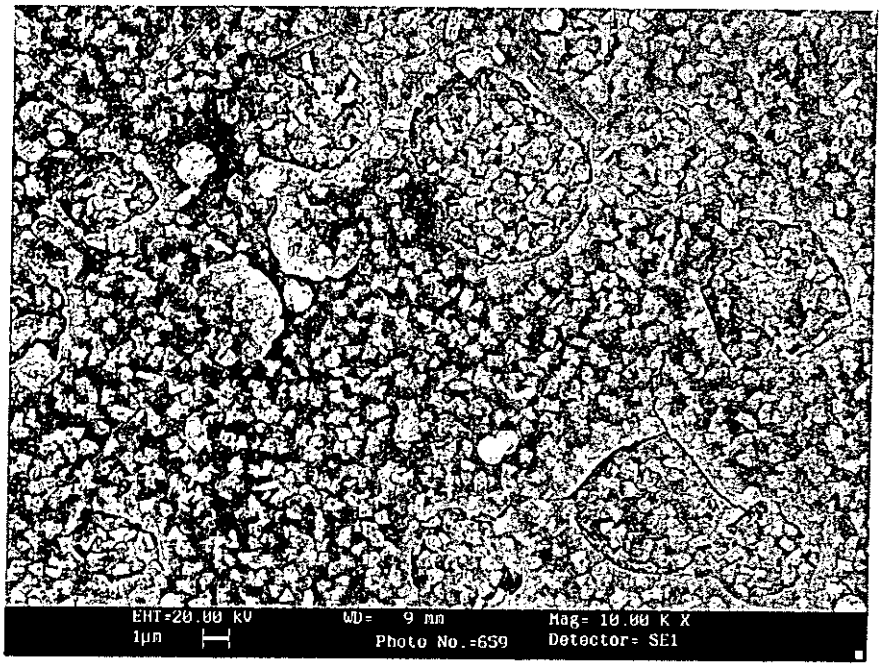

(i)

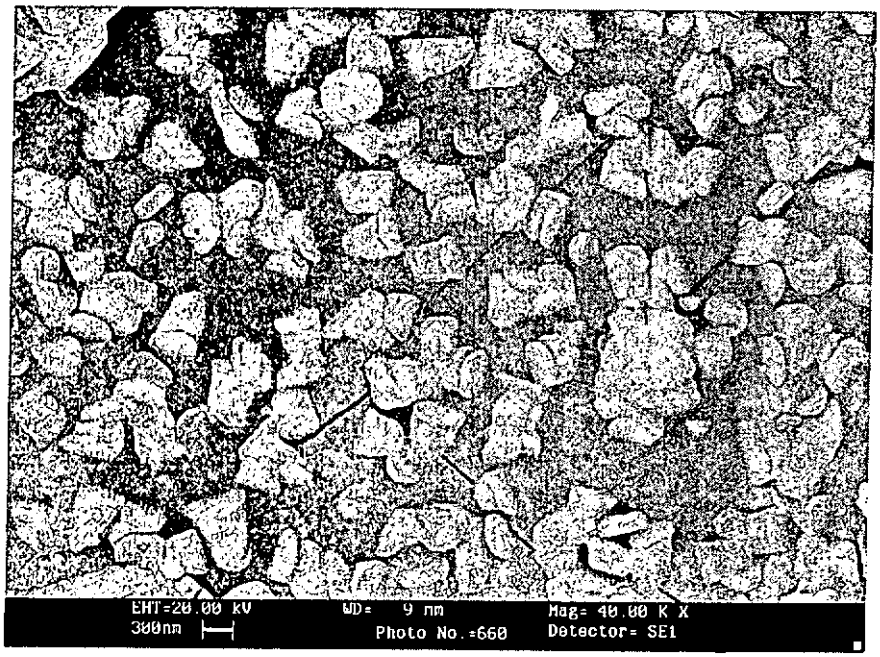

(ii)

Fig.5.17 Surface morphology of YBCO films deposited on the STO/TiN/Si heterostructure: (i) magnification = 1×10^{4}, (ii) magnification = 4×10^{4}. The YBCO layer was deposited at 750°C under an ambient oxygen pressure of 300 mTorr, whereas the STO and TiN buffer layers were deposited at 650°C and 720°C, respectively, under a pressure of 10^{-6} Torr.

5.3.5.2 Ambient Oxygen Effect

Fig.5.18a and Fig.5.18b show the scanning electron microscopy (SEM) of the YBCO/STO/TiN/Si heterostructure. The deposition conditions are the same as described in Section 5.3.3. The ambient oxygen pressure of YBCO film in Fig.5.18a is 400 mTorr and that in Fig.5.18b is 300 mTorr. Obviously, we can see that some spherical particulates, which is a common PLD feature without shadow masks and microcracks formed on the surface. The microcracks may be due to the fact that there is large difference in thermal expansion coefficients (α_{YBCO} = 12.6 x 10^{-6}/K and α_{STO} = 8 x 10^{-6}/K) [Qiao et. al., 1994] between YBCO and STO. As the difference in thermal expansion coefficient will cause the film under tensile stress when cool the film down from the deposition temperature. In order to relax the strain, microcracks are then formed. Comparatively, we can see that microcracks in Fig.5.18a is more severe than that in Fig.5.18b. This phenomenon may be probably due to the fact that TiN is more severely damaged under higher ambient oxygen. Consequently, it then affects the films growing on it.

In short, from the above discussion, it seems that the STO is not the best buffer layer for depositing YBCO on Si. Although, the T_c obtained for the YBCO/STO/TiN/Si heterostructure was 88 K which was comparable to that grown on single crystal LAO substrates of which a T_c of 90 K was obtained. However, from the scanning electron microscopy, it showed that the surface morphologies of the YBCO films on the STO/TiN/Si heterostructure had microcracks as well as the presence of particulates. The microcracks may be due to the large difference in

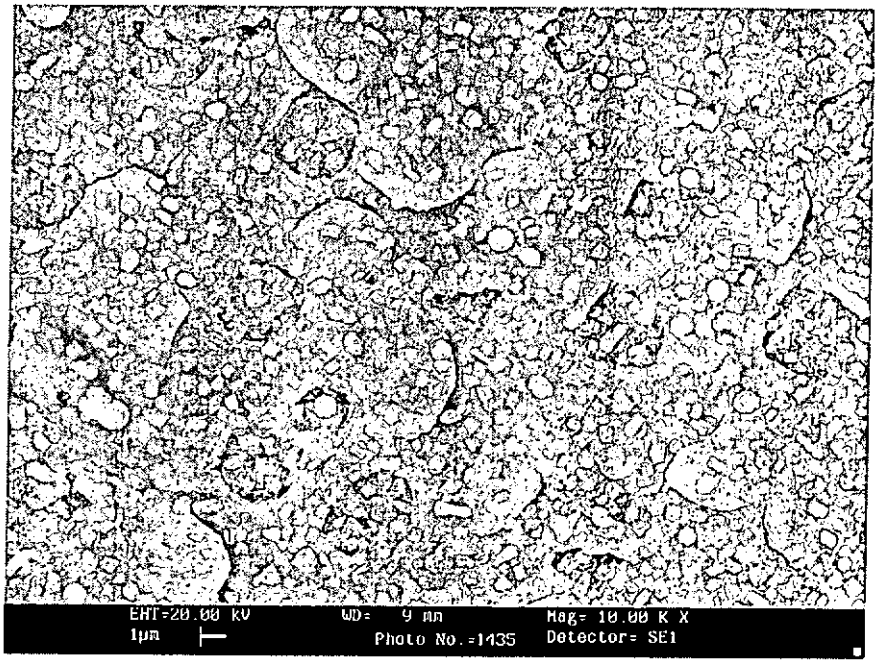

(a)

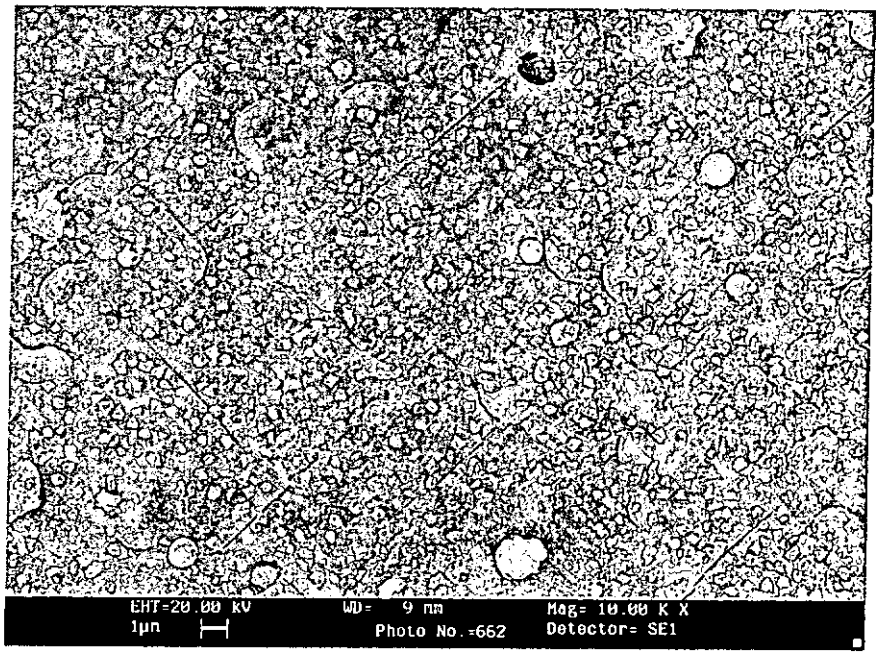

(b)

Fig.5.18 Surface morphology of YBCO films deposited on the STO/TiN/Si heterostructure, with the YBCO layer grown at 750°C under an ambient oxygen pressure of (a) 400 mTorr and (b) 300 mTorr. The STO and TiN buffer layers were grown at 650°C and 600°C, respectively, under a pressure of ~10^{-6} Torr.

thermal expansion coefficients between YBCO and Si. Besides, the oxidation of TiN during the YBCO growth also had detrimental effect on the YBCO films and the overall heterostructures. In the next chapter, we will discuss using the MgO/TiN as the buffer for depositing YBCO on Si.

Chapter 6

Fabrication and Characterization of $YBa_2Cu_3O_{7-x}$ (YBCO) Films on Si Substrates Using MgO/TiN Buffer Layers

6.1 Introduction

In Chapter 5, the fabrication and characterization of YBCO films grown on Si substrates using STO/TiN buffer layers are discussed. It is found that these buffer layers for YBCO films integrating on Si produce detrimental microcracks. In order to circumvent this undesirable feature and to produce a better film quality, magnesium oxide (MgO) is being studied as a buffer layer instead of STO. The lattice constant of MgO is 4.21 Å which has a small lattice mismatch with TiN. It is expected that a good quality of MgO film can be grown on TiN. Our experimental results did show that the MgO could be epitaxially grown on TiN. In fact, MgO is an important material and a key substrate for a variety of perovskites such as superconducting YBCO and ferroelectric lead zirconate titanate. It is a highly ionic insulating solid with a NaCl structure. Besides, it has a small dielectric constant and low loss tangent which makes it ideal for high frequency multilayer circuits.

In this chapter, the structural and electrical properties of the YBCO/MgO/TiN/Si heterostructure are presented. Its merit over the YBCO/STO/TiN/Si heterostructure is also discussed.

6.1.1 Characterization of MgO/TiN/Si

All MgO films in this study were prepared at 650°C under a base pressure of $4x10^{-6}$ Torr. The laser fluence, repetition rate and deposition time used was 3.5 J/cm^2, 10 Hz and 20 minutes respectively. The TiN films were deposited in the same conditions as described in Section 5.2.1. The thickness of the MgO films as measured by the profiler and cross-section SEM imaging was about 120 nm. Fig.6.1 shows the X-ray θ-2θ diffraction pattern for the MgO film deposited on the TiN buffered layer, which was deposited at 600°C under a pressure of $4x10^{-6}$ Torr. Sharp peaks for both of the (200)TiN and (200)MgO reflections were obtained. Since the lattice constants of MgO (4.21 Å) and TiN (4.22 Å) are so close, their peaks cannot be resolved. The FWHM of the combined (200)MgO & (200)TiN reflections is about 1.56° as shown in Fig.6.2. This value suggests that the crystal of the film is highly oriented. In order to determine whether the MgO film was epitaxially grown on the TiN buffered Si substrates, 360° ϕ-scans of (220)MgO, (220)TiN and (220)Si reflections were carried out. Fig.6.3 shows the ϕ-scans of (220)MgO, (220)TiN and (220)Si reflection peaks. Four characteristic peaks of a cubic structure are observed. The positions of the four peaks are in good match. This suggests that a cube-on-cube expitaxial growth of MgO films on TiN buffered Si substrate.

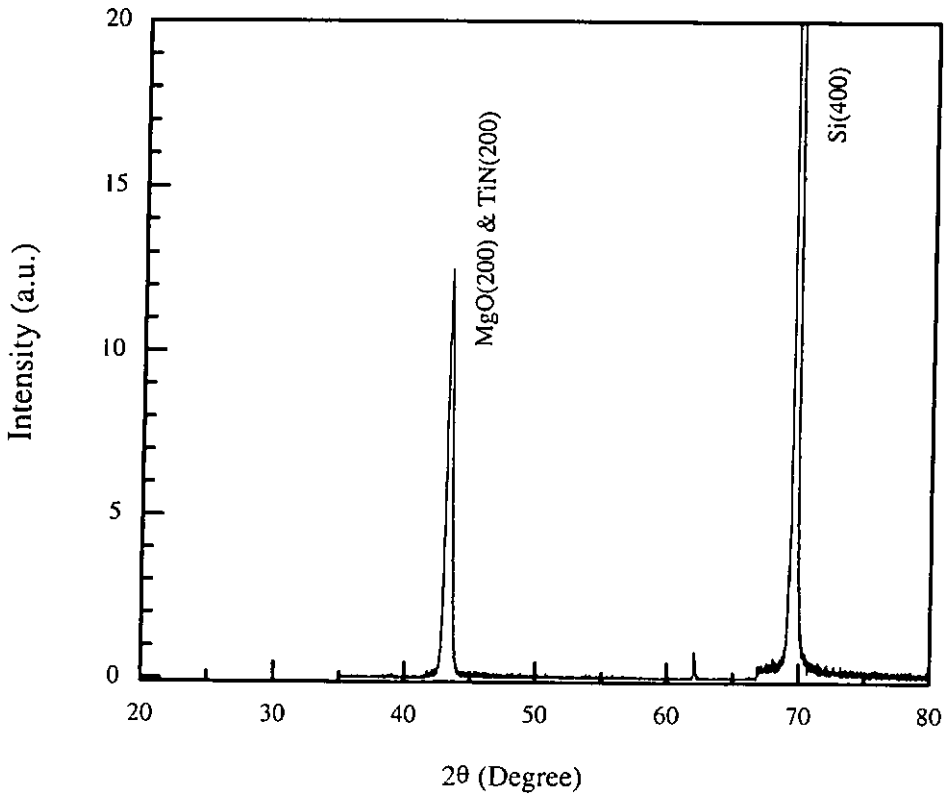

Fig.6.1 X-ray θ-2θ diffraction pattern for the MgO/TiN/Si structure. The MgO and TiN layers were deposited at 650°C and 600°C, respectively, under a pressure of 4×10^{-6} Torr.

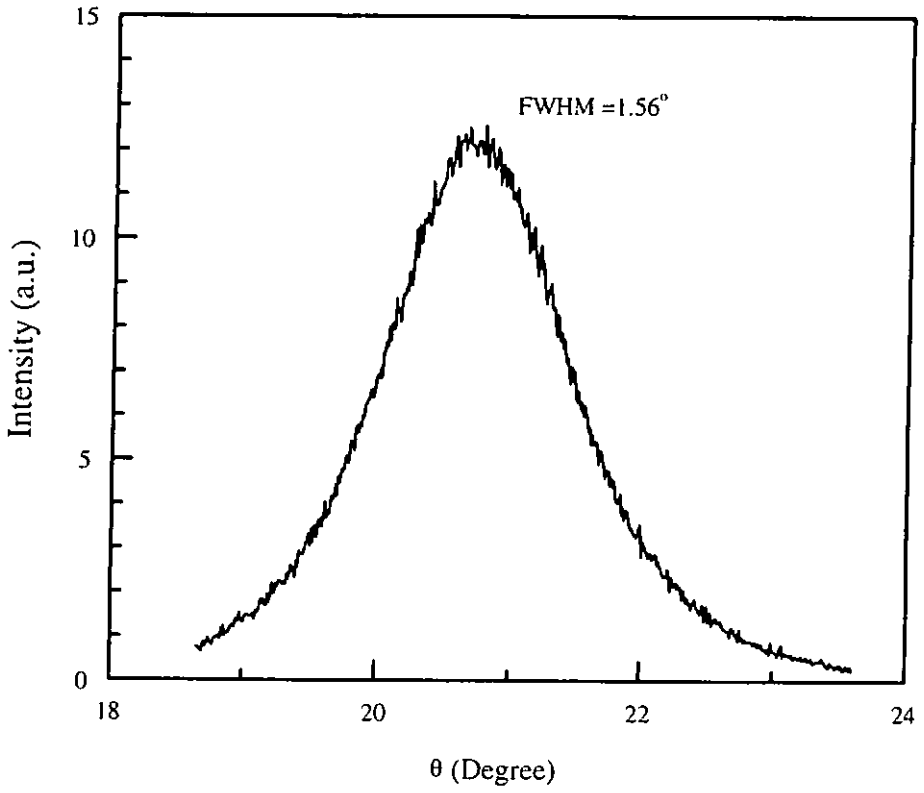

Fig.6.2 Rocking curves of (200)TiN and (200)MgO reflections of the MgO/TiN/Si heterostructure. The MgO and TiN layers were deposited at 650°C and 600°C, respectively, under a pressure of $4x10^{-6}$ Torr.

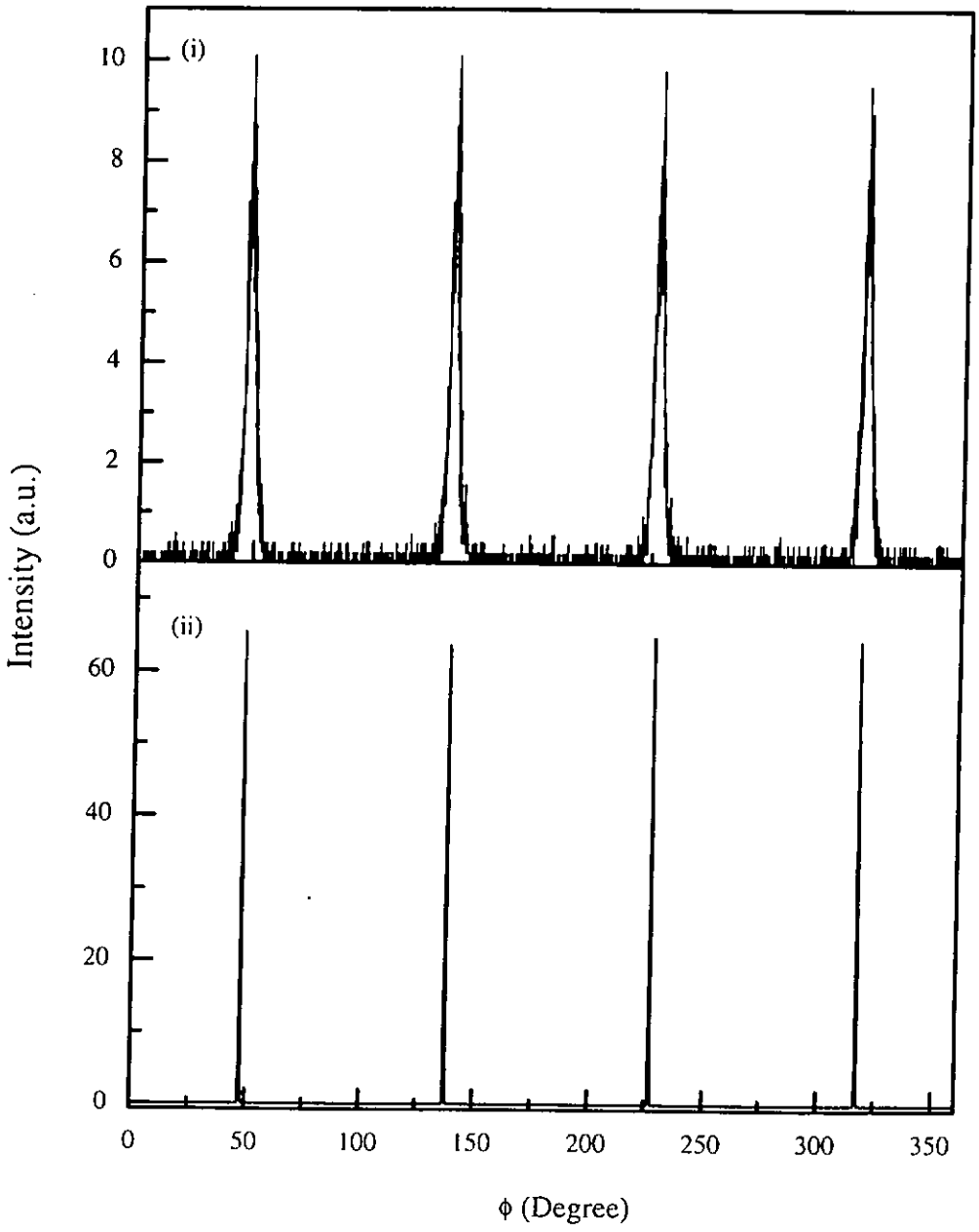

Fig.6.3 360° ϕ-scans diffraction patterns of (i) (220)MgO & (220)TiN, and (ii) (220)Si.

6.2 Characterization of YBCO/MgO/TiN/Si and YBCO/STO/TiN/Si

In Section 6.1.1, MgO has been shown to grow epitaxially on TiN buffered Si substrate. In this section, the structural characterization of YBCO films grown on the MgO/TiN/Si heterostructure is presented. Its superior structural qualities to those using STO as a buffer layer, i.e. YBCO/STO/TiN/Si is also discussed.

6.2.1 Structural Characterization of YBCO/MgO/TiN/Si and YBCO/STO/TiN/Si

Fig.6.4 shows the X-ray θ-2θ diffraction pattern for the YBCO film deposited on the MgO/TiN/Si heterostruture. The YBCO layer was deposited at 750°C under an ambient oxygen pressure of 300 mTorr for 20 minutes. The MgO and TiN were deposited at 650°C and 600°C, respectively, under a pressure of $4x10^{-6}$ Torr. It is seen that highly oriented YBCO films with strong (00ℓ) reflections are prepared. In addition, (200)TiN, (200)MgO and (200)YBCO are also recorded. The reasons why (200)TiN and (200)MgO peaks can be resolved sometimes and the occurrence of the (200)YBCO peaks have not been determined yet. In Section 7.2.1, we will again show that the (200)TiN and (200)MgO and (200)YBCO will appear together sometimes. Nonetheless, the FWHM of the (005)YBCO, (200)MgO and (200)TiN reflections were 1.37°, 1.26° and 1.82° respectively as shown in Fig.6.5. These values actually suggest that the crystal of the film is highly oriented.

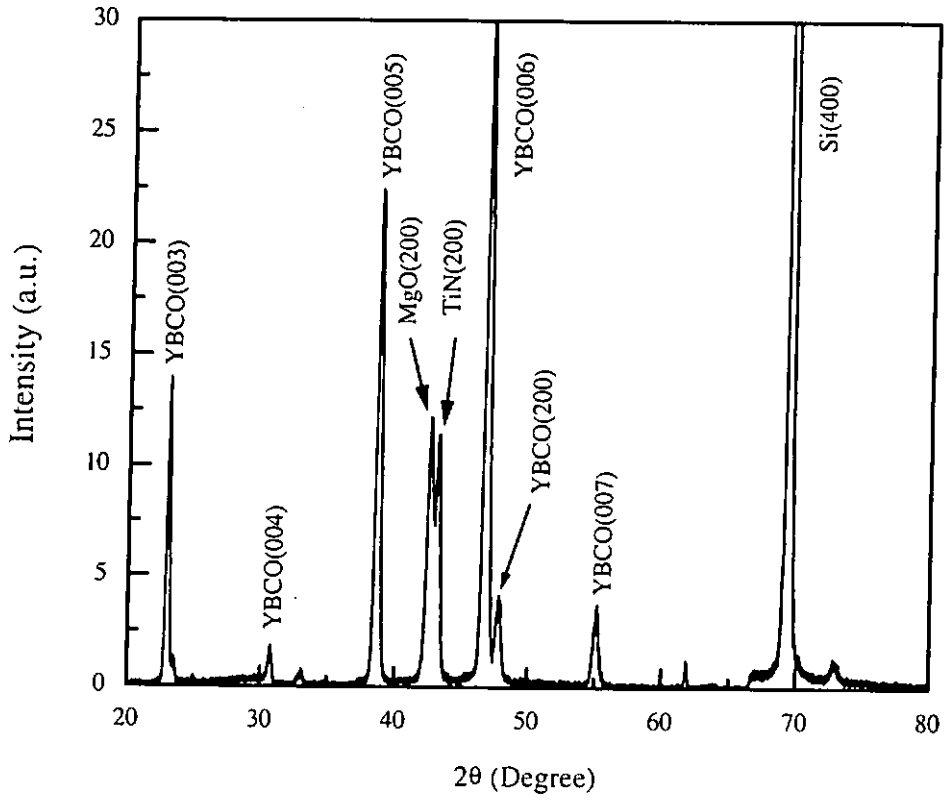

Fig.6.4 X-ray θ-2θ diffraction pattern for the YBCO/MgO/TiN/Si heterostructure. The YBCO layer was deposited at 750°C under an ambient oxygen pressure of 300 mTorr. The MgO and TiN layers were deposited at 650°C and 600°C, respectively, under a pressure of 4×10^{-6} Torr.

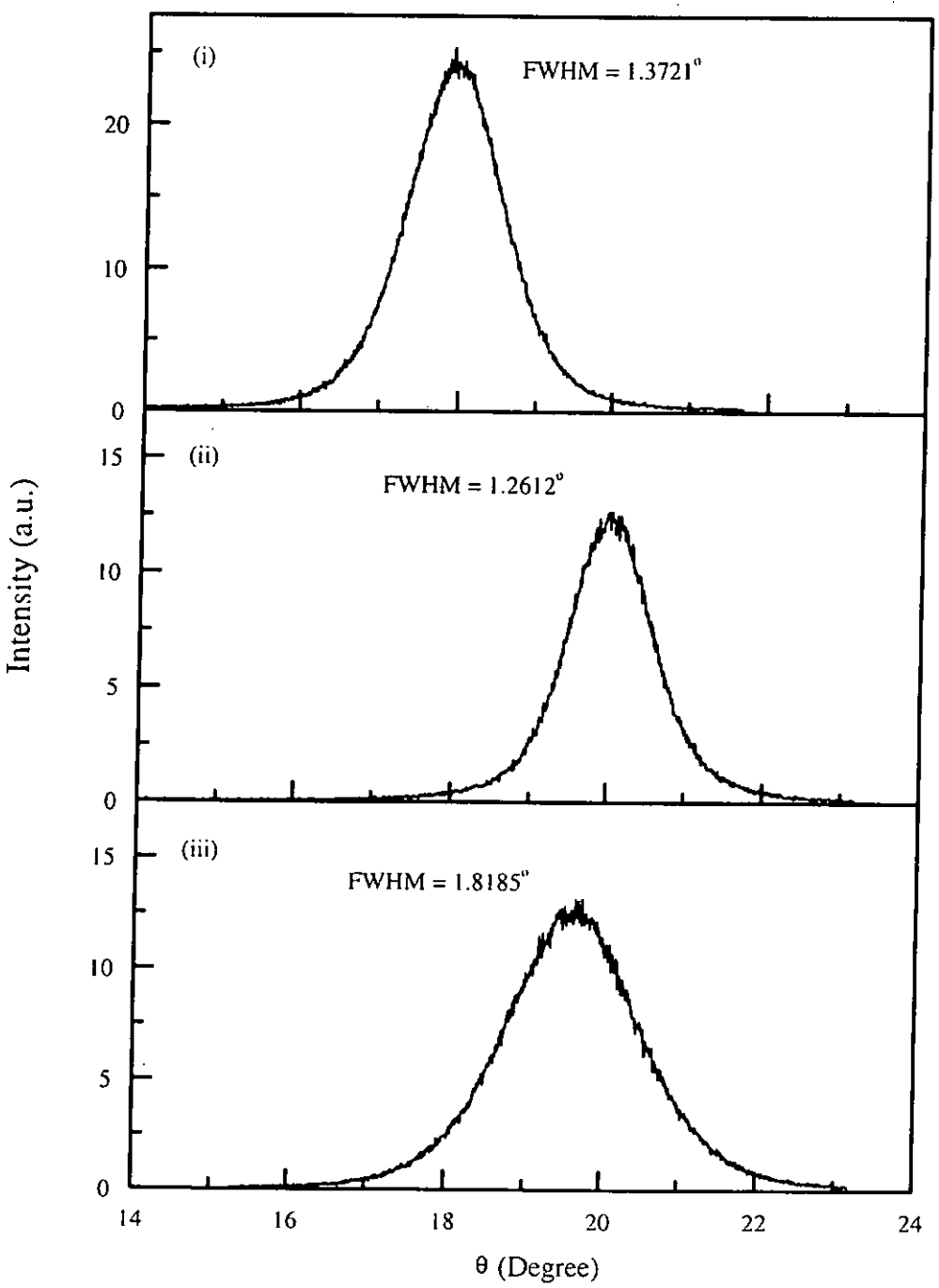

Fig.6.5 Rocking curves of (i) (005)YBCO, (ii) (200)MgO, and (iii) (200)TiN reflections. The YBCO layer was deposited at 700°C under an ambient oxygen pressure of 300 mTorr whereas the MgO and TiN layers were deposited at 650°C and 600°C, respectively, under a pressure of 4×10^{-6} Torr.

In Section 5.3.5.1, it is shown that film cracking becomes more severe when YBCO was deposited at a high deposition temperature, say, 750°C when using STO/TiN buffer layers. Therefore, we have lowered the deposition temperature of YBCO to 700°C for the subsequent experiments. Besides, as we will use the YBCO layer as thin oxide electrodes for the ferroelectric capacitors, the YBCO deposition time have also been reduced from 20 minutes to 6 minutes. For YBCO deposited for 20 minutes, the film thickness was about 900 nm as measured by the profiler and cross-section SEM imaging whereas that deposited for 6 minutes, the thickness was about 200 nm.

Fig.6.6 shows the X-ray θ-2θ diffraction patterns for the (a) YBCO/MgO/TiN/Si and (b) YBCO/STO/TiN/Si heterostrutures. The YBCO layer was deposited at 700°C under an ambient oxygen pressure of 300 mTorr for 6 minutes. The MgO and STO buffer layers were deposited at 650°C under a pressure of $4x10^{-6}$ Torr. The TiN layer in the two heterostructures was kept at 600°C and a pressure of $4x10^{-6}$ Torr. When comparing the two heterostructures, it is evident that using MgO as a buffer layer, the peaks formed are sharper which actually indicates that the films have better crystallinity. It is believed that MgO is a good oxygen diffusion barrier and can prevent TiN from oxidation. In case of using STO as a buffer layer, the TiN is being oxidized during the deposition and post-annealing of YBCO films which are required to be processed under high temperature and ambient oxygen pressure. This is evident from the weakening and broadened TiN(200) reflection in Fig.6.6b. Consequently, the oxidation of TiN will cause damaging structural defects and can have detrimental effect on the YBCO films and the overall

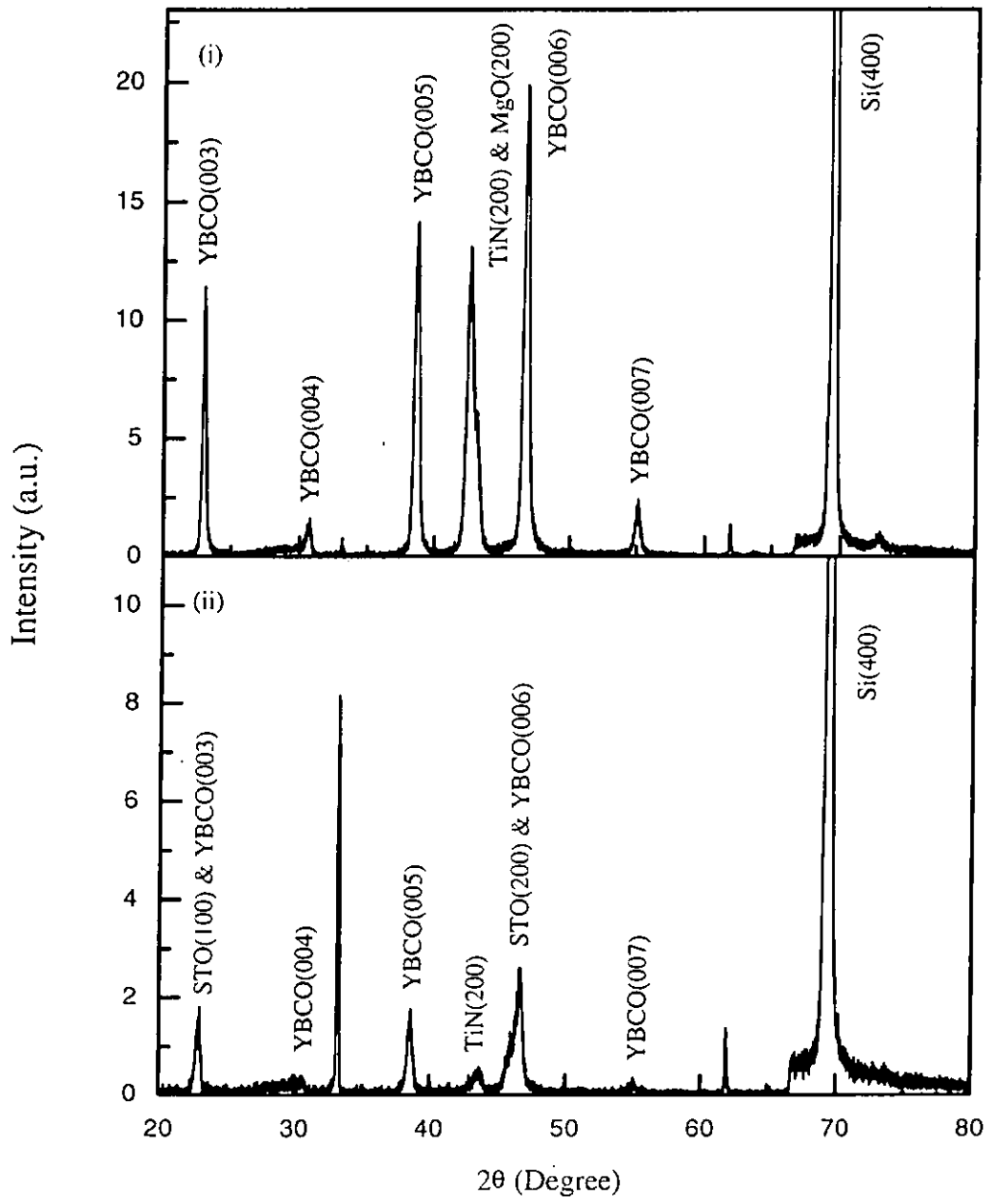

Fig.6.6 X-ray θ-2θ diffraction patterns for (a) YBCO/MgO/TiN/Si, and (b) YBCO/STO/TiN/Si. The YBCO layer was deposited at 700°C under an ambient oxygen pressure of 300 mTorr. Both MgO and STO layers were deposited at 650°C under a pressure of $4x10^{-6}$ Torr whereas the TiN was deposited at 600°C under a pressure of $4x10^{-6}$ Torr.

heterostructures.

For the YBCO/MgO/TiN/Si heterostructure, the FWHM of (005)YBCO reflection is 1.66° whereas (200)TiN & (200)MgO reflections is 2.59° as shown in Fig.6.7. Fig.6.8 shows the X-ray rocking curves of (005)YBCO and (200)TiN reflections for the YBCO/STO/TiN/Si heterostructure. Their FWHM are 1.74° and 1.86° respectively. Superficially, from the value of the FWHM obtained, it seems that the crystallinity of the YBCO/MgO/TiN/Si heterostructure is not better than the one using STO as a buffer layer. Nonetheless, if we compare the XRD profiles closely, we will discover that the signal to noise ratio is higher when using MgO as a buffer layer. This rather broad rocking curve profile of unresolved (200)TiN and (200)MgO may simply due to the small shift of (200)MgO reflection to low angle due to strain at the interface as described earlier. In Section 6.2.3, we will show the surface morphology of the YBCO/MgO/TiN/Si heterostructure is much better than that of the YBCO/STO/TiN/Si heterostructure. Needless to say, the surface morphology of the PZT/YBCO/MgO/TiN/Si heterostructure is also better than that of the PZT/YBCO/STO/TiN/Si heterostructure as will be shown in Section 7.2.1. Besides, a much better crystal quality of PZT films is formed when it is grown on the YBCO/MgO/TiN/Si heterostructure. The FWHM of the (200)PZT, (005)YBCO and (200)TiN & (200)MgO can be as low as 1.09°, 1.09° and 1.83° respectively.

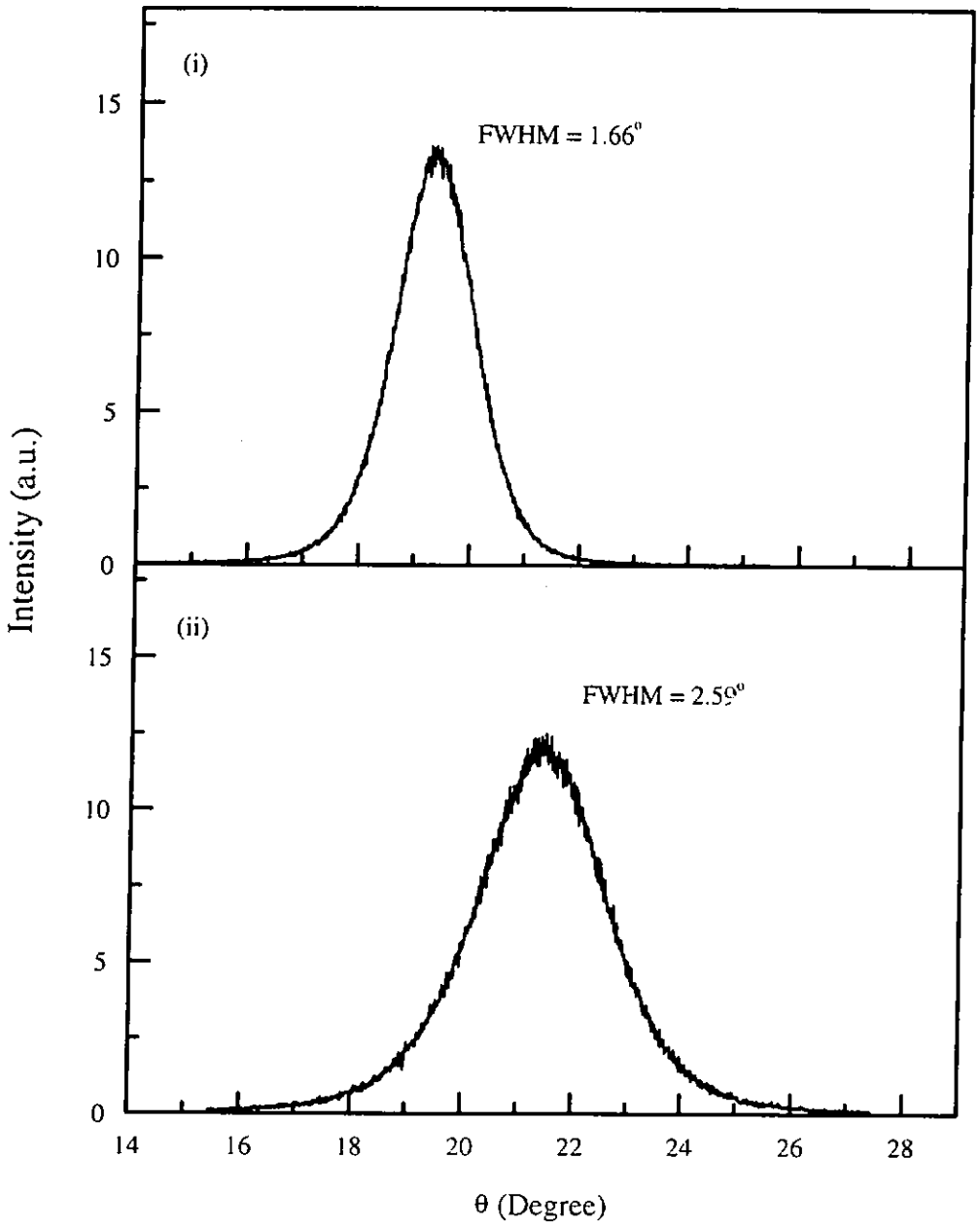

Fig.6.7 Rocking curves of (i) (005)YBCO and (ii) (200)TiN & (200)MgO reflections. The YBCO layer was deposited at 700°C under an ambient oxygen pressure of 300 mTorr whereas the MgO and TiN layers were deposited at 650°C and 600°C, respectively, under a pressure of 4×10^{-6} Torr.

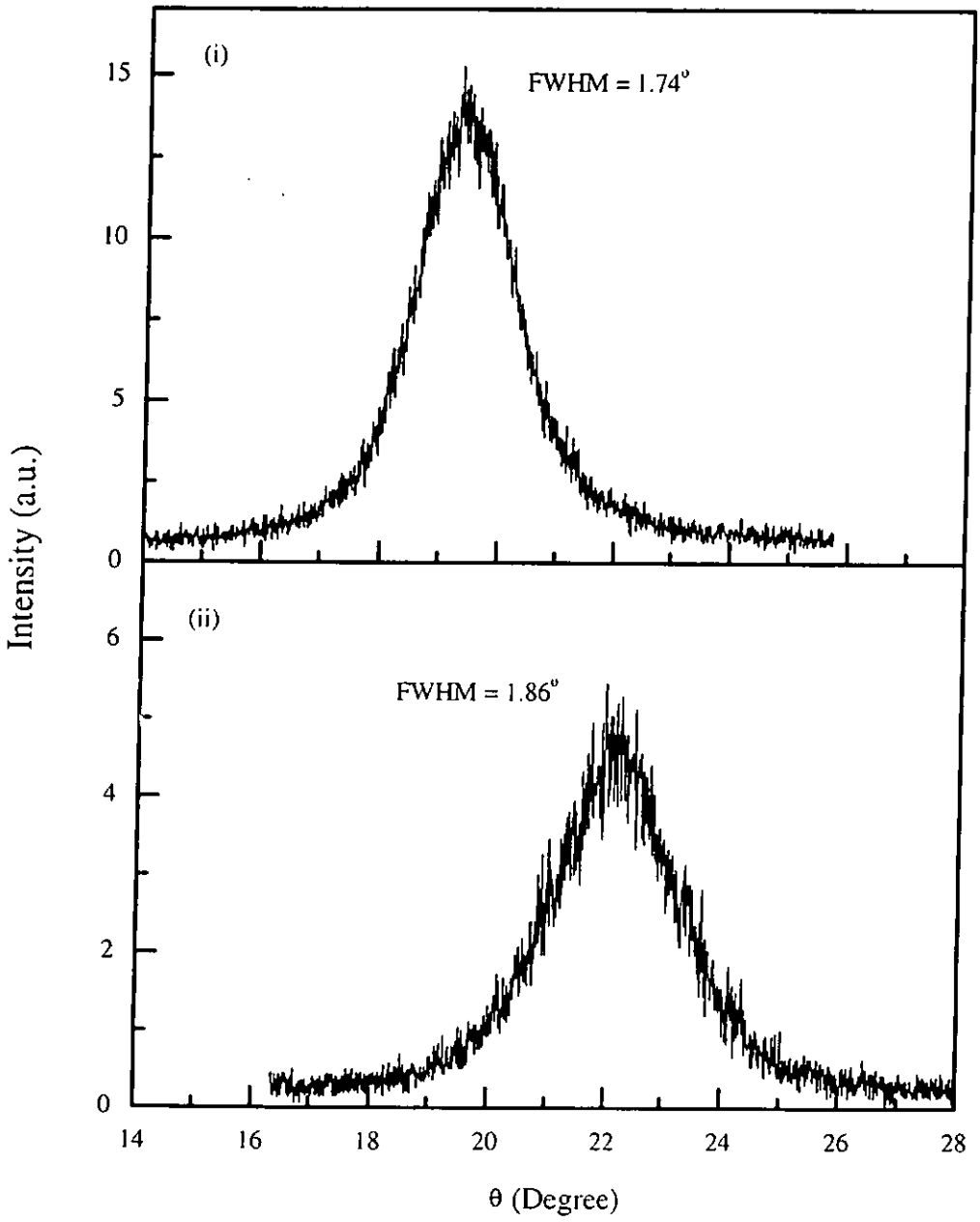

Fig.6.8 Rocking curves of (i) (005)YBCO, and (ii) (200)TiN reflections. The YBCO layer was deposited at 700°C under an ambient oxygen pressure of 300 mTorr whereas the STO and TiN layers were deposited at 650°C and 600°C, respectively, under a pressure of $4x10^{-6}$ Torr.

6.2.2 Cross-section of YBCO Thin Films on MgO/TiN/Si

Fig.6.9 shows the scanning electron micrograph of the cross-section of the YBCO/MgO/TiN/Si heterostruture. The YBCO layer was deposited at 750°C under an ambient oxygen pressure of 300 mTorr for 20 minutes. The MgO and TiN were deposited at 650°C and 600°C, respectively, under a pressure of $4x10^{-6}$ Torr. From the cross-section of the heterostrutures, three layers are clearly shown. The thickness was 900 nm, 120 nm and 200 nm for the YBCO, MgO and TiN layers respectively. It is evident that the different layers have a sharp interface. When compare this cross-section with the one having the YBCO/STO/TiN/Si heterostruture as shown in Fig.5.14, it is obvious that using MgO as a buffer layer, the interface formed is clearer. This again suggests that MgO is a better buffer layer than STO. The MgO layer is good enough to maintain the structural quality of TiN from oxidation during deposition and post-annealing of YBCO films which are required to be processed under high deposition temperature and ambient oxygen pressure.

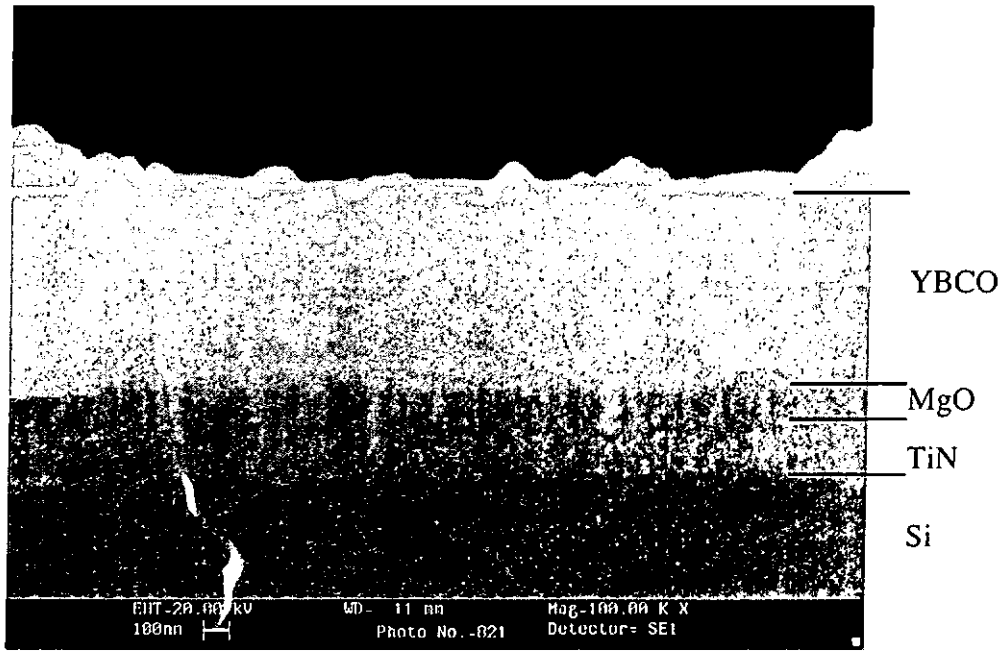

Fig.6.9 The scanning electron micrograph of the cross-section of the YBCO/MgO/TiN/Si heterostructure. The YBCO layer was deposited at 750°C under an ambient oxygen pressure of 300 mTorr for 20 minutes. The MgO and TiN were deposited at 650°C and 600°C respectively, under a pressure of 4 x 10^{-6} Torr.

6.2.3 Surface Morphologies of YBCO Thin Films Grown on MgO/TiN/Si and STO/TiN/Si Heterostructures

6.2.3.1 Comparison of YBCO Films Grown at High Deposition Temperature

In Section 5.3.5.1, we have shown that the YBCO films deposited on the STO/TiN/Si heterostructure at 750°C under an ambient oxygen pressure of 300 mTorr for 20 minutes, cracking occured (Fig.5.17). Nonetheless, there is no cracking occurs when MgO/TiN are used as the buffer layers. Fig.6.10 shows the surface morphology of YBCO films deposited on the MgO/TiN/Si heterostructure. Apart from some spherical particulates, which is a common PLD feature without shadow masks, there is no apparent cracking and holes on the surface of the YBCO film. It may be due to the fact that the thermal expansion coefficient of MgO (α_{MgO} ~ 13.5x10^{-6}/K) is much better match to that of YBCO (α_{YBCO} ~ 12.9x10^{-6}/K). (The thermal expansion coefficient of STO is α_{STO} ~ 8 x 10^{-6}/K.) Actually, the large difference in thermal expansion coefficients between YBCO and STO can create a large thermal strain in the films. As mentioned in Section 5.3.5.2, the difference in thermal expansion coefficient will cause the film under tensile stress when cool the film down from the deposition temperature. And in order to relax the strain, microcracks are then formed. Besides, cracking is more severe for the YBCO/STO/TiN/Si heterostructure as STO is not a good oxygen diffusion barrier to prevent the TiN films from oxidation during the deposition and post-annealing of YBCO films. As discussed in Section 5.3.1, under elevated temperature with high

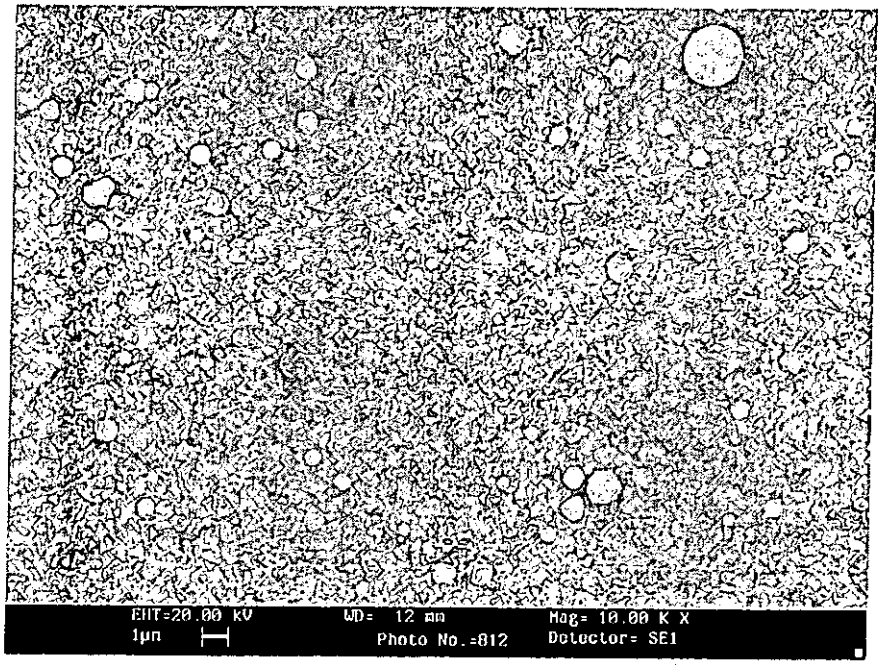

(i)

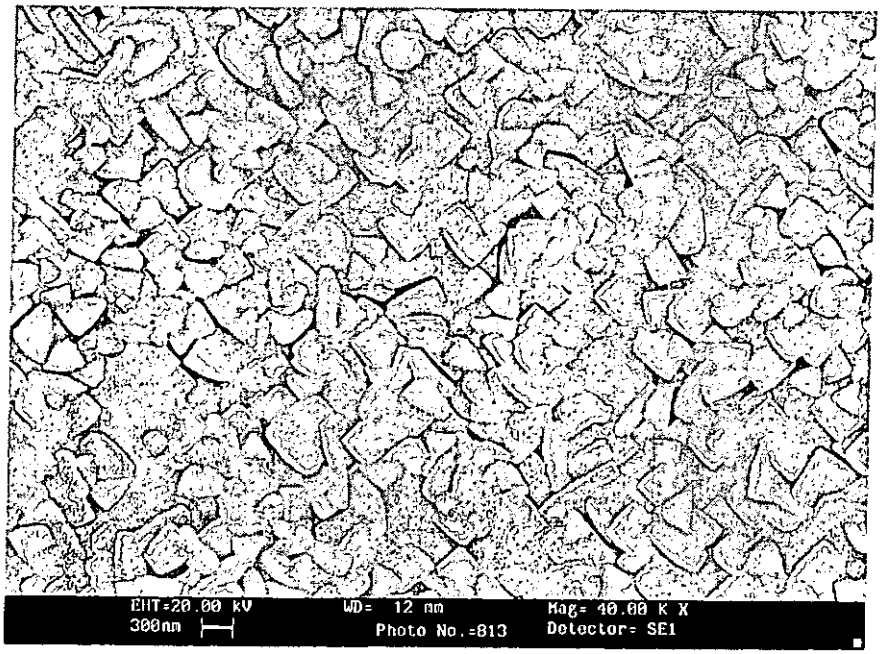

(ii)

Fig.6.10 Surface morphology of YBCO films deposited on the MgO/TiN/Si heterostructure:(i)magnification = $1x10^4$, (ii)magnification = $10x10^4$. The YBCO layer was deposited at 750°C under an ambient oxygen pressure of 300 mTorr, whereas that of the MgO and TiN buffer layers were deposited at 650°C and 600°C, respectively, under a pressure of $4 x10^{-6}$ Torr.

ambient oxygen pressure, the oxygen may diffuse through the STO capping layer. As a result, TiN is oxidized and the crystallinity of TiN is destroyed. The oxidation of TiN may cause damaging structural defects and can have detrimental effect on the YBCO films and the overall heterostructures.

6.2.3.2 Comparison of YBCO Films Grown at Low Deposition Temperature

Fig.6.11 and Fig.6.12 also show the surface morphologies of YBCO films on the MgO/TiN/Si and the STO/TiN/Si heterostrutures respectively. The YBCO layer was deposited at 700°C under an ambient oxygen pressure of 300 mTorr for 6 minutes. The MgO and STO buffer layers were also deposited at 650°C under a pressure of $4x10^{-6}$ Torr whereas the TiN layer in the two heterostructures was kept at 600°C and a pressure of $4x10^{-6}$ Torr. Again, when comparing the two heterostructures, it is evident that when using MgO as a buffer layer, the YBCO films have a much better surface morphology. The reasons are the same as discussed in Section 6.2.3.1.

In Section 5.3.5, we notice that the YBCO films can have different orientations under different substrate temperatures. For example, the YBCO films are a, b-oriented, having the c-axis of YBCO parallel to either [100] or [010] directions of STO when they are deposited at substrate temperature of 650°C and c-oriented with the c axis of YBCO parallel to the [001]STO when they are deposited at substrate temperature of 700°C or above. According to [Chan et al., 1989], the a, b-oriented

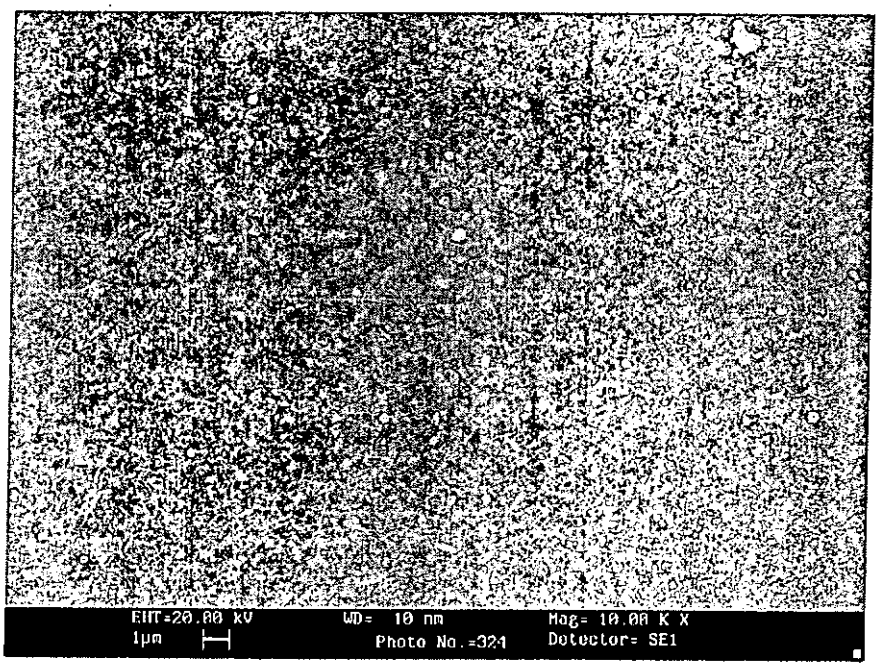

Fig.6.11 Surface morphology of the YBCO film deposited on the MgO/TiN/Si heterostructure. The YBCO layer was deposited at 700°C under an ambient oxygen pressure of 300 mTorr, whereas the MgO and TiN buffer layers were deposited at 650°C and 600°C, respectively, under a pressure of 10^{-6} Torr.

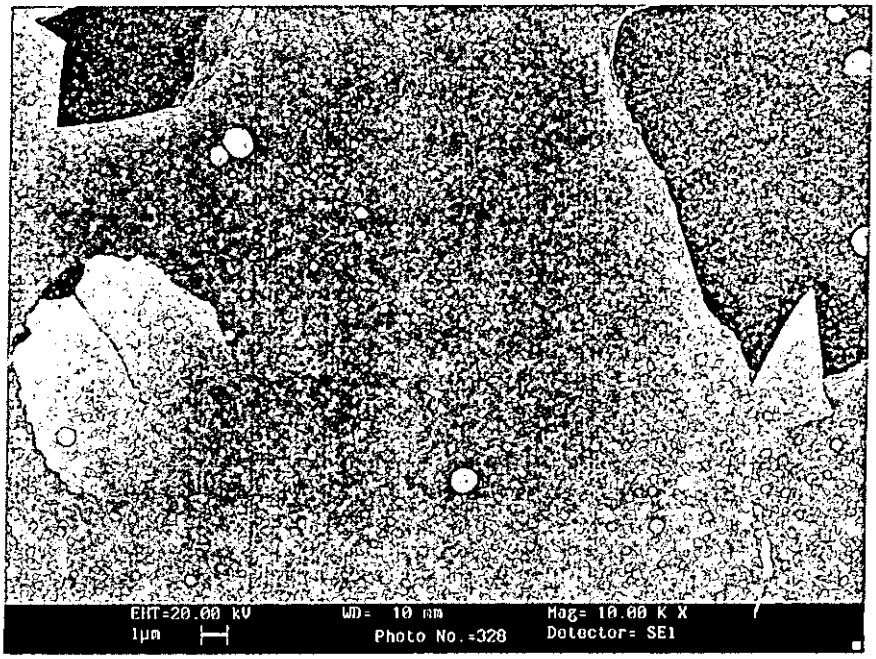

Fig.6.12 Surface morphology of the YBCO film deposited on the STO/TiN/Si heterostructure. The YBCO layer was deposited at 700°C under an ambient oxygen pressure of 300 mTorr, whereas the STO and TiN buffer layers were deposited at 650°C and 600°C, respectively, under a pressure of 10^{-6} Torr.

grains appear as cross bars and the c-oriented grains appear as disks. Obviously, our films do show similar consistency with the deposition temperatures. In Fig.6.11 and Fig.6.12, we can see that the YBCO films appear as disks which mean that the YBCO films are c-oriented. Indeed, the reason why we decide to deposit YBCO films at 700°C is that it gives c-oriented YBCO films and better surface morphologies. Of course, when the YBCO films are deposited at 750°C, they are also c-oriented. However, it is always desirable to use a lower deposition temperature for growing films with acceptable qualities

6.3 Electrical Property of the YBCO Films on the MgO/TiN/Si and the STO/TiN/Si Heterostructures

Fig.6.13 and Fig.6.14 show the resistivity against temperature of the YBCO/MgO/TiN/Si and the YBCO/STO/TiN/Si heterostructures. The MgO and STO buffer layers were deposited at 650°C whereas the TiN layers in the two heterostructures were grown at 600°C. The deposition ambient was kept at the base pressure of 4×10^{-6} Torr. The YBCO layer was deposited at 700°C under an ambient oxygen pressure of 300 mTorr for 6 minutes. After the deposition, the as-grown films were then post-annealed at 500°C under an oxygen atmosphere for 30 minutes.

For the YBCO/MgO/TiN/Si heterostructure, the YBCO film shows metallic resistivity versus temperature characteristic and has a transition temperature of 88 K. The YBCO layer in the YBCO/STO/TiN/Si heterostructure, however, shows semiconducting property versus temperature even though it does make a transition at

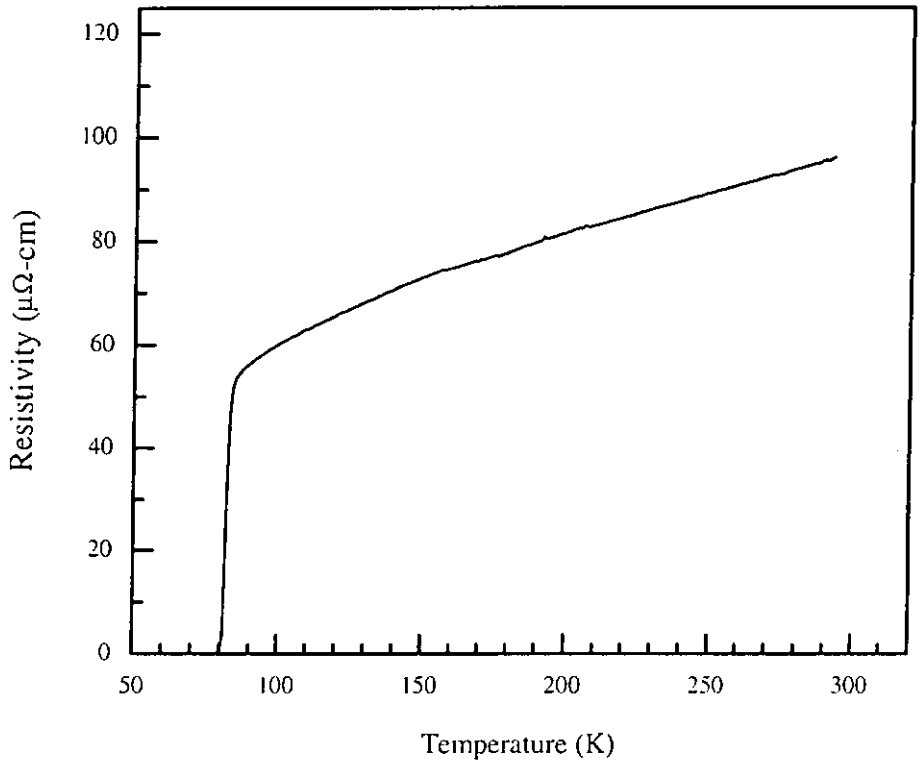

Fig.6.13 Resistivity against temperature of the YBCO film deposited on the MgO/TiN/Si heterostructure. The YBCO layer was deposited at 700°C under an ambient oxygen pressure of 300 mTorr for 6 minutes. The MgO and TiN buffer layers were deposited at 650°C and 600°C, respectively, under a pressure of 4×10^{-6} Torr.

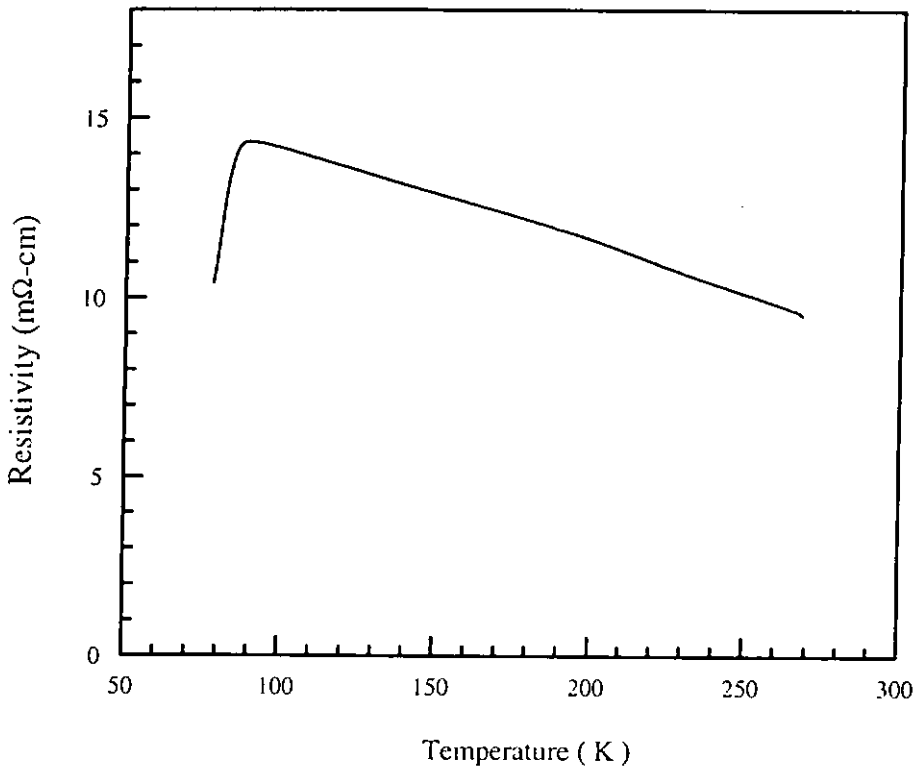

Fig.6.14 Resistivity against temperature of the YBCO film deposited on the STO/TiN/Si heterostructure. The YBCO layer was deposited at 700°C under an ambient oxygen pressure of 300 mTorr for 6 minutes. The STO and TiN buffer layers were deposited at 650°C and 600°C, respectively, under a pressure of 4×10^{-6} Torr.

88 K. Nevertheless, it does not drop off gently and remain non-zero at 78 K. In Section 6.2.3.2, we have seen the surface morphology of this heterostructure as shown in Fig.6.12. Microcracks are seen running along the film surface. Actually, these cracks may severely degrade both the structural and electrical qualities of the superconductor film.

In conclusion, it is clearly seen that the MgO/TiN buffer layers allow a better crystal growth of YBCO on Si. The superior quality of MgO may attribute to the fact that MgO appears to be a much better oxygen diffusion barrier than STO during the growth of YBCO films, in which high ambient oxygen pressure and elevated deposition temperature are involved. Furthermore, the thermal expansion coefficient of MgO (α_{MgO} ~ 13.5 x 10^{-6}/K) is much better match with that of YBCO (α_{YBCO} ~ 12.9 x 10^{-6}/K). (The thermal expansion coefficient of STO is α_{STO} ~ 8 x 10^{-6}/K.) This will help to lessen the thermally induced stress on the YBCO films and hence retain a crack free YBCO layer.

Chapter 7

Structural Characterization and Ferroelectric Properties of $Pb(Zr_{0.52}Ti_{0.48})O_3$ Thin Films

7.1 Introduction

$Pb(Zr_xTi_{1-x})O_3$ (PZT), a pseudo-cubic perovskite oxide having a lattice constant of 4.08Å has been receiving much attention due to its many useful and important properties. For its composition near the morphotropic phase boundary, $Pb(Zr_{0.52}Ti_{0.48})O_3$ exhibits the best properties such as a low coercive field, substantial remnant polarization, large dielectric constant and high piezoelectric coefficient. Indeed, PZT is one of the best known and studied ferroelectrics which offer a host of exciting applications such as non-volatile memories (NVM's) and dynamic random access memories (DRAM's). In view of this, it would be very useful if PZT can be integrated with silicon. Yet, suitable buffer layers with excellent diffusion barrier characteristics are necessary as the growth of PZT films on Si(100) substrates is not possible due to the high diffusivities of PZT constituents into silicon. Besides, lattice and domain matching substrates are required for epitaxial growth of PZT films. In addition, polarization switching fatigue problems [Ramesh et al., 1992], charge retention [Ramesh et al., 1992], imprint [Lee et al., 1995; Lee et al., 1996] and leakage current [Stolichnov et al., 1999] need to be resolved.

7.2 Characterization of PZT/YBCO/MgO/TiN/Si and PZT/YBCO/STO/TiN/Si

In this chapter, the structural characterization of the PZT films grown on the YBCO/MgO/TiN/Si and YBCO/STO/TiN/Si heteroepitaxial structures are discussed. Besides, the ferroelectric properties of the epitaxial ferroelectric thin-film capacitor based on the Au/$Pb(Zr_{0.52}Ti_{0.48})O_3$/$YBa_2Cu_3O_{7-x}$/MgO/TiN/Si heterostructure are presented. Issues concerning fatigue and the leakage current are addressed at the present studies.

7.2.1 Structural Characterization of PZT/YBCO/MgO/TiN/Si and PZT/YBCO/STO/TiN/Si

The target used for fabricating the PZT films was lead-enriched, i.e. $Pb(Zr_{0.52}Ti_{0.48})O_3$ + 10% PbO ($Pb_{1.1}(Zr_{0.52}Ti_{0.48})O_{3.1}$). All PZT films were deposited at 650°C under an ambient oxygen pressure of 250 mTorr. The laser fluence, repetition rate and deposition time used were 2.5 J/cm^2, 10Hz and 25 minutes respectively. The thickness of the PZT films was about 850 nm as measured from the cross-section SEM image.

Fig.7.1 shows the X-ray θ-2θ diffraction pattern of the PZT film deposited on the YBCO/MgO/TiN/Si heterostruture. The PZT film was deposited at 650°C under an ambient oxygen pressure of 250 mTorr whereas the YBCO film was deposited at 700°C under an ambient oxygen pressure of 300 mTorr. The MgO and TiN films

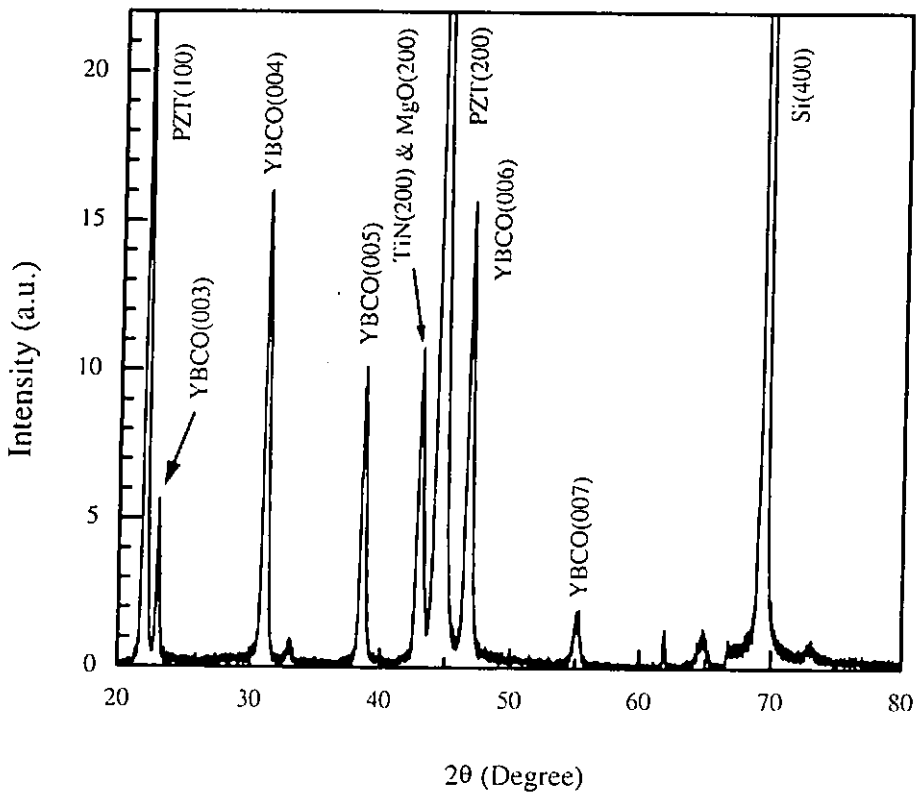

Fig.7.1 X-ray θ-2θ diffraction pattern for PZT/YBCO/MgO/TiN/Si. The PZT layer was deposited at 650°C under an ambient oxygen pressure of 250 mTorr whereas the YBCO layer was deposited at 700°C under an ambient oxygen pressure of 300 mTorr. The MgO and TiN layers were deposited at 650°C and 600°C, respectively, under a pressure of 4×10^{-6} Torr.

were deposited at 650°C and 600°C, respectively, under a pressure of $4x10^{-6}$ Torr. It is seen that a highly c-axis oriented YBCO film with strong (00ℓ) reflections are prepared. Besides, (200) reflections of TiN, MgO and YBCO were also recorded. The FWHM of the rocking curves of the (200)PZT, (005)YBCO, (200)MgO and (200)TiN reflections were 1.10°, 1.09° and 1.83° respectively as shown in Fig.7.2. These values suggest that the four layers are highly oriented crystalline films. The MgO layer helps to maintain the structural quality of TiN from oxidation during the growth of YBCO and PZT in ambient oxygen. The epitaxy of the films are confirmed by 360° ϕ-scans of (220)PZT, (220)YBCO, (220)MgO, (220)TiN and (220)Si reflections and the result shows that they have a similar 360° ϕ-scans profile as that shown in Fig.5.11. In all these ϕ-scans, four characteristics peaks of 4-fold symmetry are observed. The positions of the four peaks from the films are in good match. This strongly suggests that all these films are epitaxial growth, and cube-on-cube for some of them, grown on top of the Si substrate.

Fig.7.3 shows another X-ray θ-2θ diffraction pattern of the PZT/YBCO/MgO/TiN/Si heterostruture with the deposition conditions same as that shown in Fig.7.1. However, the X-ray diffraction pattern does show some difference. In Fig.7.3, the (200)MgO and (200)TiN reflections have been recorded as two resolved peaks. In addition, the (200)YBCO peak has also detected. This case is the same as that shown in Fig.6.4. Nonetheless, whether there is an inter-relationship between the occurrence of (200)YBCO and the separation of the (200)MgO and (200)TiN peaks, cannot be determined yet. The crystallinity of the

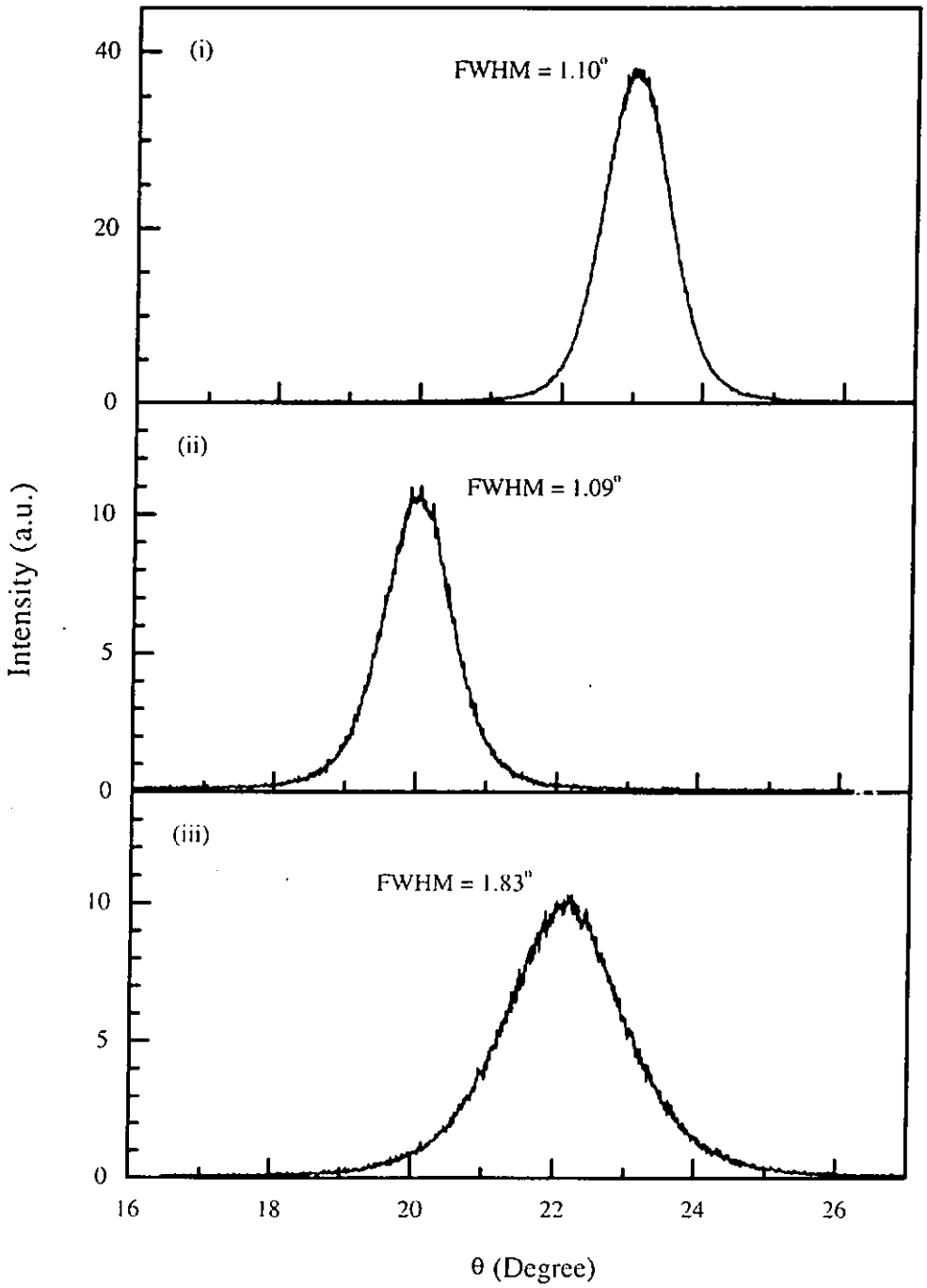

Fig.7.2 Rocking curves of (i) (200)PZT, (ii) (005)YBCO, (iii) (200)TiN & (200)MgO reflections. The PZT, YBCO, MgO and TiN films were deposited at 650°C, 700°C, 650°C and 600°C, respectively. The deposition pressures of them were 250 mTorr, 300 mTorr, $4x10^{-6}$ Torr and $4x10^{-6}$ Torr, respectively.

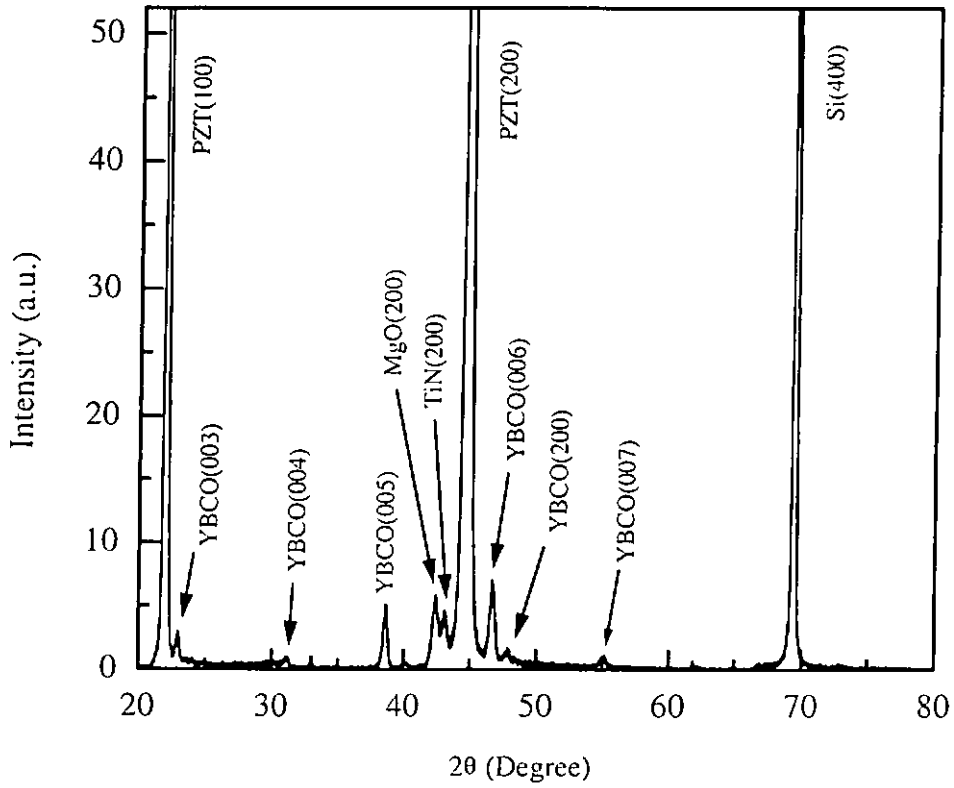

Fig.7.3 X-ray θ-2θ diffraction pattern for the PZT/YBCO/MgO/TiN/Si heterostructure. The PZT layer was deposited at 650°C under an ambient oxygen pressure of 250 mTor whereas the YBCO layer was deposited at 700°C under an ambient oxygen pressure of 300 mTorr. The MgO and TiN layers were deposited at 650°C and 600°C, respectively, under a pressure of 4×10^{-6} Torr.

films formed, however, is not as good as that shown in Fig.7.1. However, they are still well oriented films. The FWHM of the (200)PZT, (005)YBCO, (200)MgO and (200)TiN are 1.14°, 1.44°, 1.64° and 2.22° respectively as shown in Fig.7.4. And similarly, from the 360° ϕ-scans of (220)PZT, (220)YBCO, (220)MgO, (220)TiN and (220)Si reflections, they do show good heteroepitaxial structure.

Fig.7.5 shows the X-ray θ-2θ diffraction pattern of the PZT films deposited on the YBCO/STO/TiN/Si heterostruture. The deposition conditions for all the layers were the same as that of the corresponding layers shown in Fig.7.1 for the YBCO/MgO/TiN/Si heterostruture. As expected, the crystallinity of the different layers formed was not as good as the one using MgO as a buffer layer. From the profile, we can see that the peaks formed were not so sharp and the (200)TiN reflection disappeared. Actually, the reason for these occurrences is primarily due to the oxidation of the TiN buffer layer as discussed previously. The FWHM of the (200)PZT and (005)YBCO are 1.38° and 1.45° respectively as shown in Fig.7.6.

7.2.2 Cross-section of the $Pb(Zr0_{0.52}Ti_{0.48})O_3$ Thin Films on the YBCO/MgO/TiN/Si Heterostructure

Fig.7.7 shows the scanning electron micrograph (SEM) of the cross-section of the PZT/YBCO/MgO/TiN/Si heterostructure in which the deposition conditions for the different layers are the same as that shown in Fig.7.1. The PZT layer was deposited at 650°C under an ambient oxygen pressure of 250 mTorr whereas the YBCO layer was deposited at 700°C under an ambient oxygen pressure of 300

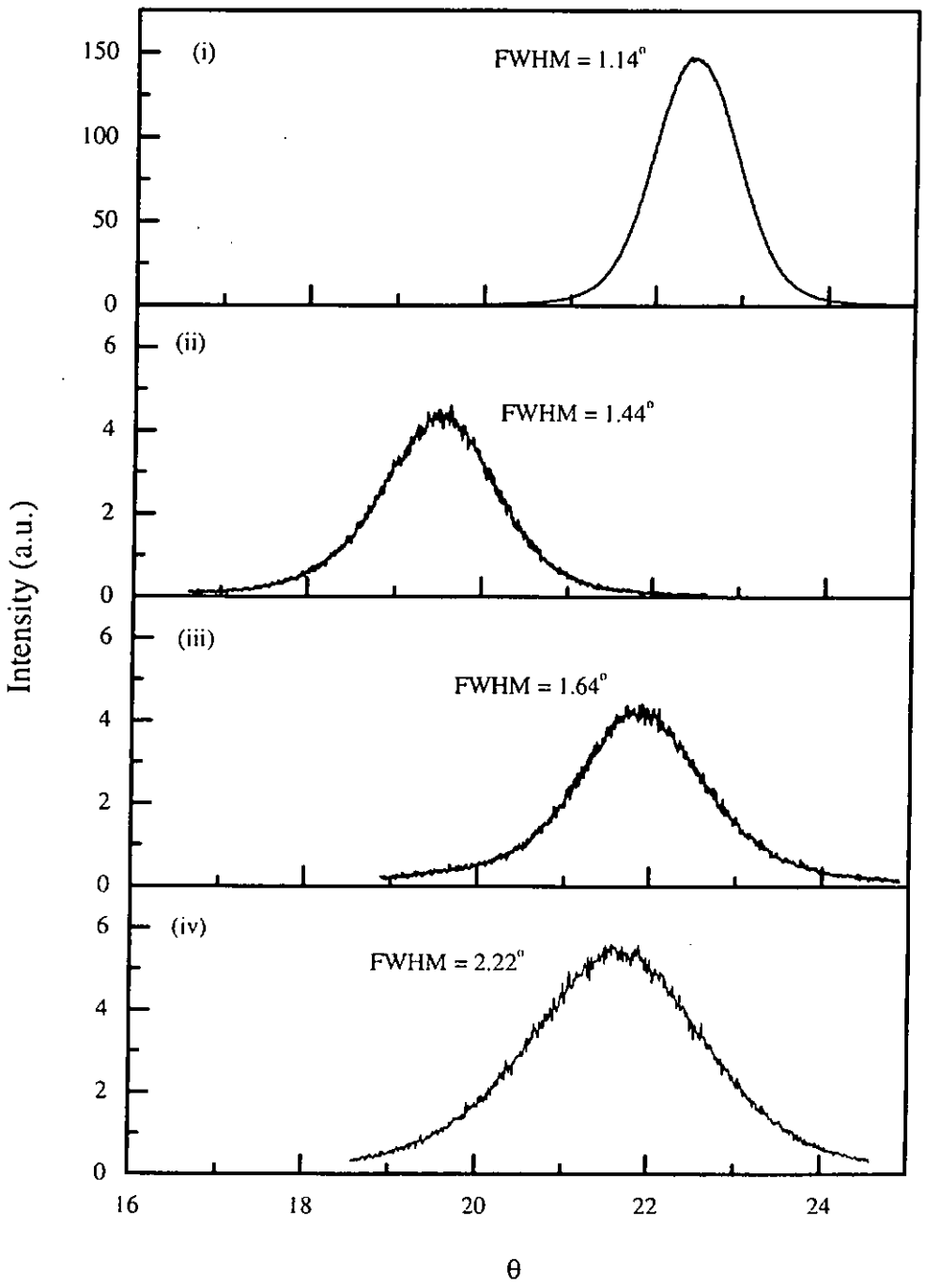

Fig.7.4 Rocking curves of (i) (200)PZT, (ii) (005)YBCO, (iii) (200)MgO and (iv) (200)TiN reflections. The PZT, YBCO, STO and TiN films were deposited at 650°C, 700°C, 650°C and 600°C, respectively. The deposition pressures of them were 250 mTorr, 300 mTorr, $4x10^{-6}$ Torr and $4x10^{-6}$ Torr, respectively.

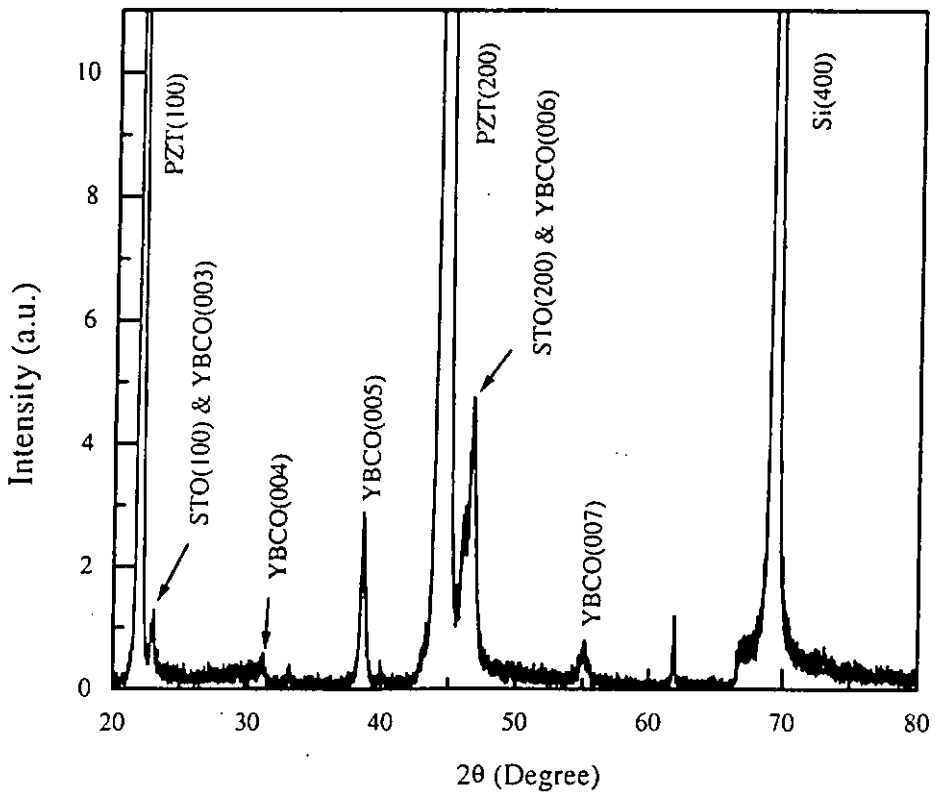

Fig.7.5 X-ray θ-2θ diffraction pattern for the PZT/YBCO/STO/TiN/Si heterostructure. The PZT layer was deposited at 650°C under an ambient oxygen pressure of 250 mTorr whereas YBCO was deposited at 700°C under an ambient oxygen pressure of 300 mTorr. The STO and TiN layers were deposited at 650°C and 600°C, respectively, under a pressure of 4×10^{-6} Torr.

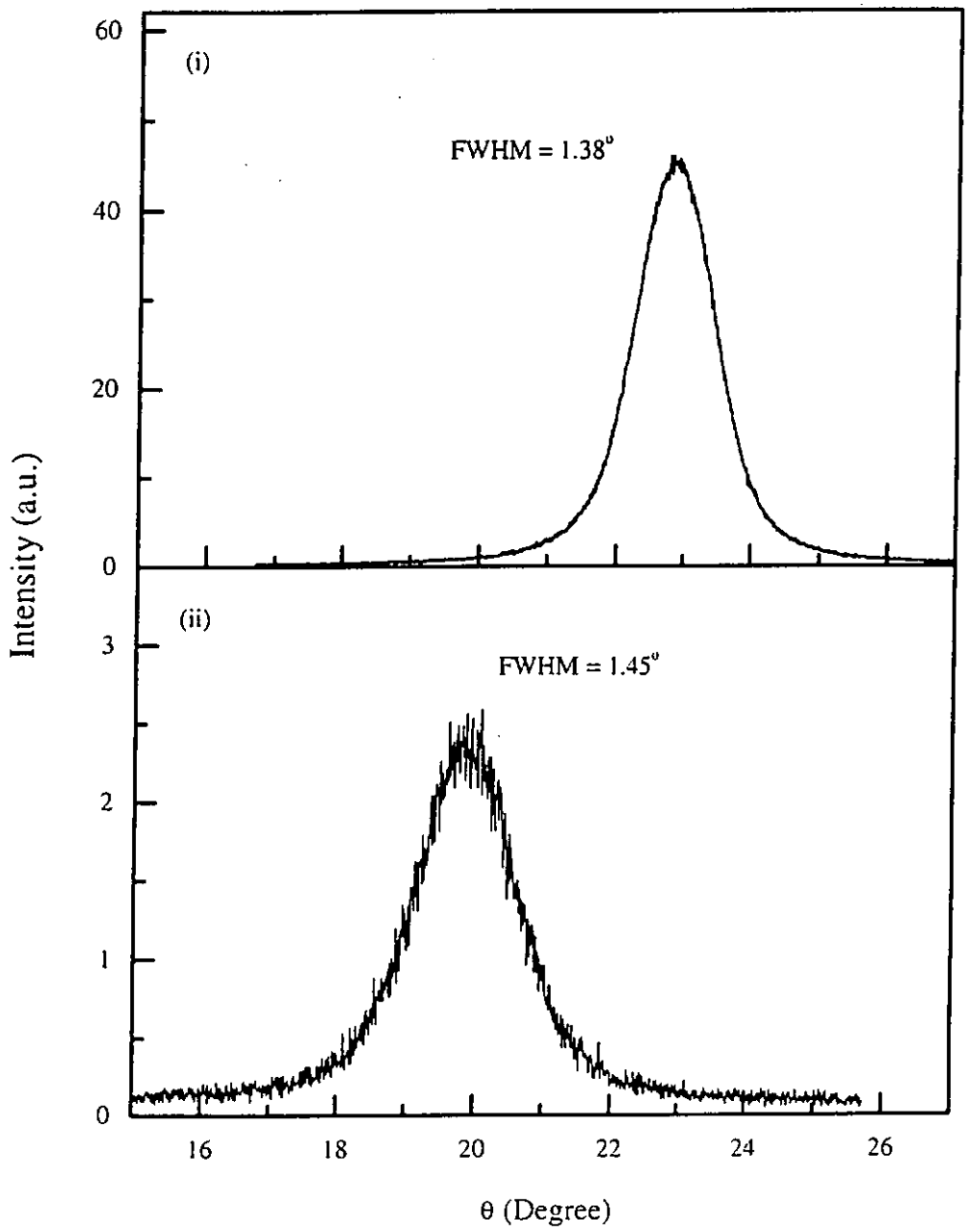

Fig.7.6 Rocking curves of (i) (002)PZT and (ii)(005)YBCO reflections.

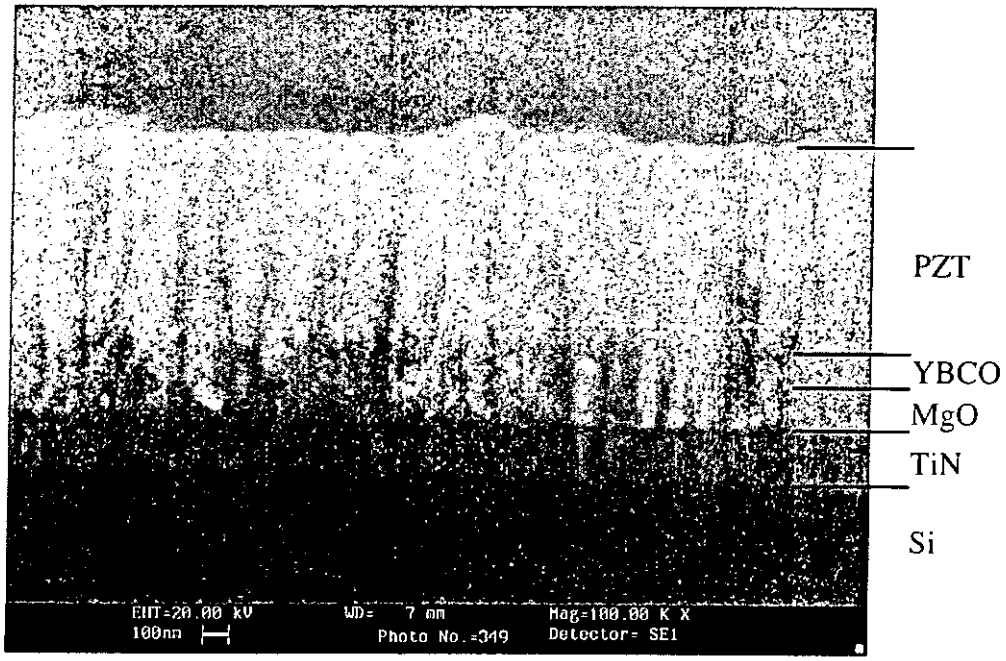

Fig.7.7 The scanning electron micrograph of the cross-section of the PZT/YBCO/MgO/TiN/Si heterostructure. The PZT layer was deposited at 650 °C under an ambient oxygen pressure of 250 mTorr for 20 minutes whereas the YBCO layer was deposited at 700 °C under an ambient oxygen pressure of 300 mTorr for 6 minutes. The MgO and TiN were deposited at 650 °C and 600 °C respectively, under a pressure of 4×10^{-6} Torr.

mTorr. The MgO and TiN were deposited at 650°C and 600°C, respectively, and under a pressure of $4x10^{-6}$ Torr. From the cross-section SEM imaging, the thickness was about 850 nm, 200 nm, 120 nm and 200 nm for the PZT, YBCO, MgO and TiN layers respectively. Clearly, the four layers have sharp and clean interfaces. Same as that discussed in Section 6.2.2, the MgO layer is good enough to maintain the structural quality of the heteroepitaxial structure.

7.2.3 Surface Morphologies of the $Pb(Zr_{0.52}Ti_{0.48})O_3$ Thin Films on the YBCO/MgO/TiN/Si and the YBCO/STO/TiN/Si Heterostructures

Fig.7.8 and Fig.7.9 show the surface morphologies of PZT films deposited on the YBCO/MgO/TiN/Si and the YBCO/STO/TiN/Si heterostructures. Again, the deposition conditions for the different layers are the same as that described for Fig.7.1. The PZT layer was deposited at 650°C under an ambient oxygen pressure of 250 mTorr whereas the YBCO layer was deposited at 700°C under an ambient oxygen pressure of 300 mTorr. The MgO and TiN were deposited at 650°C and 600°C, respectively, under a pressure of $4x10^{-6}$ Torr. Obviously, there is big difference in the surface morphologies of the PZT films such as holes are observed in Fig.7.9 but not in Fig.7.8. Actually, this phenomenon is the same as that discussed in Section 6.2.3.1. The occurrence of holes is due to the large difference in thermal expansion coefficients between YBCO and STO and the oxidation of TiN films during deposition and post-annealing of PZT and YBCO films.

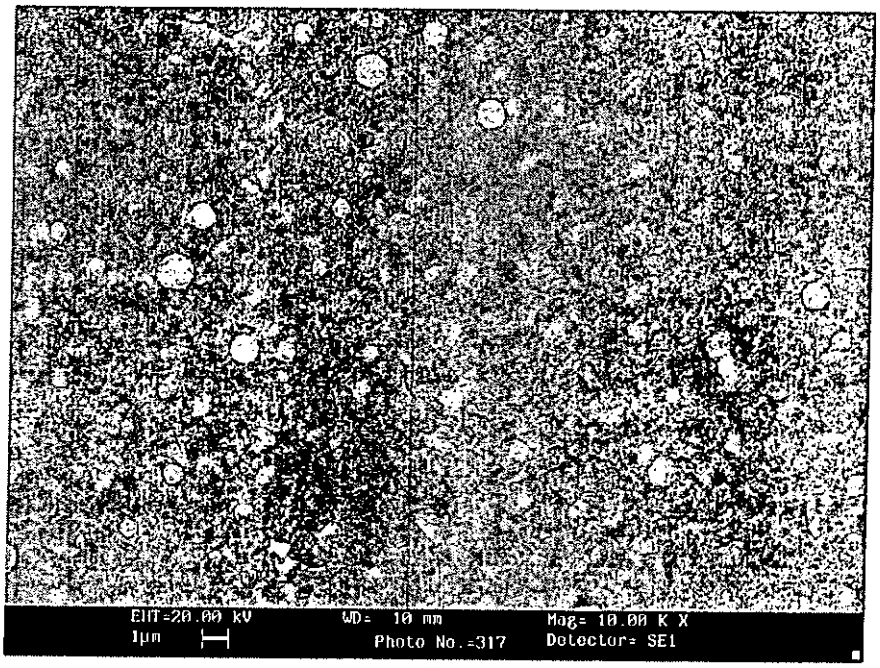

(i)

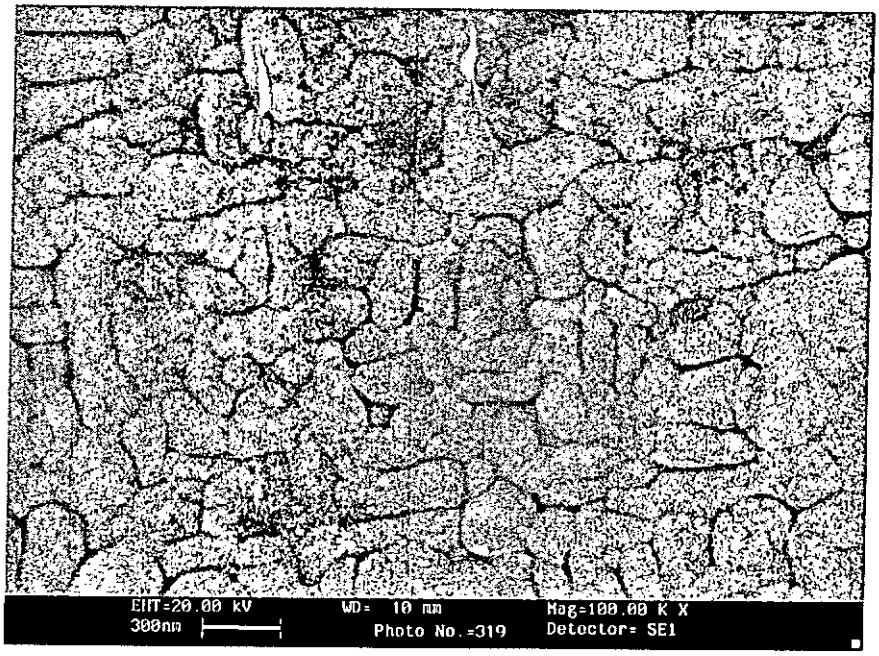

(ii)

Fig.7.8 Surface morphology of the PZT film deposited on the YBCO/MgO/TiN/Si heterostructure: (i) magnification = 1×10^{4}, (ii) magnification = 10×10^{4}. The PZT layer was deposited at 650°C under an ambient oxygen pressure of 250 mTorr, whereas the YBCO layer was deposited at 700°C under an ambient oxygen pressure of 300 mTorr. The MgO and TiN buffer layers were deposited at 650°C and 600°C, respectively, under a pressure of 10^{-6} Torr.

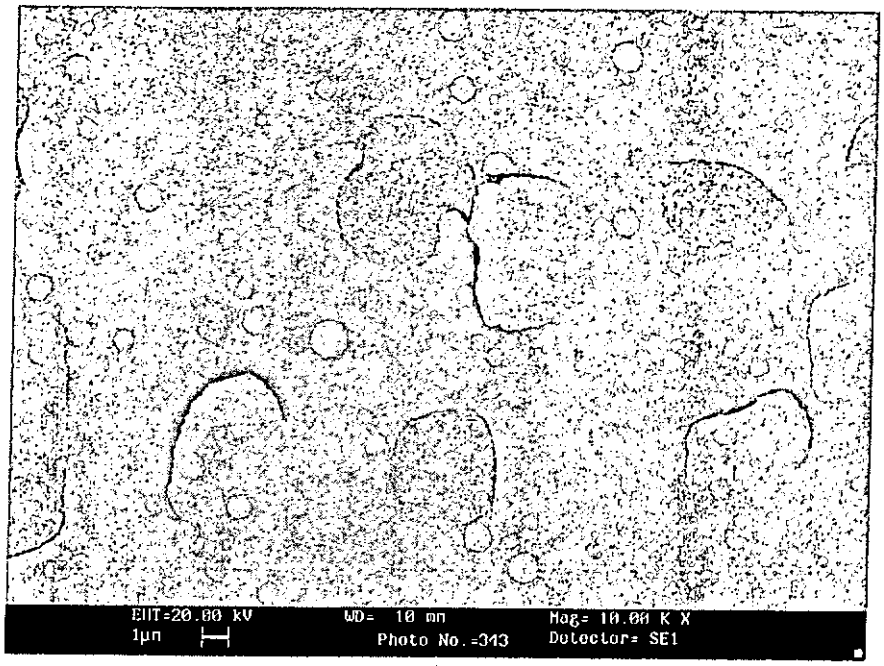

(i)

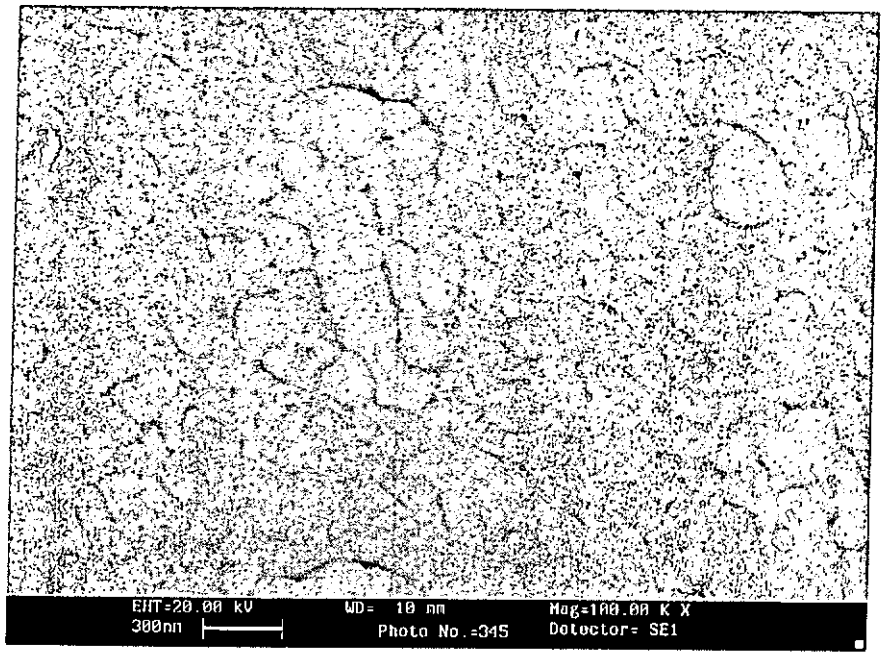

(ii)

Fig.7.9 Surface morphology of the PZT film deposited on the YBCO/STO/TiN/Si heterostructure: (i) magnification = 1×10^4, (ii) magnification = 10×10^4. The PZT layer was deposited at 650°C under an ambient oxygen pressure of 250 mTorr, whereas the YBCO layer was deposited at 700°C under an ambient oxygen pressure of 300 mTorr. The STO and TiN buffer layers were deposited at 650°C and 600°C, respectively, under a pressure of 10^{-6} Torr.

In Fig.7.8, apart from the scattered spherical particulates which can be eliminated by using a shadow mask, it is clear that the film is crack-free and the grains of the multi-layer are densely packed. The grain size of the PZT film grown under the deposition condition as stated in Fig.7.8 ranges from 140 nm to 510 nm.

7.3 Ferroelectric Properties of PZT Thin Films

7.3.1 Hysteresis Loop

Fig.7.10 shows the schematic diagram of the Au/PZT/YBCO/MgO/TiN/Si heterostructure capacitor. The top most gold layer was deposited by sputtering on PZT to act as the top electrode. Its thickness is about 100 nm. It was patterned by contact mask into circular spot with diameter of 320 μm. All other layers were in-situ deposited by the PLD with the same deposition conditions as mentioned in Section 7.2.1. The PZT layer was deposited at 650°C under an ambient oxygen pressure of 250 mTorr whereas the YBCO layer was deposited at 700°C under an ambient oxygen pressure of 300 mTorr. The MgO and TiN were deposited at 650°C and 600°C, respectively, under a pressure of 4×10^{-6} Torr.

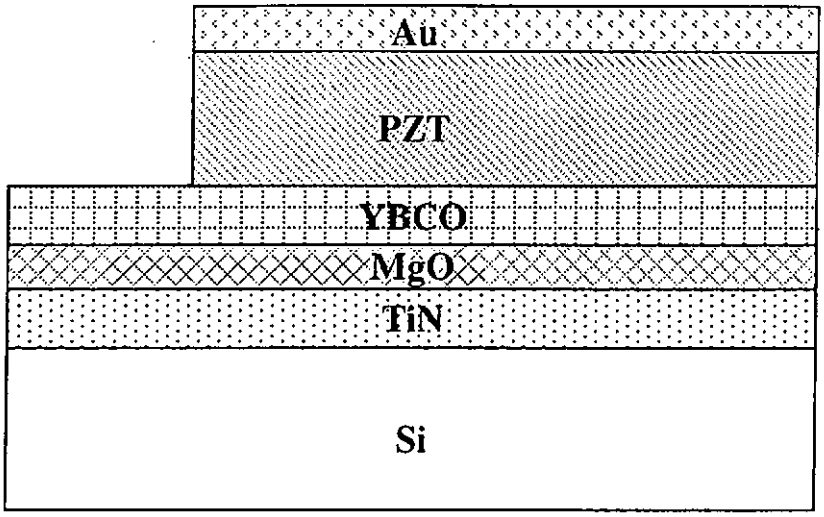

Fig 7.10 Schematic diagram of the Au/PZT/YBCO/MgO/TiN/Si heterostructure capacitor.

Fig.7.11 and Fig.7.12 show the P-E hysteresis loops of the Au/PZT/YBCO/MgO/TiN/Si and the Au/PZT/YBCO/LAO capacitors. The datas were obtained in the pulse test with driving voltages of 7 V, 9 V, 11 V, 13 V and 15 V. In Fig.7.11, it is seen that the capacitor has a square and well saturated loop with remnant polarization (P_r), saturation polarization (P_s) and coercive field (E_c) of 24 $\mu C/cm^2$, 40 $\mu C/cm^2$ and 47 kV/cm respectively. Actually, these values are comparable to that grown on single crystalline substrate as shown in Fig.7.12. The remnant polarization (P_r), saturation polarization (P_s) and coercive field (E_c) are about 36 $\mu C/cm^2$, 42 $\mu C/cm^2$ and 47 kV/cm respectively. These results are close to those reported by Wu et al. [2000] in which the remnant polarization is 35-40 $\mu C/cm^2$ and the coercive field is 40-50 kV/cm.

In Fig.7.11 and Fig.7.12, it is noted that the hysteresis loops are a little asymmetric in shape, which may be attributed to the different top and bottom electrodes and also oxygen vacancies and trapped electrons near the electrodes at the bottom and top of the device [Lee et al., 1996]. The absolute value of the negative coercive field E_c^- was less than that of the positive coercive field E_c^+, a feature similar to the reported case for the Au/$PbTiO_3$/$YBa_2Cu_3O_{7-\delta}$ capacitor [Gao et al., 2000]. Gao et al. suggested that the larger difference between the work function of YBCO and PTO than that of Au and PTO results in higher barrier height and so the asymmetry of electric properties of Au/PTO/YBCO capacitor. Besides, they also suggested that the asymmetry is due to the lattice mismatch at the interface. According to the strain theory [Tabata et al., 1994], the defects which appeared at

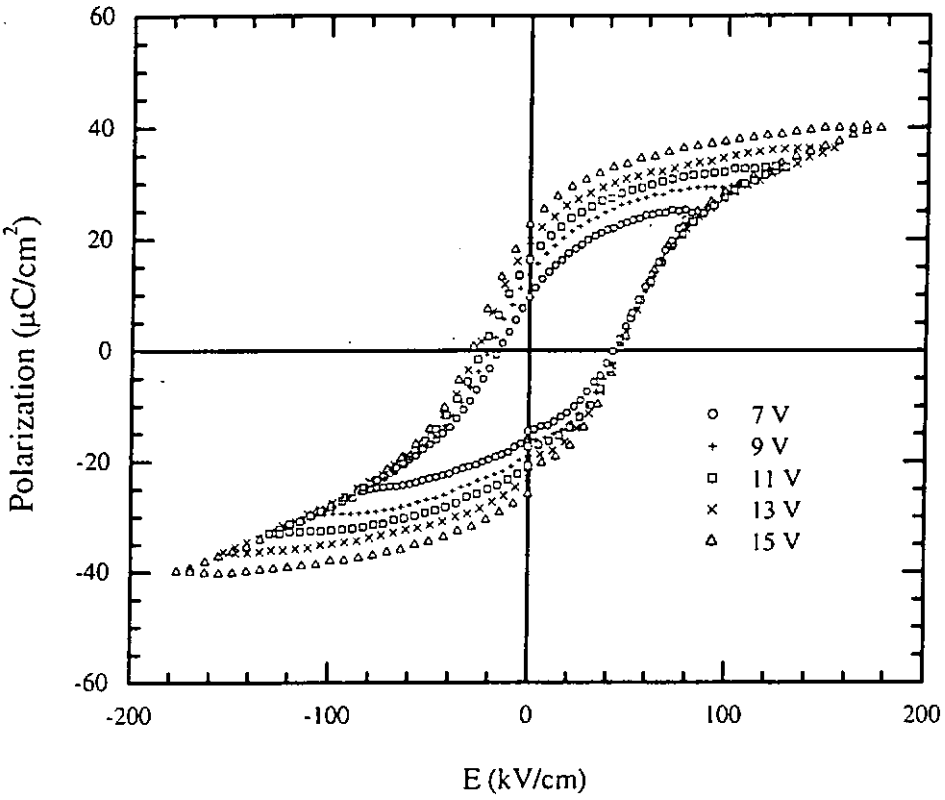

Fig.7.11 P-E hysteresis loops of the Au/PZT/YBCO/MgO/TiN/Si capacitor.

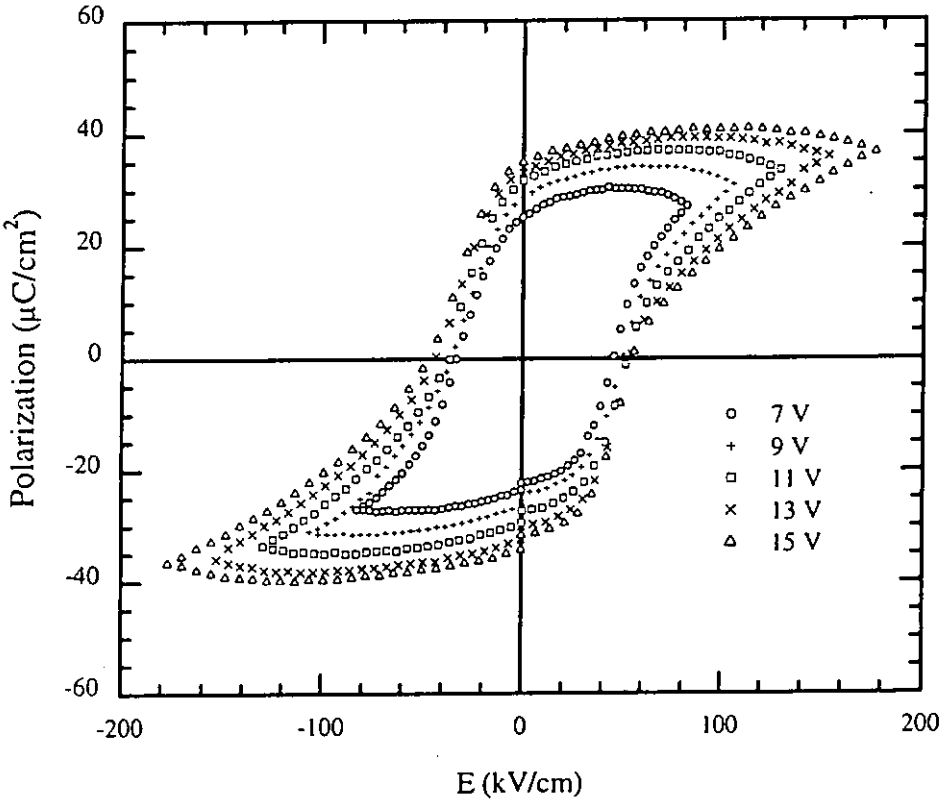

Fig.7.12 P-E hysteresis loops of the Au/PZT/YBCO/LAO capacitor.

the interface between the PTO layer and other material can generate strain and induce stress at the interface. The stress would then induce piezoelectric effect on the PTO layer and result in the generation of charges at the top and the bottom interfaces. Therefore, an appending electric field is produced in the PTO layer. And from the whole capacitor, this property is similar to a constant bias on the top electrode. The absolute value of E_c^- was less than that of E_c^+ suggesting that the DC bias on the top electrode is negative which offsets a part of the polarized field in the PTO layer and results in the asymmetry of the hysteresis loop of the Au/PTO/YBCO capacitor. Applying the same concept, the asymmetry of electric properties of Au/PZT/YBCO/MgO/TiN/Si capacitor may be due to the interface of PZT/YBCO and the lattice mismatch. (Au, 4.08 Å; PZT, a = 4.08 Å; YBCO, a = 3.82 Å, b = 3.89 Å, c = 11.68 Å).

7.3.2 Fatigue Behavior

Fig.7.13 shows the normalized switchable polarization as a function of switched cycles of the Au/PZT/YBCO/MgO/TiN/Si capacitor. It shows that the switchable polarization does not change much up to 10^7 cycles. After that, there is a gradual loss of polarization. It drops down to 70% of its initial polarization in 10^9 cycles. Fig.7.14 shows the corresponding change of the hysteresis loop. It seems that the change in the hysteresis loop is not significant. The drop in the remnant polarization is not much. However, from the fatigue profile, it does show that Au/PZT/YBCO/MgO/TiN/Si capacitor starts to fatigue after 10^7 cycles. In fact, in order to get a fatigue free capacitor, YBCO itself as the top electrode may be used.

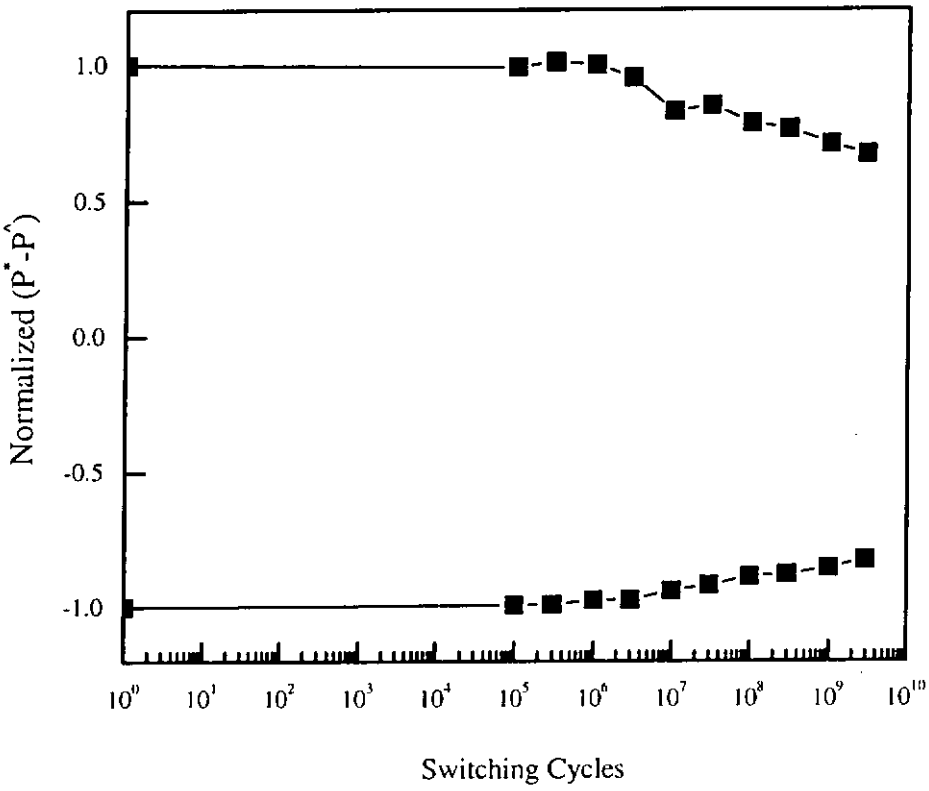

Fig.7.13 Fatigue characteristic of the Au/PZT/YBCO/MgO/TiN/Si capacitor.

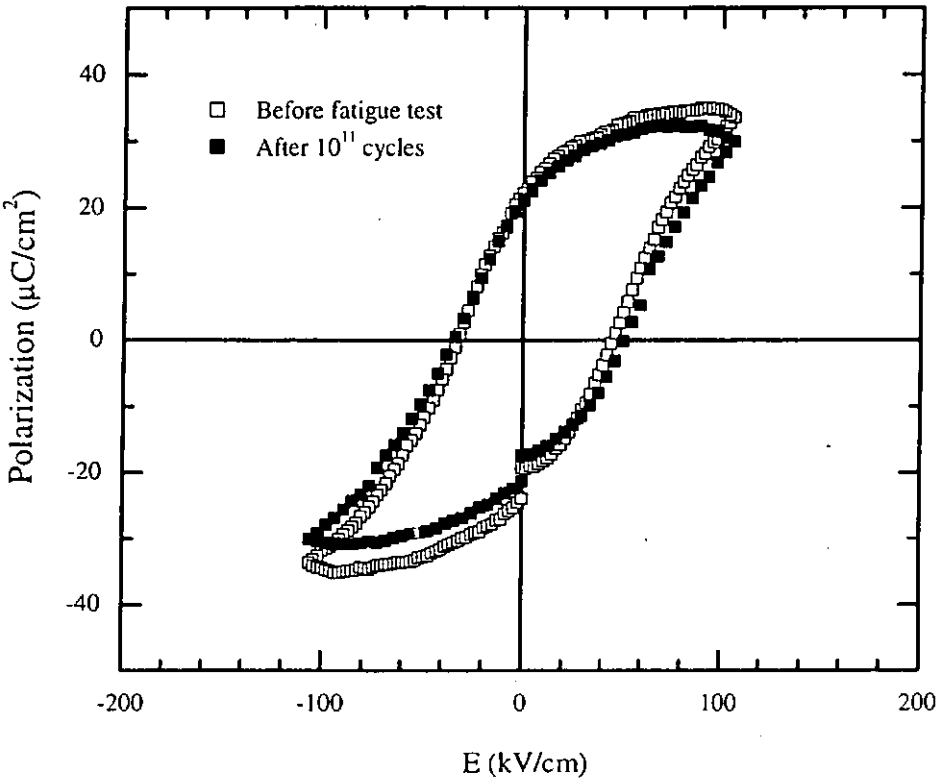

Fig.7.14 Hysteresis loops before and after fatigue test for the Au/PZT/YBCO/MgO/TiN/Si capacitor.

As mentioned in Chapter 1, using highly conductive oxide such as RuO_2, IrO_2, $La_{0.5}Sr_{0.5}CoO_3$(LSCO) and $YB_2Cu_3O_7$(YBCO) as electrodes yield greatly improved fatigue characteristics. It is believed that oxygen vacancies in the PZT thin films can easily exchange with the oxygen in the oxide electrodes, thereby reducing the oxygen vacancy pileup at interfaces and reducing the fatigue. In addition, Ramesh et al. [1992] pointed out that the superconductive cuprate was a better oxide electrode candidate for ferroelectric memory devices than the conventional Pt metal electrode. However, in order to have good fatigue-free performance as well as a low leakage current, using hybrid electrodes may be a much better choice as will be discussed in Section 7.3.4.

7.3.3 Dielectric Constant

The dielectric constant for a bulk PZT is between 1000-3200. The highest dielectric constant extracted from the maximum capacitance of the Au/PZT/YBCO/MgO/TiN/Si capacitor was 648 and the dielectric loss is 0.06 as measured at a frequency of 1 kHz. Actually, it is better than Wu et al. [1993] who reported that the dielectric constant of their PZT film on YBCO was only 330. They explained the lower value of the dielectric constant might contribute to the diffuse interface, as defined by a particulate microstructure. From these results, it is apparent that in order to fabricate ferroelectric film with high dielectric constant and low loss tangent, high quality heteroepitaxial films with sharp and clean interface are required.

7.3.4 Current-voltage Characteristic

Fig.7.15 shows the current-voltage curve of the Au/PZT/YBCO/MgO/TiN/Si capacitor. From the figure, it is seen that as the voltage is increasing, the current density is increasing. The minimum current density is 10^{-7} A/cm^2 with an applying voltage of 1 V. Actually, in order to improve the leakage current, hybrid or layered electrodes that include Pt and oxides can be used [Al-Shareef et al., 1995]. Al-Shareef et al has pointed out that using the new hybrid electrodes the PZT capacitor can have low leakage as well as good fatigue performance. Usually, the PZT films with oxide electrodes exhibit high leakage. According to Lee et al.[Lee et al., 1995], the high leakage is due to the fact that the Schottky barrier for the charge carrier injection through the Pt/PZT interface is much higher than that for oxide/PZT interface. Therefore, the injection current through the former is expected to be much higher than through the latter. Apart from this, the high conduction of PZT films with oxide electrodes is controlled by conductive secondary phase formed at the grain boundaries due to diffusion of the electrode material [Al-Shareef et al., 1994].

In conclusion, a better crystal growth of PZT films is obtained on the YBCO/MgO/TiN/Si heterostructure. Excellent ferroelectric properties of the Au/PZT/YBCO/MgO/TiN/Si capacitor are demonstrated. The P_r, P_s and E_c obtained are comparable to those of PZT films grown directly on single crystal substrates. In addition, a high dielectric constant of 648 and a low leakage current density of 10^{-7} A/cm^2 at an applying voltage of 1V are obtained. Furthermore, the integrated ferroelectric capacitor shows no sign of polarization fatigue up to 10^7 switching

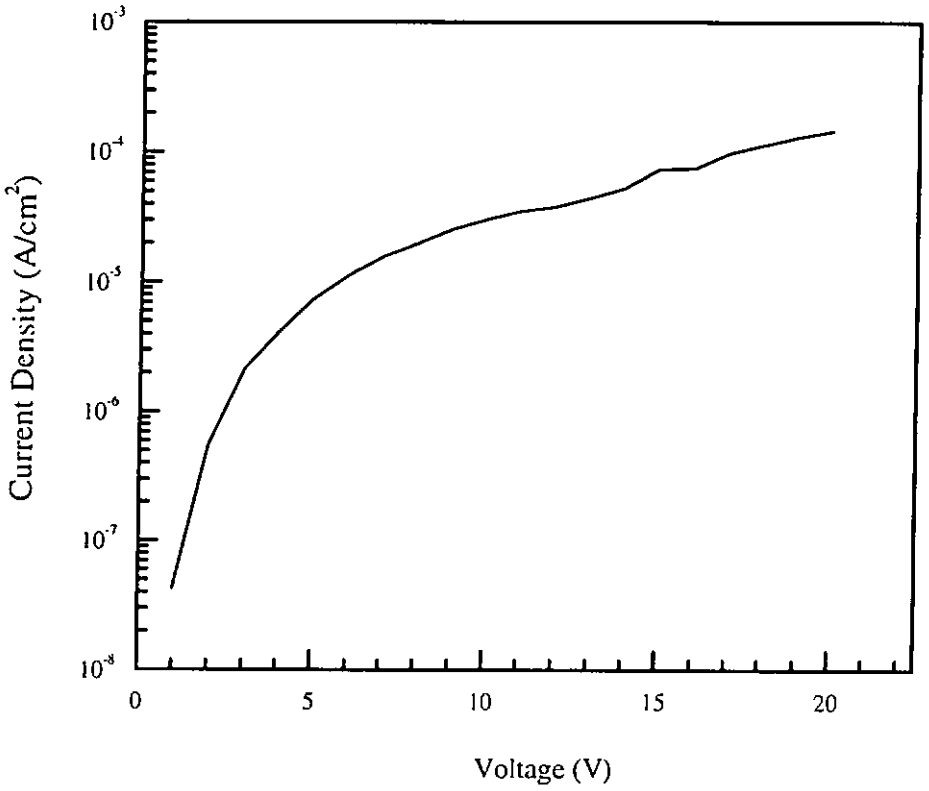

Fig.7.15 Current-Voltage characteristic of the Au/PZT/YBCO/MgO/TiN/Si capacitor.

cycles. We have therefore demonstrated that the heteroepitaxial structure Au/PZT/YBCO/MgO/TiN/Si is a viable system for developing into practical NVFERAM.

Chapter 8

Conclusion

In order to fabricate novel epitaxial ferroelectric thin film capacitors on buffered Si substrates for potential non-volatile memory devices, heteroepitaxial multilayer which include SVO/TiN/Si, STO/TiN/Si, MgO/TiN/Si, YBCO/STO/TiN/Si, YBCO/MgO/TiN/Si, Au/PZT/YBCO/STO/TiN/Si and Au/PZT/YBCO/MgO/TiN/Si were fabricated. Apart from these heterostructures, high quality conducting oxide thin films such as SVO and YBCO, and the Au/PZT/YBCO heterostructure were also fabricated on (100)$LaAlO_3$ single crystal substrates. The structural properties of these deposited films were characterized by a four-circle (X-ray θ-2θ scan, ω-scan and ϕ-scan) X-ray diffractometer using Cu $K\alpha$ radiation. Electrical property such as the resistivity against temperature of the SVO and YBCO films was measured by the standard four-point-probe technique over a temperature range from 77 K to room temperature. Measurements of ferroelectric properties of the PLD PZT films such as P-E loops, polarization switching fatigue, dielectric constant and I-V curves were also carried out.

From the X-ray ω-scan rocking curves, it is shown that high quality SVO films can be obtained on TiN buffered Si substrate. The X-ray 360° ϕ-scans diffraction patterns, suggest that SVO can be epitaxially grown on Si at a processing temperature as low as 550°C and heteroepitaxial relationship of $(100)_{SVO}||(100)_{TiN}||(100)_{Si}$ has been obtained. The SVO films are of good metallic

properties and resistivities down to 3 $\mu\Omega$-cm at 78 K was achieved. This represents the lowest resistivity achieved for non-superconducting oxides. The high conductivity of SVO is attributed to the presence of high concentration of oxygen vacancies in the oxygen defficient SVO films. For these reasons, SVO needs to be prepared under high vacuum and should avoid excessive oxidation at high temperature in oxygen ambient. In fact, it is envisaged that SVO can be used as conductive oxide electrodes in applications where neither high temperature nor ambient oxygen is involved.

Since ferroelectric PZT films needed to be processed under 250 mTorr ambient oxygen pressure at 550°C or above, the use of SVO as conducting oxide electrodes would inevitably result a down graded conduction and poor film crystallinity. Instead we choose YBCO as the bottom electrode for the ferroelectric PZT capacitor. It has superconductivity property at the transition temperature (T_c) of about 88 K. It is metallic like and has good electrical conduction at room temperature. Epitaxial YBCO/STO/TiN/Si heterostructure has been fabricated. However, scanning electron microscopic studies of the film surfaces revealed that the films had several types of defects such as grain boundaries, thermally induced cracks and irregular shaped outgrowths. In fact, the thermally induced cracks were likely due to the large difference in thermal expansion coefficient between YBCO and STO and the oxidation of TiN layer. In view of this, instead of STO/TiN buffer layers, MgO/TiN buffer layers were used. In comparison, YBCO/MgO/TiN/Si heterostructure not only has a much better crystallinity but also a much better surface morphology. Apart from some spherical particulates, which is a common

PLD feature without shadow masks, there is no apparent cracking and holes on the surface of the YBCO films. Besides, the PZT films deposited on YBCO/MgO/TiN/Si heterostructure also show superior crystallinity, smooth surface morphologies and better ferroelectric properties. Actually, the remnant polarization, saturation polarization and coercive field of the PZT film in this heterostructure are comparable to that of PZT film grown on single crystal LAO substrate. For the Au/PZT/YBCO/MgO/TiN/Si integrated ferroelectric capacitor, they are 24 $\mu C/cm^2$, 40 $\mu C/cm^2$ and 47 kV/cm respectively, whereas that of the Au/PZT/YBCO/LAO capacitor, they are 36 $\mu C/cm^2$, 42 $\mu C/cm^2$ and 47 kV/cm respectively. No apparent fatigue was observed up to 10^7 polarization switching cycles. In addition, the Au/PZT/YBCO/MgO/TiN/Si capacitor had a high dielectric constant of 648 and the corresponding dielectric loss was about 0.06. The leakage current of such capacitor was in the order of 10^{-7} A/cm^2.

In conclusion, Au/PZT/YBCO/MgO/TiN/Si integrated ferroelectric capacitors of good electrical performance have been fabricated. Their potential for use in future NVFERAM has been demonstrated. In order to enhance its long-term operation reliability, its resistance to fatigue may improve further using YBCO as both the top and bottom electrodes, i.e. YBCO/PZT/YBCO/MgO/TiN/Si heterostructure. It is believed that oxide electrodes can alleviate fatigue. However, PZT thin film capacitors with oxide electrodes typically exhibit high leakage current which actually impede their practical use for memory applications. In order to have a low leakage as well as good fatigue performance, hybrid electrodes are perhaps a

much better choice. For example, for the YBCO/PZT/YBCO/MgO/TiN/Si heterostructure, instead of using YBCO as the bottom electrode, the YBCO/Pt or Pt/YBCO hybrid electrodes may be used, i.e. YBCO/PZT/YBCO/Pt/MgO/TiN/Si or YBCO/PZT/Pt/YBCO/MgO/ TiN/Si. The merits of such or similar hybrid electrodes, however, need further in-depth investigations.

References

Al-Shareef, H. N., O. Auciello, and A. I. Kingon, "Electrical properties of ferroelectric thin-film capacitors with hybrid (Pt, RuO_2) electrodes for nonvolatile memory applications", J. Appl. Phys., Vol.77 (5), pp.2146-2154 (1995).

Auciello, O., J. F. Scott, and R. Ramesh, "The physics of ferroelectric memories", Phys. Today, pp.22-27 (July, 1998).

Chan, Siu-Wai, D.M. Hwang, and L. Nazar, "Microstructure of $YBa_2Cu_3O_{7-x}$ thin films grown on single-crystal $SrTiO_3$", J. Appl. Phys., Vol.65 (12), pp.4719-4722 (1989).

Cheung, Jeffrey T., James M. Isoris Gergis, and Roger E. DeWames, "Reproducible growth of high quality $YBa_2Cu_3O_{7-x}$ film on (100) MgO with a $SrTiO_3$ buffer layer by pulsed laser deposition", Appl. Phys. Lett., Vol.60 (25), pp.3180-3182 (1992).

Cheung, Jeffery T., "History and Fundamentals of Pulsed Laser Deposition", Chrisey B. Douglas, and Hubler K. Graham, Pulsed Laser Deposition of Thin Films, John Wiley & Sons, Inc, New York, pp.5-10 (1994).

Du, Xiaofeng, and I.-Wei Chen, "Fatigue of $Pb(Zr_{0.53}Ti_{0.47})O_3$ ferroelectric thin films", J. Appl. Phys., Vol.83 (12), pp.7789-7799 (1998).

Fork, D. K., F. A. Ponce, J. C. Tramontana, and T. H. Geballe, "Epitaxial MgO on Si(001) for Y-Ba-Cu-O thin-film growth by pulsed laser deposition", Appl. Phys Lett., Vol.58 (20), pp.2294-2296 (1991).

Funakubo, H., Y. Takeshima, D. Nagano, A. Saiki, K. Shinozaki, and N. Mizutani, "Deposition conditions of $SrTiO_3$ films on various substrates by CVD and their dielectric properties", Thin Solid Films, Vol.334 (1-2), pp.71-76 (1998).

Gao, J., L. Zheng, X. Zhu, L. Wang, C. Lin, and D. Zhu, "Asymmetry of the hysteresis loops for the $Au/PbTiO_3/YBa_2Cu_3O_{7-\delta}$ capacitor", Nucl. Instr. Meth. in Phys. Res. B, Vol.169, pp.12-15 (2000).

Gupta, Ram P., W. S. Khokle, R. C. Dubey, Seema Singhal, and K. C. Nagpal, "Y-Ba-Cu-O superconducting film on oxidized silicon" Appl. Phys Lett., Vol.52 (23), pp.1987-1988 (1988).

Hwang, Doo-Sup, Soon-Gul Lee, Yong-Ki Park, John-S Chun, and Jong-Chul Park, "Observation of defects and growth orientations of $YBa_2Cu_3O_x$ thin films with YSZ buffer layers on Si", Physica C, Vol.250, pp.375-381 (1995).

Ishiwara, H., and K. Jyokyu, "Formation of Conductive $SrVO_3$ Films on Si Substrates", Jpn. J. Appl. Phys., Vol.30 (12A), pp.L2059-L2061 (1991).

Juang, J.Y., R.T. Kao, M.C. Hsieh, M.H. Li, M.L. Chu, K.H. Wu, T.M. Uen, and Y.S. Gou, "Growth of pulsed laser deposited YBCO thin films on YSZ and YSZ/Si substrates", Physica B: Condensed Matter, Vol.194-96, Part 1, pp.385-386 (1994).

Lee, S. H., S. C. Bae, J. G. Kang, H. J. Kang, H. J. Shin, and J. K. Ku, "Substrate temperature effects on the preparation of $YBa_2Cu_3O_{7-x}$ superconducting films on (100) $SrTiO_3$ by laser ablation", J. Appl. Phys., Vol.70 (10), pp.5661-5666 (1991).

Lee, H. N., Y. T. Kim, and Y. K. Park, "Memory window of highly c-axis oriented ferroelectric $YMnO_3$ thin films", Appl. Phys Lett., Vol.74 (25), pp.3887-3889 (1999).

Lee, J., R. Ramesh, V. G. Keramidas, W. L. Warren, G. E. Warren, and Jr., J. T., Evans, "Imprint and oxygen deficiency in (Pb, La)(Zr, Ti)O_3 thin-film capacitors with La-Sr-Co-O electrodes", Appl. Phys Lett., Vol.66 (11), pp.1337-1339 (1995).

Lee, J., and R. Ramesh, "Imprint of (Pb,La)(Zr,Ti)O_3 thin films with various crystalline qualities", Appl. Phys Lett., Vol.68 (4), pp.484-486 (1996).

Lee, M. B., and H. Koinuma, "Structural and dielectric properties of epitaxial $SrTiO_3$ films grown on Si(100) substrate with TiN buffer layer", J. Appl. Phys., Vol.81 (5), pp.2358-2362 (1997).

Leung, Yau Shing, "Fabrication and characterization of pulsed laser deposition of $La_{1-x}Ca_xMnO_3$ based heterostructures", The Hong Kong Polytechnic University, Hong Kong (1998).

Liu, J. M., S. Y. Xu, W. Z. Zhou, X. H. Jiang, C. K. Ong, and L. C. Lim, "Preparation of (001)-oriented PZT thick films on silicon wafer by pulsed laser deposition", Materials Science and Engineering A, Vol.269, pp.67-72 (1999).

Luo, Li, X. D. Wu, R.C. Dye, R.E. Muenchausen, S.R. Foltyn, Y. Coulter, and C. J. Maggiore, "a-axis oriented $YBa_2Cu_3O_{7-x}$ thin films on Si with CeO_2 buffer layers", Appl. Phys Lett., Vol.59 (16), pp.2043-2045 (1991).

Moon, B. K., and H. Ishiwara, "Roles of Buffer Layers in Epitaxial Growth of $SrTiO_3$ Films on Silicon Substrates", Jpn. J. Appl. Phys., Vol.33, Part I (3A), pp.1472-1477 (1994).

Moon, B.K., E. Tokumitsu, and H. Ishiwara, "Formation of high-dielectric oxide films on $SrVO_{3-x}Si$ substrates", Materials Science and Engineering, Vol. B41, pp.157-160 (1996).

Nagata, H., T. Tsukahara, M. Yoshimoto, and H. Yoshimoto, "Laser molecular beam epitaxy of single-crystal $SrVO_{3-x}$ films", Thin Solid Films, Vol.208, pp.264-268 (1992).

Narayan, J., P. Tiwari, X. Chen, J. Singh, R. Chowdhury, and T. Zheleva, "Epitaxial growth of TiN films on (100) silicon substrates by laser physical vapor deposition", Appl. Phys. Lett., Vol.61 (11), pp.1290-1292 (1992).

Qiao, Jianmin, and Cary Y. Yang, "High-T_c superconductors on buffered silicon: materials properties and device applications", Materials Science and Engineering, Vol. R14, pp.157-201 (1995).

Ramesh, R., W. K. Chan, B. Wilkens, H. Gilchrist, T. Sands, J.M. Tarascon, V.G. Keramidas, D. K. Fork, J. Lee , and A. Safari, "Fatigue and retention in ferroelectric Y-Ba-Cu-O/Pb-Zr-Ti-O/Y-Ba-Cu-O heterostructures", Appl. Phys Lett., Vol.61 (13), pp.1537-1539 (1992).

Ramesh, R., H. Gilchrist, T. Sands, and V.G. Keramidas, "Ferroelectric La-Sr-Co-O/Pb-Zr-Ti-O/ La-Sr-Co-O heterostructures on silicon via template growth", Appl. Phys. Lett., Vol.63 (26), pp.3592-3594 (1993).

Ritums, D. L., N. J. Wu, X. Chen, D. Liu, and A. Ignatiev, "Conducting and interfacial properties of epitaxial SVO films" Space Technology and Applications International Forum, pp.672-677 (1998).

Singh, Rajiv K., and D. Kumar, "Pulsed laser deposition and characterization of high-T. $YBa_2Cu_3O_{7-x}$ superconducting thin films", Materials Science and Engineering, R22, pp.113-185 (1998).

Scott, J. F., and Carlos A. PAZ DE ARAUJO, "Ferroelectric Memories", Science, Vol.246, pp.1400-1405 (1989).

Sinharoy, S., H. Buhay, D. R. Lampe, and M. H. Francombe, "Integration of ferroelectric thin films into nonvolatile memories", J. Vac. Sci. Technol. A, Vol.10 (4), pp.1554-1561 (1992).

Stolichnov, I., A. Tagantsev, N. Setter, J. S. Cross, and M. Cross, "Control of leakage conduction of high-fatigue-endurance (Pb,La)(Zr,Ti)O_3 film ferroelectric capacitors with Pt/$SrRuO_3$ electrodes", Appl. Phys Lett., Vol.75 (12), pp.1790-1792 (1999).

Tabata, H., H. Tanaka, and B. A. Tuttle, Ferroelectric Thin Films IV, Research Society Symposium Proceedings, Vol.361, pp.453 (1994).

Tsai, J.C.C., "Diffusion". S. M. Sze, VLSI Technology, McGraw-Hill Book Company, New York, pp.272-326 (1988).

Tsvetanka Zheleva, K. Jagannadham, and J. Narayan, "Epitaxial growth in large-lattice-mismatch systems", J. Appl. Phys., Vol.75 (2), pp.860-871 (1994).

Vijay, D. P., and S. B. Desu, "Electrodes for $PbZr_xTi_{1-x}O_3$ Ferroelectric Thin Films", J. Electrochem. Soc., Vol.140 (9), pp.2640-2645 (1993).

Wu, N. J., A. Ignatiev, A. W. Mesarwi, H. Lin, K. Lin, and H. D. Shih, "Heterostructures of $Pb(Zr_xTi_{1-x})O_3$ and $YBa_2Cu_3O_{7-\delta}$ on MgO Substrate Prepared by Pulsed Laser Ablation", Jpn. J. Appl. Phys., Vol.32, Part I (11A), pp.5019-5023 (1993).

Wu Wenbin, K. H. Wong, and C. L. Choy, "Low-temperature growth of epitxial $LaNiO_3/Pb(Zr_{0.52}Ti_{0.48})O_3/ LaNiO_3$ on Si(001) by pulsed-laser deposition", J. Vac. Sci. Technol. A, Vol.18 (1), pp.79-82 (2000).

Wu Wenbin, K. H. Wong, C. L. Mak, and C. L. Choy, "Effect of oxygen stoichiometry on the ferroelectric property of epitaxial all-oxide $La_{0.7}Sr_{0.3}MnO_3/Pb(Zr_{0.52}Ti_{0.48})O_3/ La_{0.7}Sr_{0.3}MnO_3$ thin film capacitors", J. Vac. Sci. Technol. A, Vol.18 (5), pp.1-5 (2000).

Wu Wenbin, K. H. Wong, C. L. Mak, C. L. Choy, and Y. H. Zhang, "Epitaxial $Pb(Zr_{0.52}Ti_{0.48})O_3/La_{0.35}Nd_{0.35}Sr_{0.3}MnO_3$ heterostructures for fabrication of ferroelectric field-effect transistor", J. Appl. Phys., Vol.88 (4), pp.2068-2071 (2000).

Young, Sik Jeong, Joo Hyung Park, and Sang Yeol Lee, "Epitaxial growth of YBCO on Hastelloy with YSZ buffer layer by laser ablation", Thin Solid Films, Vol.318, pp.262-264 (1998).

Sharma, A. K., J. Narayan, C. Jin, A. Kvit, S. Chattopadhyay, and C. Lee, "Integration of $Pb(Zr_{0.52}Ti_{0.48})O_3$ epilayers with Si by domain epitaxy", Appl. Phys. Lett., Vol.76 (11), pp.1458-1460 (2000).

Greedan, J. E., A. O'Reilly, and C.V. Stager, "Oxygen ordering in the crystal structure of the 93-K superconductor YBa2Cu3O7 using powder neutron diffraction at 298 and 79.5 K", Phys.Rev. B, Vol.35, pp.8770-8773 (1987).

M. Hao, K. Lai, W. M. Chen, and J. C. Lee, "Surface cleaning effect on dielectric integrity for ultrathin oxynitrides grown in N2O" Appl. Phys. Lett., Vol.65, pp.1133 (1994).

Kim, Sung-Min, and Sang Yeol Lee, "Characterization of YBCO superconducting films fabricated by pulsed laser deposition", Thin Solid Films, Vol.355-356, pp.461-464 (1999).